UNIVERSITÉ SORBONNE PARIS CITÉ

Thèse préparée
à l'INSTITUT DE PHYSIQUE DU GLOBE DE PARIS
École doctorale STEP'UP – ED N°560
IPGP - Équipe de Tectonique et Mécanique de la Lithosphère

Fast algorithms to model quasi-dynamic earthquake cycles in complex fault networks

par
Pierre Romanet

présentée et soutenue publiquement le
10 Octobre 2017

Thèse de doctorat de Sciences de la Terre et de l'environnement

dirigée par Raúl Madariaga

devant un jury composé de :

Michel Bouchon Directeur de recherche (ISTerre, Grenoble)	Rapporteur
David Marsan Professeur (ISTerre Université Savoie Mont-Blanc)	Rapporteur
Hideo Aochi Senior research engineer/Chercheur Associé (BRGM et ENS)	Examinateur
Nadaya Cubas Maitre de Conférence (UPMC)	Examinateur
Harsha S. Bhat Chargé de Recherche (ENS Paris)	Co-encadrant
Raúl Madariaga Professeur (ENS Paris)	Directeur de thèse

Invité : **Satoshi Ide**, Professeur (University of Tokyo)

Table des matières

Table des matières 2

1 Introduction **6**

1.1 The faulting origin of earthquakes 7

1.2 Observations 11

1.2.1 Crust is composed of a myriad of interconnected fault that interact with each other 11

1.2.2 The seismic cycle budget has now to take into account slow-phenomena 15

1.3 Models of earthquake cycles 18

1.3.1 Spring slider models 21

1.3.2 Continuum models 23

1.4 Spatio-temporal complexities in earthquake cycle modeling . 26

2 Fast methods for quasi-dynamic earthquake cycles in 2D non planar geometries **29**

2.1 Introduction 30

2.2 Boundary Integral Equation for planar elasticity 32

2.2.1 Numerical calculation 36

2.3 Fast Fourier Transform 37

2.4 Fast Multipole Method 38

2.4.1 Adaptive quad-tree structure 39

2.4.2 Analytic approximation of the kernel 41

2.5 Hierarchical Matrices 48

2.5.1 Introduction 48

2.5.2 Construction of a binary tree 51

2.5.3 Construction of the structure of the matrix 51

2.5.4 Admissibility condition 51
2.5.5 Low rank approximation 54
2.5.6 Conclusion of H-matrix 56
2.6 Model of earthquake cycle 57
2.6.1 Rate and State Friction 57
2.6.2 Loading 57
2.6.3 Radiation damping term 57
2.6.4 Governing equations for Quasi-Dynamic earthquake cycle models 58
2.7 Comparison of H-matrices and Fast Multipole Method 59
2.7.1 Speed of methods 59
2.7.2 Accuracy 60
2.8 Conclusion 64

3 Overlapping faults in mode III **65**
3.1 Introduction 66
3.2 Single planar fault 70
3.3 Two overlapping faults 73
3.3.1 Overlapping faults with constant overlap at close distance to each other 74
3.3.2 Overlapping faults with constant overlap at far distance to each other 82
3.3.3 Variation around the geometry 84
3.4 Statistics of slow and fast events 93
3.5 Conclusion 98

4 Perspectives **100**
4.1 Fault roughness 101
4.1.1 Introduction 101
4.1.2 Rough fault in out-of-plane configuration 101
4.1.3 Rough fault in in-plane configuration 102
4.1.4 Discussion and conclusion 106
4.2 Induced seismicity 110
4.2.1 Introduction 110
4.2.2 Model 110
4.2.3 Fluid injection during earthquake cycle 113

- 4.2.4 Conclusion 113
- 4.3 Real geometry of fault network 120
  - 4.3.1 Scenario 1 : initial nucleation on Camp Rock fault . . 121
  - 4.3.2 Scenario 2 : initial nucleation on Homestead Valley Fault 126
  - 4.3.3 Scenario 3 : initial nucleation on Johnson Valley Fault 129
  - 4.3.4 Discussion and conclusion 132

5 Conclusion 133

- 5.1 Conclusion 133
- 5.2 Perspectives futures 135
  - 5.2.1 Rugosité et réseau de failles 135
  - 5.2.2 Simulation complètement dynamique en 3D 136
  - 5.2.3 Atténuation des risques liés aux tremblements de terre 136
- 5.3 Conclusions générales 137

Résumé

Les failles sont rarement uniques et planes, le plus souvent elles agissent en réseau et présentent des complexités géométriques (rugosité, branches etc) à toutes les échelles. Cependant, la majorité des modèles de cycles sismique jusqu'à ce jour, ne prennent pas en compte ces complexités géométriques. Cela est principalement dû aux limites des ressources informatiques, et au temps de calcul qui ne peut être accéléré simplement qu'en géométrie plane. Dans cette thèse, nous avons développé un nouveau modèle quasi - dynamic du cycle sismique, avec une loi de friction de type ”rate and state” et une loi d'évolution de la variable d'état ”aging”. Pour surmonter le problème du temps de calcul, sans pour autant se restreindre à une géométrie plane, nous avons fait appel à deux méthodes : la méthode multipolaire rapide et les matrices hiérarchiques. Ces deux méthodes permettent des gains de temps significatifs en réduisant la complexité du temps de calcul de l'ordre de $\mathcal{O}(N^2)$ à $\mathcal{O}(N \log N)$, N étant le nombre d'éléments utilisés pour discrétiser la faille. En utilisant ce modèle, nous avons pu explorer le comportement de deux failles dont une partie se superpose en mode III. Alors qu'une faille unique donne lieu à un comportement périodique, avec toujours le même tremblement de terre se répétant, l'introduction d'une seconde faille interagissant avec la première fait apparaître une grande complexité dans le cycle sismique : comportement apériodique, ruptures partielles, ”afterslip”, coexistance des évènements lents et rapides. Dans le domaine particulier ou évènements de glissement lent et rapide coexistent, nous avons montré que le moment des ces deux types d'événement suivaient des lois d'échelle qui s'apparentent aux lois observées dans la nature par *Ide et al.* (2007). Nous avons aussi montré que la rugosité et les réseaux de failles en mode II (”in-plane”), provoquaient le même genre de complexités dans le cycle sismique.

Chapitre 1

Introduction

Avant-propos

Cette section présente une introduction générale à la problématique de cette thèse. La première partie est une introduction historique à la découverte des failles en temps qu'origine des tremblements de terre. Nous nous attachons à retracer les principales découvertes et intuitions qui ont amené à identifier les failles comme moyen de relâcher les déformations accumulées dans la croûte terrestre. Dans une deuxième partie, nous présentons les failles vues dans leur ensemble et non plus seulement en temps qu'entité unique. Au travers d'exemples, nous montrons que, dans de nombreux cas, la rupture sismique met en jeu de nombreuses failles établies en réseau. Nous nous attachons à démontrer que la géométrie et les réseaux de failles ont un rôle important dans le cycle sismique. Les découvertes récentes sur la présence d'évènements de glissement lent, a remis en cause notre compréhension du cycle sismique. Les évènements lents peuvent en effet relâcher une partie non négligeable des contraintes sur les failles. L'invention de la loi empirique de friction ”rate and state” a permis, en introduisant une récupération de la résistance des failles après rupture, de simuler pour la première fois le cycle sismique complet (inter-sismique, sismique, post-sismique) en incluant plusieurs évènements (*Rice*, 1993 ; *Liu and Rice*, 2005 ; *Barbot et al.*, 2012). Les modèles patins resort ont montré des comportements similaires (lois d'Omori et de Gutenberg, comportement apériodique) aux cycles sismiques lorsqu'on les a mis en réseau, reliés entre eux par des resorts (*Burridge and Knopoff*, 1967 ; *Nussbaum and Ruina*, 1987 ;

Carlson and Langer, 1989). Cependant, le passage aux modèles continus correctement discretisés, conduit à un cycle sismique sans complexités particulières (périodique et toujours le même évènement) (Rice, 1993). ce qui a amené à devoir complexifier ces modèles continus pour pouvoir reproduire les comportements observés (séismes lents et rapides, ruptures partielles, glissements post-sismiques). En particulier les modèles actuels sont très dépendant de la longueur de nucléation, qui semble régir le domaine de comportement du cycle : apparition de séisme lent ou pas (Liu and Rice, 2005, 2007 ; Rubin, 2008 ; Veedu and Barbot, 2016), ruptures partielles (Chen and Lapusta, 2009 ; Michel et al., 2017). Ce paramètre est souvent controlé par le truchement de la variation des paramètres rhéologiques (des paramètres de la loi de friction) sur la faille. Peu de travaux se sont vraiment intéressés à l'effet des interactions de faille, et de la géométrie sur le cycle sismique, et comment la géométrie peu changer ou contrôler cette longueur de nucleation. Le but de cette thèse est donc d'étudier plus en détail l'influence de la géométrie des failles sur le cycle sismique.

1.1 The faulting origin of earthquakes

Earthquakes are one of the most striking manifestation of earth dynamics. Since the birth of humanity, people are experiencing these destructive events. However the comprehension of these phenomenons was difficult, because most of the time they do not provoke any surface fault trace, they are underground phenomena, and they can be felt far away from their hypocenter.

The first physical mechanism for earthquake was proposed by Aristotle (384-322 B.C.). Aristotle was one of the person trying to move forward the classical explanation of a divine retribution. He tried to explain earthquake based on the experience they have on atmospheric events, like thunder and lightening. His theory was that in the Earth, there are caverns producing fires, and drawing an analogy to sudden storm and lightening, these fires would sometimes expand rapidly and result in violent burst. These violent bursts would shake the ground, and create an earthquake (Agnew, 2002). Although the mechanisms they suggested were incorrect, it was the first time that they were trying to explain what was happening, relying on their experience on other phenomena. Besides some modifications of that theory, like replacing the fire with smoky vapor, the underlying idea of explosion in the ground will remain the predominant idea until the 18th century.

One of the first key point of the understanding of earthquakes was to differentiate the propagation of waves from the phenomenon that created these waves. At least two writers, J Michell (1761) and J Drijhout (1765) understood this idea (*Agnew*, 2002). By doing an analogy with sounds propagating in air, J. Michell inferred that waves were propagating through the elasticity of rocks. However the origin of these waves was still thought to be an explosion due to water vaporized suddenly by underground fires. This led to the knowledge that earthquake can be felt although the earthquake source is far away.

In the beginning of the 19th century, the development of solid mechanics provided the physical basis for the mathematical description of earthquakes. Robert Mallet (1810-1881), a polymathic Irish engineer, was most probably one the first person to try to explain earthquakes, gathering the newly developed solid mechanics together with geology and engineering. We owe him not only the term *Seismology*, but also a great improvement in seismology as a science. He made up one of the first catalog of more than 6800 of earthquakes with their location and effects. He also published one of the first world seismic hazard map (*Lee et al.*, 2002) based on this catalog (Fig. 1.1). He was the first to create artificial earthquakes with gunpowder and used its invention to calculate for the first time the P wave velocity in different kind of rocks. He found 280m/s for sandy soil and 600m/s for granite (values that are now known to be too small and are likely caused by insensitive instruments) (*Agnew*, 2002). Charles Lyell (1797-1875) was a contemporary of Robert Mallet, made important contributions in the recognition of earthquakes as a engine of earth Dynamism -p179- of *Scholz* (2002). Although the distinction between the origin of earthquakes and the propagating waves was made, and the fault relationship with earthquake was established, the emergence of the faulting origin hypothesis of earthquakes would only happen in late 19th century.

Grove Carl Gilbert (1843-1918) was a geologist, working on normal fault system in the Basin and Range province of west America (*Segall*, 2010). He was the first to recognized that a strain release along fault was the source

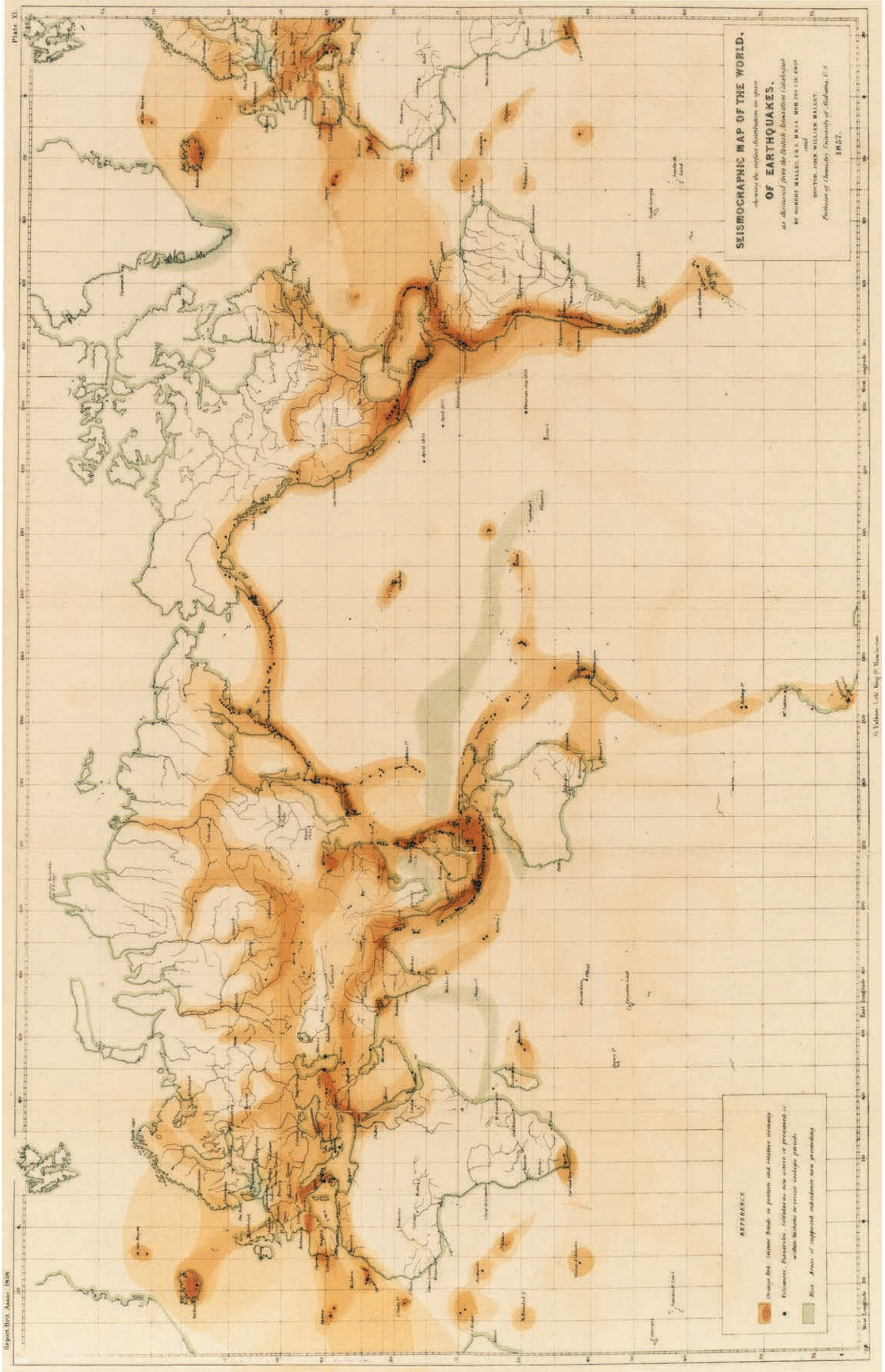

Figure 1.1 – Seismic hazard map by Robert Mallet and his son that was published in 1858. This map was only based on felt reports of earthquakes. Main subduction zones are well represented, Mallet also noted the association with large Mountain ranges. Taken from *Lee et al.* (2002)

of earthquakes. He also understood earthquake phenomenon as a stick slip phenomena 80 years before the famous paper of *Brace et al.* (1966) (*Gilbert*, 1884). He wrote in 1884 :

> The upthrust produces a local strain in the crust . . . and this strain increases until it is sufficient to overcome the starting friction on the fractured surface. Suddenly, and almost instantaneously, there is an amount of motion sufficient to relieve the strain, and this is followed by a long period of quiet, during which the strain is gradually reimposed. The motion at the instant of yielding is so swift and so abruptly terminated as to constitute a shock, and this shock vibrates through the crust with diminishing force in all directions.

At the same time as Gilbert understood the faulting origin of earthquakes, at least two authors Alexander McKay (1841-1917) and Bunjiro Koto (1856-1935) made observations of new fresh scarp concomitant with earthquakes. This observation made Bunjiro Koto think that earthquake was the result of dislocation on a fault (*Koto*, 1893). The controversy at that time was to know if faults were the origin or a consequence of earthquake. The final proof came from geodetic observations after the 1906 San Francisco earthquake by Harry Fielding Reid (1859-1944). He showed that the rupture was not only superficial but also happened in depth.This led to the generally accepted faulting origin of earthquakes. Reid gave the five statements of his elastic rebound theory in 1911 (*Segall*, 2010) :

1. The fracture of the rock, which causes a tectonic earthquake, is the result of elastic strains, greater than the strength of the rock can withstand, produced by the relative displacements of neighboring portions of the earth crust.
2. These relative displacements are not produced suddenly at the time of the fracture, but attain their maximum amounts gradually during a more or less long period of time.
3. The only mass movements that occur at the time of the earthquake are the sudden elastic rebounds of the sides of the fracture towards position of no elastic strain ; and these movements extend to distances of only a few miles from the fracture.

4. The earthquake vibrations originate in the surface of fracture ; the surface from which they start has at first a very small area, which may quickly become very large, but at a rate not greater than the velocity of compressional elastic waves in the rock.
5. The energy liberated at the time of an earthquake was, immediately before the rupture, in the form of energy of elastic strain of the rock. (Reid 1911, p. 436)

These statements lay the foundations for the understanding of faulting origin of earthquake. With small modification it is possible to identify from these statements three main ingredients that are necessary to get earthquakes :

An elastic medium The elastic medium has the role of storing energy, before the next earthquake releases it. The most simple system that one can think about in order to store elastic energy is a spring. Of course real mediums are much more complex, in reality earthquakes happen in 3 dimensional, heterogenous fractured rocks.

An inherent resistance Following Reid's theory, this inherent limit was mainly thought to be the strength of rock, although this appeared to be incorrect. We now know that this resistance is mainly frictionally controlled. However, the ways the friction acts on the two sliding parts of the faults is still an open question.

Loading The loading of the fault remained unsolved till the beginning of the 60's, where the plate tectonic was really demonstrated. It is now accepted that this is the engine that loads fault system.

1.2 Observations

1.2.1 Crust is composed of a myriad of interconnected fault that interact with each other

Along with these three ingredients, we need to account for the fact that the faults themselves are geometrically complex. In figure 1.2, it is possible

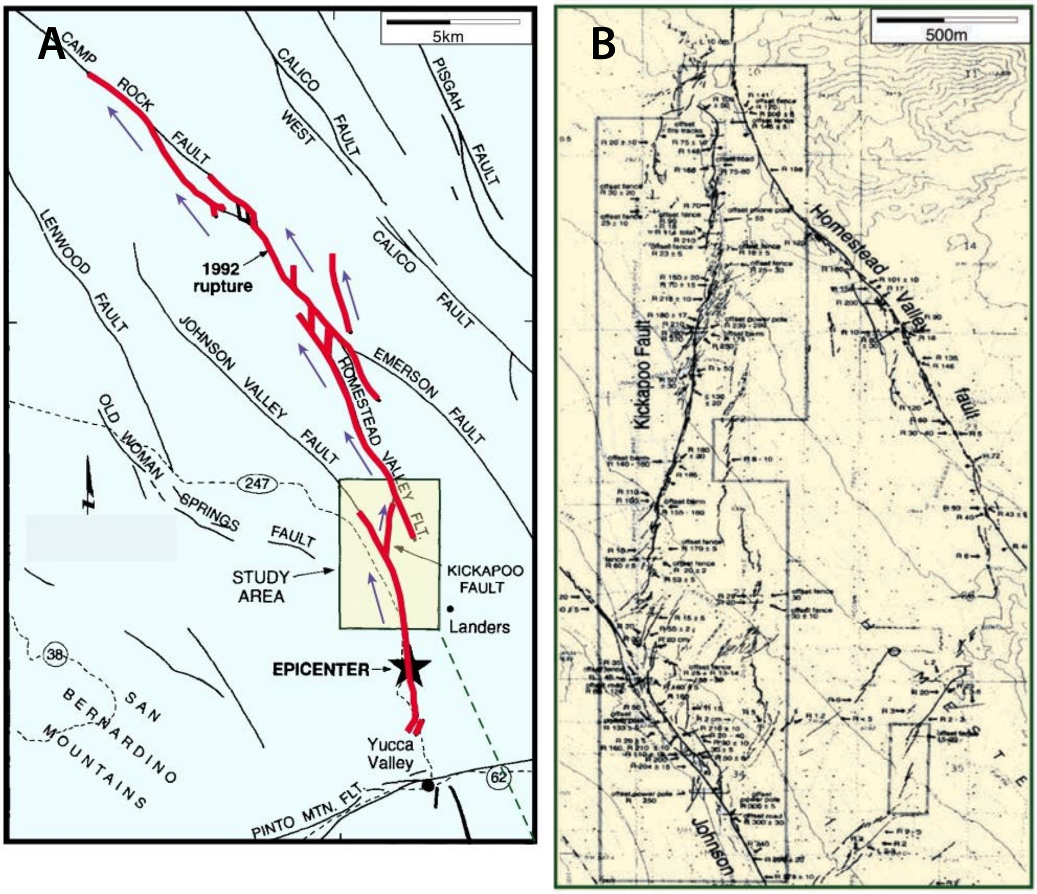

Figure 1.2 – Fault surface map of the 1992 $M_w 7.3$ Landers earthquake modified from *Sowers et al.* (1994). (A) Faults that rupture the surface are shown in red line. Earthquake really ruptures a geometrically complex fault system . (B) Zoom on a location of the Kickapoo fault. Even at smaller scale, the fault still shows geometrical complexities.

to see a fault map of the area of the 1992 $M_w 7.3$ Landers earthquake, in the eastern California shear zone. The 1992 $M_w 7.3$ Landers earthquake ruptured at least 5 major right lateral faults and many more smaller faults (*Sieh et al.*, 1993). The fault surface map of the area (Fig. 1.2 red line, from *Sowers et al.* (1994)) shows an extremely complex network of fault system with jogs, branches, and overlap of faults. If we zoom in, it is still possible to see a complex fault system with many subsidiary structures. The earthquake nucleated on the Johnson Valley Fault (*Sieh et al.*, 1993) and quickly continued to the Homestead valley fault through the Kickapoo fault (*Sowers et al.*, 1994).

An other more recent example of a complex fault network is the 2016

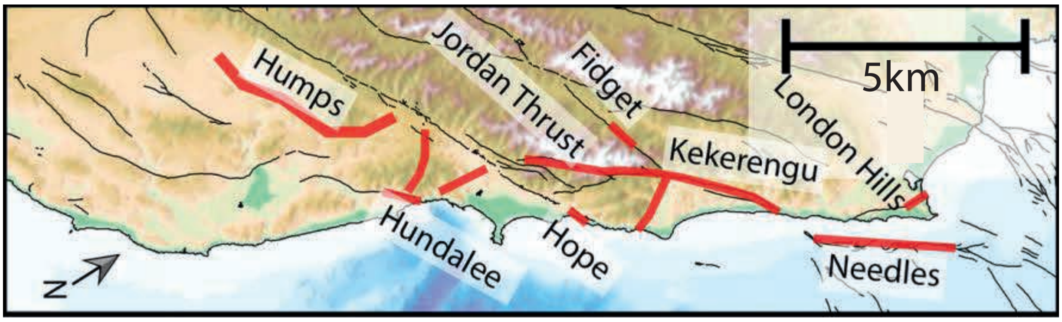

Figure 1.3 – Fault surface map of the 2016 $M_w 7.8$ Kaikoura earthquake from *Hamling et al.* (2017). Faults that ruptured to the surface are shown in red line.

$M_w 7.8$ Kaikoura earthquake that happened in north east coast of the south Island in New Zealand. This earthquake have ruptured at least 12 major faults (*Hamling et al.*, 2017). Long period analysis showed that this earthquake initiated on a small strike slip fault and propagated to the north-east (*Duputel and Rivera*, 2017). This earthquake apparently triggered slip on a splay fault, being one of the rare example where intraplate and interplate faults interact with each other (*Hollingsworth et al.*, 2017 ; *Duputel and Rivera*, 2017).

Geometry of faults themselves, including bend, jogs, kinks, was also identified to have strong implications for earthquake dynamics like initiation and arrest of ruptures (*King and Nabelek*, 1985 ; *Sibson*, 1985 ; *Wesnousky*, 1988). An other kind of geometrical complexity is the natural self-affine roughness of fault surfaces. It was initially measured at the laboratory sample scale (~ 1cm) using surface profiler (*Power et al.*, 1987 ; *Schmittbuhl et al.*, 1993). The self-affine nature of faults was shown to be a robust observation over more than 9 decades of length scales (*Lee and Bruhn*, 1996 ; *Renard et al.*, 2006 ; *Candela et al.*, 2009, 2012). The surface rupture map of faults also shows roughness *Candela et al.* (2012) (Fig. 1.4, for rupture surface map of different strike-slip fault system from *Klinger* (2010)).

It is known that these geometrical complexities are of particular importance for the dynamic of earthquakes, and some earlier work have tried to reproduce these features from a modeling perspective : how does an earthquake rupture navigate a fault branch (*Kame and Yamashita*, 2003 ; *Bhat et al.*, 2007, among others) ? What is the cause of the arrest of a rupture ? Is the cause of the enhanced high radiation pattern the roughness of the

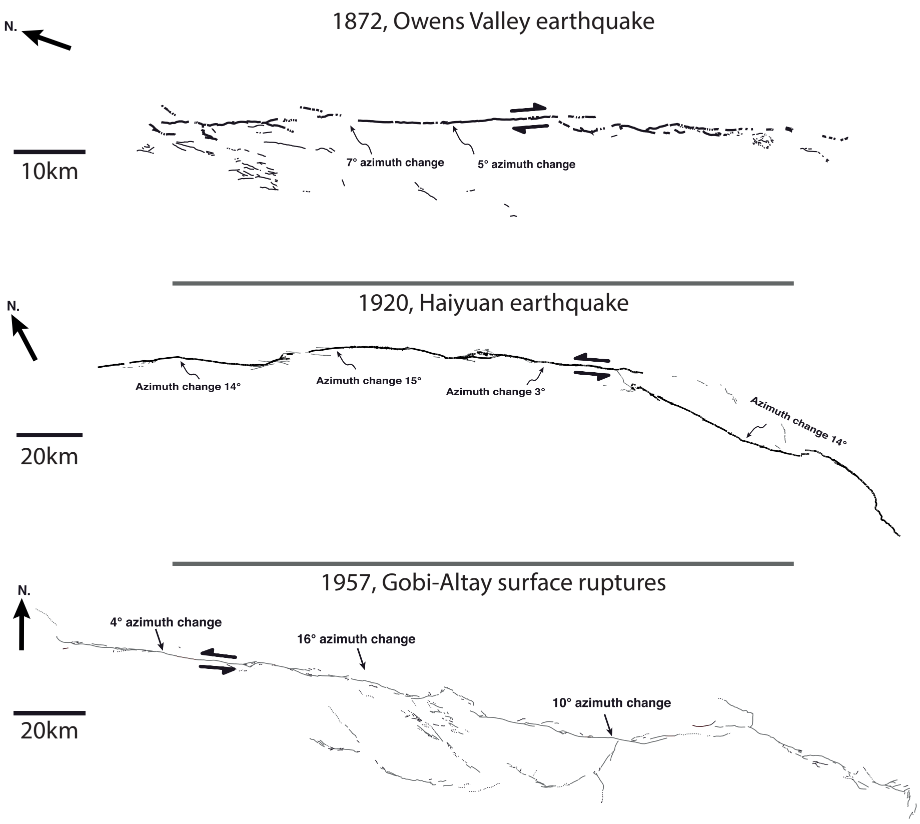
1872, Owens Valley earthquake

1920, Haiyuan earthquake

1957, Gobi-Altay surface ruptures

Figure 1.4 – Fault surface map for the 1872 $M_w 7.5 - 7.8$ Owens Valley earthquake (US), the 1920 $M_s 8$ Haiyuan earthquake (China) and the 1957 $M_w 8.3$ Gobi-Altay earthquake (Mongolia). Modified from *Klinger* (2010).

fault (*Dunham et al.*, 2011) ?. These are questions that are still not completely resolved. However, very little effort seems to have been done on the behavior of the long term seismic cycle itself. This raises a host of questions like : in a given fault network, are there areas of the fault that are subject to rupture more often that others ? How does stress transfer work in a given geometry ? Are there recurrent pattern of seismic cycles (same sequence of faults that rupture) ? Some observation seems to provide a partial answer for these questions. For example it has been observed that the roughness of the fault correlates with the slip on the fault (*Candela et al.*, 2011). However, we are still at the beginning to understand the whole complexity of fault networks. The recent years have provided a whole new host of observations, and with that the fact that faults does not only release the stress dynamically (an earthquake), but can also release stress a-seismically.

1.2.2 The seismic cycle budget has now to take into account slow-phenomena

Discovery of slow events Until the sixties, the classic image of earthquake cycle was that faults slowly accumulate stress due to plate loading during a long period called interseismic period, until this stress exceeds the strength of the fault and is suddenly released (coseismic period), resulting in an earthquake. The first evidence of another mode of slip was discovered in the sixties on San Andreas fault. *Steinbrugge et al.* (1960) observed a slow offset of a winery wall near Hollister, although no earthquakes happened at that time.

In the early 90s, the development of continuous GPS brought a new light on slow phenomena : the occurence of Slow-Slip-Events (SSEs). They are slip episodes, that happen along subduction zone. They propagate along the fault, at small rupture velocity (about 0.5 km/h in Cascadia (*Dragert et al.*, 2004) to about 1 km/day in Mexico (*Franco et al.*, 2005)) and with a small slip-velocity (from about 1mm/yr in the Bungo Channel, Japan to about 1 m/year in Cascadia) (*Schwartz and Rokosky*, 2007). Since the first detection of SSEs in Bungo Channel in Japan (*Hirose et al.*, 1999), they were discovered in nearly all subduction zones : Cascadia (*Dragert et al.*, 2001, 2004), Central Ecuador (*Vallee et al.*, 2013), Guerrero (*Lowry et al.*, 2001 ; *Kostoglodov et al.*, 2003 ; *Franco et al.*, 2005), Hikurangi (*Douglas et al.*, 2005). However, it is worth noting that some areas seem to lack slow-slip events. In Chile, only one large SSE was recorded, happening prior to the $M_w 8.1$ Iquique megathrust event in 2014 (*Ruiz et al.*, 2014). In Japan for the subduction related to the pacific plate, a small number of them have been detected prior to the $M_w 9.0$ Tohoku megathrust (*Kato et al.*, 2012 ; *Ito et al.*, 2013) . In Sumatra, there were not any slow-slip ever recorded to my knowledge. Although GPS is still nowadays the main SSE detection tool, new observations tools now allow for a broader detection of slow-slip, like networks of sea-bottom pressure gauges (*Ito et al.*, 2013 ; *Wallace et al.*, 2016) or via the migration of microseismicity, repeating earthquakes and tremors

(*Igarashi et al.*, 2003 ; *Kato et al.*, 2012 ; *Kato and Nakagawa*, 2014), thus increasing significantly the probability of their detection.

At the same time in early 2000, analysts from the Japan Meteorological Agency (Japanese nationwide database for natural phenomena) started to see unknown signal in seismograms. They were observing low frequency signal, without any clear P-wave arrival although the S-arrival was clear. These events were called Low Frequency Earthquakes (LFE) (*Beroza and Ide*, 2011). Non-volcanic tremors were also discovered around the same time. Tremors are weak persistent signals of low frequencies. They were first discovered in south-west Japan (*Obara*, 2002). A year after, slow slip events and tremors were found to be associated in Cascadia (*Rogers and Dragert*, 2003). Tremors were found to correlate spatially and temporally with SSEs. This join phenomenon is called Episodic Tremor and Slip (ETS). ETS are also seen in southwest japan subduction zone (*Obara et al.*, 2004).

The attention in recent years, to observe above phenomena, was mainly focused on subduction zone. However slow-events also appear in continental systems. In San Andreas fault system, as mentioned previously, it is known since the 1960s that part of the fault are creeping continuously, parts are experiencing creep bursts, and some parts are blocked. Creep burst and sudden acceleration of slip were also discovered in other strike slip fault systems, like in Hayward fault, USA with creepmeters (*Lienkaemper et al.*, 1997) or using INSAR technics like in Haiyuan fault, China (*Jolivet et al.*, 2013) and in North Anatolian fault, Turkey (*Rousset et al.*, 2016). However there is still no clear evidence of propagation along strike of these slow-phenomena like it can be observed in subduction zones (*Rogers and Dragert*, 2003).

Interactions with earthquakes All these slow phenomena release stress accumulated during the inter-seismic period. This means that these slow phenomena have a mean positive stress drop (*Maury et al.*, 2014) although thought to be less than for earthquake (*Gao et al.*, 2012). However, they also participate in loading the system at their edge, so they can increase the probability of events (slow or fast). A complete detection and description of slow-slip events may help to characterize the stress state in the medium. It has been proposed that because of the sensitivity of slow slip to small stress changes, it can be used as stress meters (*Obara and Kato*, 2016). At

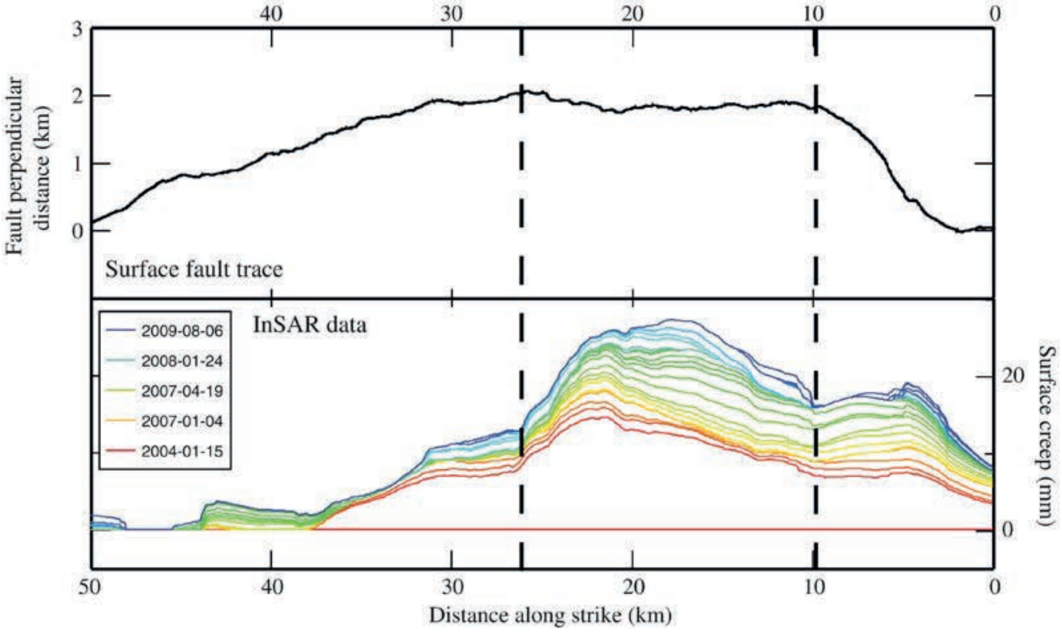

Figure 1.5 – Fault surface of the Haiyuan fault, China and the associated cumulative aseismic distribution of fault-parallel slip from *Jolivet et al.* (2015). Dash lines represent significant fault bends.

least two big megathrust events, seem to have been preceded by a slow slip event : the M_w9 Tohoku-Oki event (*Ito et al.*, 2013 ; *Mavrommatis et al.*, 2015) and the $M_w8.1$ Iquique event (*Ruiz et al.*, 2014 ; *Brodsky and Lay*, 2014). The $M_w7.3$ Papanoa earthquake in Guerrero, Mexico was apparently triggered by a large slow slip event detected geodetically. On the other part, there also exist a few examples of slow-events being triggered either by surface waves (*Itaba and Ando*, 2011 ; *Zigone et al.*, 2012) or by static stress transfer (*Kato and Nakagawa*, 2014).

In the previous section we showed that most earthquake happen in a context were multiple faults are there, and where the fault surfaces are not planar. It has been suggested that the slip due to aseismic creep burst correlates with the geometry of the fault (*Jolivet et al.*, 2015, Fig. 1.5). One can wonder to what extend the geometry can influence the absence or the presence of slow events. Can one trigger the other ? Are some places of the fault more likely to host slow events ?

1.3 Models of earthquake cycles

The mechanical models of earthquakes follows the three ingredient recipe : an elastic medium, a loading of the system, and a friction law. In this section, we will focus on models that incorporate restrengthening of the fault surface after an event. This condition allows for the simulation of a full seismic cycle including multiple events, with coseismic and inter-seismic periods.

Rate and state friction laws

Although Reid's theory was providing good results, the pattern of elastic radiation, explanation of surface ruptures, the behaviour of rock in laboratory experiments, some studies were challenging this idea. The relatively low stress drop observed for earthquakes was difficult to explain in the classical theory (*Brace and Byerlee*, 1966). *Brace and Byerlee* (1966), in their famous experiment, show that creating new fractures was not the only model that can explain earthquake faulting. In their experiment, they saw-cut a sample rock and load it at both ends with a confining pressure. They observed that the sliding between the two pieces of rocks was not smooth but rather in boom and bust motion. This was really the beginning of the well accepted theory of frictionally controlled earthquakes. As noted by *Scholz* (2002) in section 2.3 , the new emphasise of *Brace et al.* (1966) was not on a criteria for sliding (i.e. the strength of the material), but on the existence of a stability regime of a system. Friction is the resistance of motion that appears when two surfaces are in contact and slide one against the other. The two main characteristics of friction are : that the friction force is independent of the surface area of contact. The second main characteristic of friction is that friction force $\mathbf{F}_f$ is proportional with a constant f_0 to the normal force $\mathbf{F}_n$ that is applied (eq. (1.1)).

$$\mathbf{F}_f = f_0 \mathbf{F}_n \tag{1.1}$$

Early experiments showed that the static friction coefficient was actually different from the dynamic friction (*Rabinowicz*, 1958). The static friction has the property to increase with the logarithm of time, and the dynamic friction to depend on the velocity. *Rabinowicz* (1958), introduced a critical distance D_c to bridge the gap between the static friction and kinetic friction by linking them by $V = D_c/t$. Weakening friction laws were introduced to reproduce the earthquake behavior. They are called weakening because the friction decreases with the ongoing sliding (or sliding rate), making these friction laws able to lead to instabilities, i.e. earthquakes.

Dieterich (1979) in his work was the first to propose constitutive relationship to model velocity jump experiments. The experiment consisted of velocity jump, in a shear apparatus, of two ground surfaces of granodiorite. When a jump of slip velocity was suddenly applied, the friction coefficient showed a first increase, called the direct effect, and then relaxes toward a new steady state value (Fig. 1.6). Based on the previous experiments that showed increase in friction coefficient with increase time of contact (*Rabinowicz*, 1958), he interpreted the decrease in friction modulus with velocity as a effect of decrease in average contact time. For that purpose, he followed *Rabinowicz* (1958) by introducing a relaxation over the length scale D_c, that relates contact time t to sliding velocity V as following : $V = D_c/t$. This empirical law was the first to manage to reproduce qualitatively as well as quantitatively the friction jump experiment. It also unified the different static and dynamic friction coefficients into one rate dependent coefficient. This law was later improved by *Ruina* (1983), by introducing a state variable θ, that follows a evolution law. One common interpretation of this state variable θ is the life time of contact asperities. A modern form of this law was given by *Marone* (1998).

$$\tau^f = \sigma_n \left(f_0 + a \log\left(\frac{V}{V_0}\right) + b \log\left(\frac{\theta V_0}{D_c}\right)\right) \tag{1.2}$$

With either the aging state evolution law :

$$\dot{\theta} = 1 - \frac{\theta V}{D_c} \tag{1.3}$$

Or the slip evolution law :

$$\dot{\theta} = -\frac{V\theta}{D_c} \log\left(\frac{V\theta}{D_c}\right) \tag{1.4}$$

Nowadays, none of the state evolution reproduce the whole experimental data set. Slip law lacks the logarithmic time dependence of friction, if $V = 0$, θ does not evolve with time. This probably led modelers to favor the aging law (*Ampuero and Rubin*, 2008). However ageing law has a non symmetric response for velocity step experiment if we either increase or decrease the

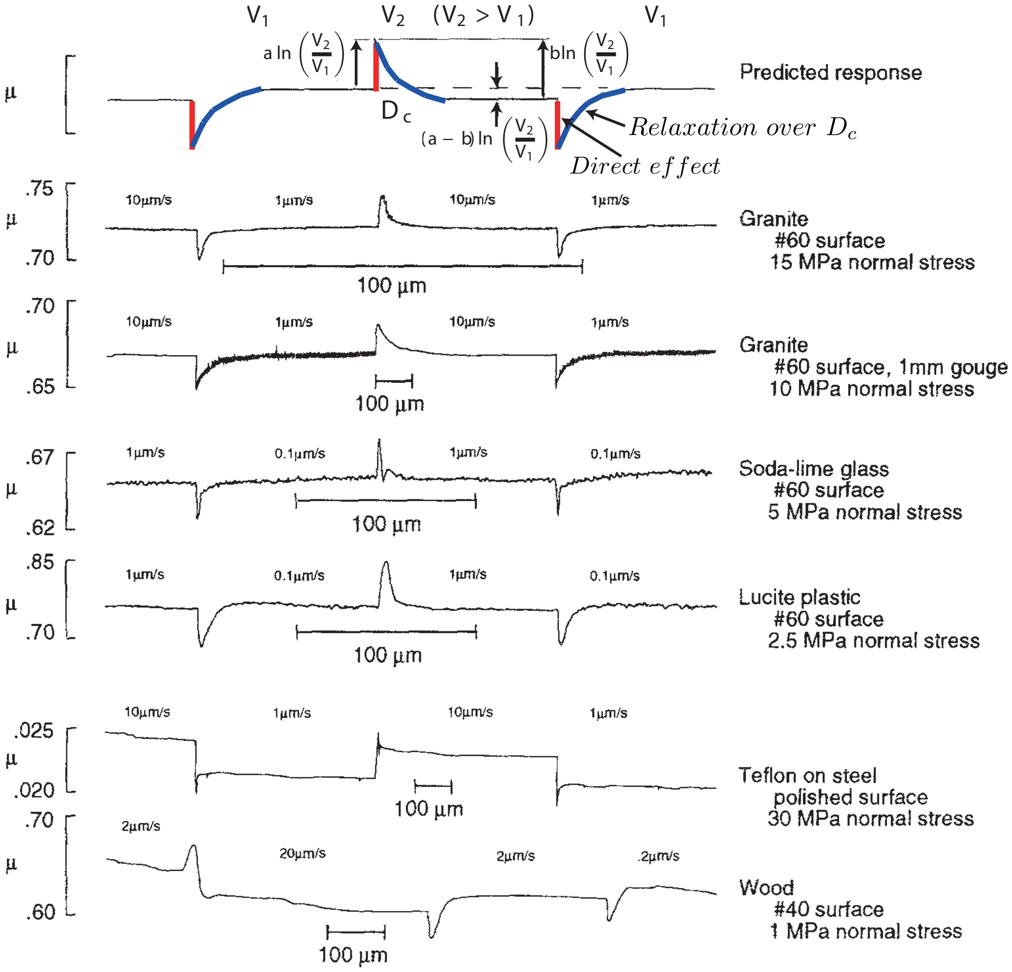

Figure 1.6 – The velocity stepping experiment for different materials from *Dieterich and Kilgore* (1994).

velocity (*Blanpied et al.*, 1998 ; *Ampuero and Rubin*, 2008). Several attempts have been made to improve the state evolution law, by introducing normal stress dependence (*Linker and Dieterich*, 1992), by proposing other forms of the state evolution (*Perrin et al.*, 1995 ; *Kato and Tullis*, 2001), by adding shear stress rate dependance (*Bhattacharya et al.*, 2015). Nethertheless, none of these laws have reached a consensus. Another promising improvement in friction laws is the add of other physic-based frictional mechanisms like dilatant strengthening (*Segall and Rice*, 1995 ; *Segall and Bradley*, 2012a) and thermal pressurisation (*Rice*, 2006 ; *Schmitt et al.*, 2011).

1.3.1 Spring slider models

Description of the model

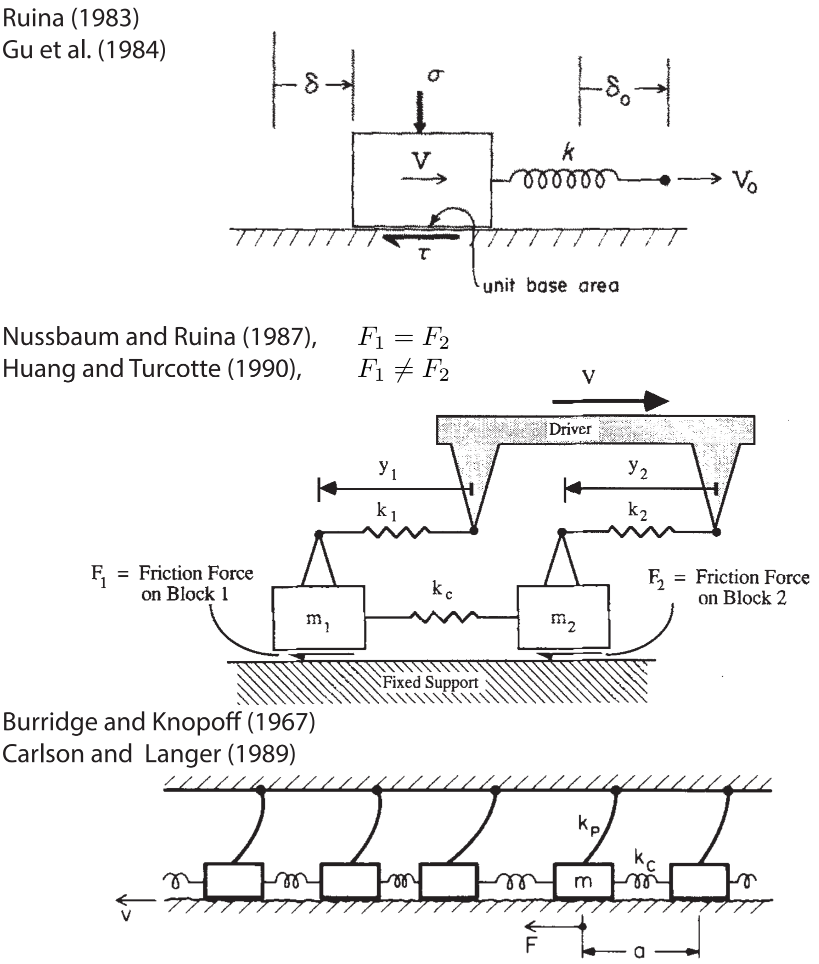

Figure 1.7 – Modified from *Nussbaum and Ruina* (1987), *Carlson and Langer* (1989) and *Gu et al.* (1984). This figure shows the different models of spring sliders used to mimic earthquake cycles.

Spring sliders, were for long used to conceptualise stick slip behaviour in rocks. One of the first mention of this analogy to earthquake can be find in the article of *Gilbert* (1884). It consists into a slider that is set down on a surface, and is dragged at constant velocity by a spring. A friction force is developed at the interface of the slider and the surface, and resists the movement of the slider. The stick slip behaviour coming from a model of a spring slider can be conceptualised by introducing two different friction coefficients, one that represents static friction and the other dynamic friction. Although this picture is now know to be incomplete, it is sufficient to understand the behaviour of stick slip. Suppose that the slider does not move, the spring is then loaded at a constant velocity, creating a force on the slider. The slider does not move until this force becomes greater than the frictional resistance, then the slider starts to move. Because the dynamic resistance is lower than the static resistance, an instability develops. When the spring is finally unloaded, the slider returns to rest, and the cycle continues. As we saw in previous section, it was for long known that dynamic and static friction were not equal to each other. In order to get more physical insight, one need to focus on the transition from a resting slider, to a dynamically moving slider. This can be done using the spring slider model together with a rate and state friction law.

Stability analysis

One of the most important question maybe in seismology is what does give rise to the instability, in other words, what would made a fault exhibit earthquakes instead of steady creeping. For spring-slider system in rate and state framework, this question has been answered, for both Ruina-slip state evolution law and Dieterich-aging state evolution law. The first linear stability analysis was done by *Ruina* (1983) for both slip and aging state evolution law. It was followed by a non linear stability analysis using Lyapunov function for slip law (*Gu et al.*, 1984), and for aging law (*Ranjith and Rice*, 1999). The main result of their analysis was the existence of the same critical stiffness of the spring for both state evolution laws :

$$k_c = \sigma_n(b-a)/D_c \tag{1.5}$$

For the aging law, the non linear analysis showed that if the stiffness of the spring is greater than this critical stiffness $k > k_c$, then the system is stable for any finite perturbation. For the slip law, the non linear analysis showed that for $k > k_c$, the system is conditionally stable. In other words, this means that for aging law, any perturbation to a stable system will return to the creep behaviour, whereas for slip law, strong enough perturbation in a stable system may lead to a stick-slip behaviour.

Phenomenology

An interesting feature of spring slider models is that they show very complex spacio-temporal behaviour as soon as two spring sliders are connected through a spring to each other. Two spring sliders connected to each other with total symmetry shows asymmetry in their behaviour : either a global complete event including the two sliders with always the same first block to move or global complete events with alternating first block to move (*Nussbaum and Ruina*, 1987). When the symmetry is broken by putting different frictional responses of the two blocks, the behaviour of the two blocks can be chaotic (*Huang and Turcotte*, 1990). The Buridge-Knopoff model consists into several spring sliders that are all linked to each other through a spring. This model was able to mimic Gutenberg-Richter scaling law, and also Omori's law (*Burridge and Knopoff*, 1967). It consists into assembling several sliders in series, each of them being link to its neighbours by a spring (see Fig. 1.7). Although these models can reproduce some of the statistics of earthquakes, one has to be careful with extrapolating ideas from this kind of models. Obviously there is no wave propagation in the spring slider model. Another criticism is that it was thought that increasing the order of the system will lead to more spatio-temporal complexity of the response (*Huang and Turcotte*, 1990), however it seems not to hold always true. *Rice* (1993) showed that when a continuous system is correctly discretised in rate and state framework, the behaviour of the system can be less complex than the discretised system. *Madariaga et al.* (1992) also showed that when increasing the number of sliders with a specific rate weakening friction, the system can lose its ability to reproduce correctly scaling laws.

1.3.2 Continuum models

Evolution of spring slider models

Continuum models benefits a lot from the development of numerical methods like finite differences, finite elements, boundary element method. It was expected that the complexity coming from multiple spring sliders simulation will show up even strongly in continuum models (*Carlson and Langer*, 1989 ; *Huang and Turcotte*, 1990). However, this was shown not to be the case for correctly discretized continuum models with rate and state friction law (*Rice*, 1993).

Stability analysis

The same question is raised as for spring sliders : what would make a continuous fault unstable ? Although the general answer is unavailable in the framework of rate and state, it is possible to infer a length scale in some limiting cases for simple straight continuum faults with homogeneous frictional parameters. The first nucleation length-scale derived for continuous fault came from the spring slider modelling. If it is assumed that the stiffness of a fault k_{fault} is inversely proportional to its length, we can derive a nucleation length scale L_{nuc} (*Rice*, 1992). At the critical length L_{nuc}, the stiffness of the fault equals the critical stiffness derived from a spring slider (*Rice*, 1992).

$$k_c = \sigma_n \frac{b-a}{D_c} = \frac{\mu}{L_{nuc}} = k_{fault} \tag{1.6}$$

Thus,

$$L_{nuc} = \frac{\mu D_c}{\sigma_n (b-a)} \tag{1.7}$$

By studying the nucleation on fault with rate and state resistance, Dieterich derived another nucleation length scale L_b inversely proportional to the friction parameter b (*Dieterich*, 1992).

$$L_b = \frac{\mu D_c}{\sigma_n b} \tag{1.8}$$

More recent work shows that the nucleation actually depends on the ratio a/b (*Rubin and Ampuero*, 2005 ; *Ampuero and Rubin*, 2008 ; *Viesca*, 2016). *Rubin and Ampuero* (2005) first derived analytical solution in the limiting case where $V\theta/D_c >> 1$ for the aging state evolution law. They showed that this assumption would remain valid only if the ratio $a/b < 0.3781$. For high a/b however, they pointed out that the coefficient $V\theta/D_c$ was nearly constant at the interior of the nucleation patch. Using that as an assumption, with energetic consideration, they were able to derive another expression for the nucleation length scale when a/b approaches 1. We can summarize their result by :

$$\begin{cases} L_{nuc} = 2 * 1.3774 * L_b & 0 \leq a/b < 0.3781 \\ L_{nuc} = 2 * \dfrac{L_b}{\pi(1-a/b)^2} & a/b \to 1 \end{cases} \tag{1.9}$$

The nucleation length scale found by *Rubin and Ampuero* (2005), was later shown to hold true by recasting the system of equations to look for instabilities and doing a linear perturbation analysis of these instabilities (*Viesca*, 2016). The figure 1.8 shows simulation of slip evolution for different values of length of the fault, and ratio a/b. The fault is straight and single. In that particular setting, we see that the nucleation length scale given by equation 1.9 provides very good results (Fig. 1.8).

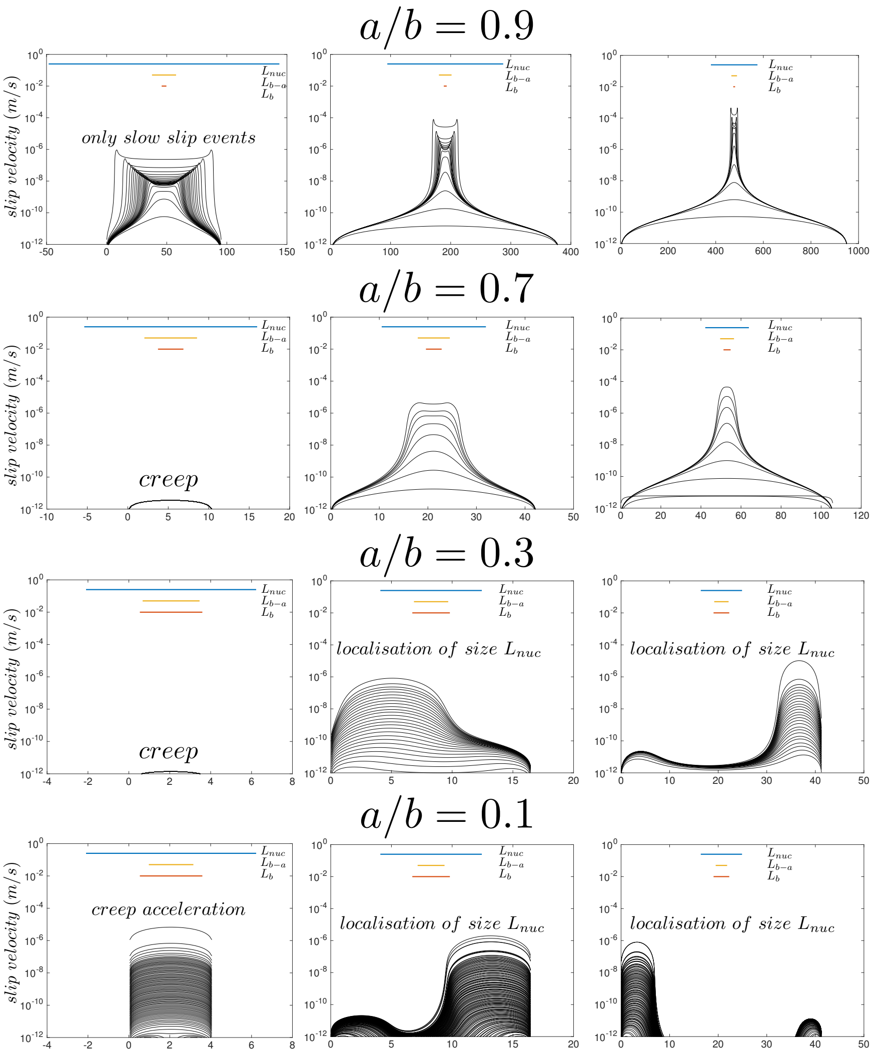

Figure 1.8 – Slip velocity in logarithmic scale for quasi-dynamic simulations. The three nucleation length scales are shown for various length of the fault.

1.4 Spatio-temporal complexities in earthquake cycle modeling

In the introduction, we saw that the faulting origin of earthquakes, and their modelling, mainly rely on our comprehension of the three ingredients (elastic medium, loading, frictional resistance) that are needed for earthquakes. The 19th century marked a great improvement in our understanding of earthquakes. The beginning of the 21th century, with the discovery of slow phenomena, improved a lot our understanding of the seismic cycle. We now know that a fault can dissipate a non-negligible part of the accumulated stress a-seismically. This is of particular importance because it means that slow-events must be accounted in slip budget on fault systems together with earthquakes. However the diversity of slip events, and the complexity of the seismic cycles remains difficult to model and to explain. The fact that earthquake does not rupture the entire fault, that some ruptures show complex pattern of acceleration and deceleration, the interplay between slow and fast dynamics, and between network of faults, is not emerging naturally with single planar fault system with homogenous rheology (i.e. friction parameters) (*Rice*, 1993). Therefore this model needed some improvement to be able to reproduce natural seismicity. A possible candidate that can bring this complexity would be the actual geometry of fault networks. We saw that faults are rarely planar and isolated, but are rather rough and acting in networks. The effect of this natural complexity of fault networks have been poorly studied mainly because of the limitation of computational resources. Since the earlier work of *Liu and Rice* (2005, 2007), it is known that a simple way to obtain both slow and fast dynamic on a fault is to adjust the length of the fault to be close to the nucleation length scale (*Rubin*, 2008). This size of the patch to nucleation length scale appear to be the main controlling parameters in many studies (*Rubin and Ampuero*, 2005 ; *Rubin*, 2008 ; *Viesca*, 2016). These studies were able to explain and reproduce many of the observed complexities like interplay between slow and fast events (*Liu and Rice*, 2005, 2007 ; *Rubin*, 2008 ; *Veedu and Barbot*, 2016), repeaters (*Chen and Lapusta*, 2009), partial ruptures (*Chen and Lapusta*, 2009 ; *Michel et al.*, 2017). However, the controlling parameter in these simulation is also the limiting parameter of the studies, slow events are not emerging if this ratio is to large and this appears contradictory to the nearly ubiquitous detection of slow events. One way to overcome this issue was to appeal to other frictionnal mechanism like dilatent strenghtening (*Segall and Rice*, 1995 ; *Rubin*, 2008 ; *Segall et al.*, 2010) that stabilize the rupture at intermediate slip-velocity.

The goal of this thesis is to show that networks of faults, and geometrical complexities when correctly accounted can also produce a wide range of complex slip behavior, and even more that they are necessary to take into account if we want to fully understand the seismic cycle. We will see in this thesis that only appealing to geometrically complex networks of faults without any variation in rheology is sufficient to reproduce earthquakes, slow events, partial ruptures and aperiodicity of the seismic cycles. For that purpose we will use two recently developed methods, Fast Multipole Method and H-matrices, that can accelerate the computation time significant enough to account for a myriad of complex fault networks. This work can be thought as a continuation of many other works, that focus more on interaction of asperities and statistics (*Dublanchet et al.*, 2013), effect of stress perturbation from another fault and emergence of slow events (*Liu and Rice*, 2007), and more generally the effect of geometry on the seismic cycle (*Li and Liu*, 2016).

This thesis is organized as followed : Section II is a description of the quasi-dynamic model for both in plane and out of plane elasticity, with rate and state friction law. We also described two new methods : Fast Multipole Method and H-matrices that can accelerate the calculation, without any limitation on the geometry of the faults, hence allowing for relatively fast long term simulation of the seismic cycle. Section III is an exploration of the parameter space of a system of two overlapping faults. In this section, we show that even one of the most basic geometrical complexity (two overlapping faults), can give rise to several modes of slip including creep burst, slow and fast events, partial ruptures, afterslips and apparent chaotic behavior of the seismic cycle. Moreover, taking advantage of the fast methods depicted in section II, we were able to do some statistics on the events that were emerging in our simulation, and we showed that the moment of slow and fast events follow the scaling law discovered by *Ide et al.* (2007). Section IV is a demonstration of the power of our methodology on three different topics. 1) We explore the effect of self-similar geometrical roughness of faults on the seismic cycle. We show that the behavior of the seismic cycle differs greatly if we consider in-plane or out-of-plane elasticity, and that the roughness of fault may provide an appealing explanation for size distribution of earthquakes. 2) We ran fluid injection simulation, by using pore pressure diffusion, and showed that this is perturbing the seismic cycle of the fault. 3) We ran seismic cycle simulation on a real fault network from the the eastern California shear zone area (*Sowers et al.*, 1994).

Chapitre 2

Fast methods for quasi-dynamic earthquake cycles in 2D non planar geometries

Avant-propos

Ce chapitre présente le modèle utilisé dans le reste de cette thèse. Dans un premier temps, nous introduisons brièvement les équations intégrales de frontière, en élasticité plane. Ces équations intégrales sont en fait la solution analytique (sous forme d'intégrale) du problème d'élasticité dont le glissement ou les contraintes sont connus sur la l'élément frontière (la faille). Cette intégrale est ensuite discrétisée pour pouvoir être intégrée numériquement. Ce type d'approche présente plusieurs avantages : tout d'abord, la convergence est très bonne parce que la solution provient de la discrétisation d'une solution analytique. Ensuite, il n'y a pas de difficulté de maillage, car seulement la faille nécessite d'être maillée. Finalement, cette approche se marie très bien avec la résolution d'un problème de type "rate and state", si l'on ne s'intéresse qu'à la partie quasi-dynamique. En effet, dans ce cas particulier, la solution de ce problème peut se réécrire sous la forme d'un système d'équations différentielles ordinaires, ce qui se prête très bien à la résolution avec un solveur à pas de temps variable de type Runge-Kutta ou Bulirsch-Stoer. Néanmoins cette méthode présente des défauts : elle nécessite la connaissance de la fonction de Green du problème ce qui limite l'utilisation de la méthode des éléments frontières à des cas simples de type milieu infinis et homogènes. La deuxième difficulté est que la résolution du problème est couteuse en terme de temps de calcul. En effet, le temps de calcul croit avec le carré de la taille du problème, ce qui signifie par exemple que doubler la longueur d'une faille, multipliera par quatre le temps de calcul. Cependant ce dernier point peut être résolu en faisant appel à des méthodes accélératrices comme la méthode Multipolaire Rapide ou les matrices hiérarchiques. La présentation de ces méthodes représente le coeur de ce chapitre. Elles permettent une diminution drastique du temps de calcul de la méthode des éléments frontières tout en gardant une excellente précision. Dans l'avant dernière section de ce chapitre nous présentons comment sont réalisés le chargement et l'inclusion de la loi de friction. Pour clore ce chapitre, nous démontrons la robustesse de notre méthode par une comparaison de la vitesse (avec et sans méthode accélératrice), et nous comparons aussi la précision de notre méthode par rapport à une solution analytique.

2.1 Introduction

The complexity that arises on fault systems is extraordinary rich in behaviour, spanning several orders of magnitude in space, from micro-seismicity to large megathrust earthquakes, and in time, from seconds for earthquake to years for slow-slip phenomena. The space-time occurrence of earthquakes also show complexities. For decades, earthquake models have tried to capture this complexity. The rate and state framework (*Dieterich*, 1979 ; *Ruina*, 1983), that formulates a law for the frictional strength of the fault and the recovery of this strength after an earthquake, has helped a lot to understand the temporal complexity of earthquakes.

In earthquake mechanics, many numerical methods have been used to solve the governing elastodynamics equation, together with friction laws and specific boundary conditions (free surface, layered medium). The first numerical methods used were finite difference methods (for e.g. *Andrews*, 1976 ; *Madariaga*, 1976 ; *Virieux and Madariaga*, 1982), and we can cite among others the finite element (*Melosh and Raefsky*, 1981), method and the spectral element method (*Komatitsch and Vilotte*, 1998). All these methods are based on a discretisation of the entire volume. The Boundary Element Method (BEM) is a numerical method based on the discretisation of a boundary integral equation. Contrary to the previous methods, the BEM requires only the discretisation of the boundary of the volume (i. e. faults), which makes it easier to capture complex fault geometries. Usually a boundary element equation for the static stress change due to slip on a fault can be represented as :

$$\tau(\mathsf{x}) = \int_\Gamma K(x,\xi) f(\xi) \mathrm{d}\xi \tag{2.1}$$

Where f is a function of the gradient of the slip for the elasto-static problem $f(\xi) = \partial \Delta u(\xi)/\partial \xi$. The kernel, $K(x,\xi)$, depends on the geometry and the kind of problem we are solving. And Γ is the boundary of the system, it is the fault in our particular case. This representation becomes a double convolution over time and space for the dynamic problem.

Boundary integral equations were first introduced in the sixties to solve 2D potential problem (*Jaswon and Ponter*, 1963 ; *Symm*, 1963 ; *Jaswon and Ponter*, 1963). Since then, it has undergone rapid development, and was quickly applied in crack propagation problems (*Kostrov*, 1966 ; *Burridge*, 1969), in 2D planar, anti-plane stress and strain configuration. The regularised BEM for elastodynamics in 2D for a general geometry in in-plane stress and strain was developed by *Tada* (1995). Five years later, he generalised it into 3D infinite elastic medium (*Tada and Madariaga*, 2001).

The main advantage of BEM is the ease of meshing faults as it only requires to mesh the boundary surface i.e. the fault surface. Another advantage of this method is its accuracy, and convergence. Indeed, the boundary element method is based on a semi-analytical (meaning an analytical solution in a form of an integral), hence if integration is done carefully, it naturally converges towards the solution. Finally one of the other advantage is that solving a elasto-quasidynamic BEM with a rate-and-state friction law, it can be recast as a set of ordinary differential equations. A set of ordinary differential equation (ODE) is particularly well suited for the modelling of earthquake cycle because we can use very effective adaptive step-size solvers like Runge Kutta (*Press et al.*, 1993 ; *Stuart and Tullis*, 1995 ; *Liu and Rice*, 2005) or Bulirsch-Stoer method (*Bulirsch and Stoer*, 1966). Adaptive time step is needed if we want to keep a good accuracy during earthquakes, and to be able to march through inter-seismic period.

However this method has two main drawbacks : first, it requires the knowledge of the Green's function. Unfortunately, Green's functions are only available for simple settings like infinite homogeneous medium. For more complicated medium, we need to precompute numerically the Green's function. The second drawback of this method is that is requires the computation of fully populated matrices, making all big problems, computationally out of reach. However this last point can be compensated by accelerating methods (*Greengard and Rokhlin*, 1987 ; *Carrier et al.*, 1988 ; *Hackbusch*, 1999). The kernel in elasticity is generally smooth at the far field so that methods like Fast Multipole Method or Hierarchical matrices can be used to accelerate the calculation. Fast multipole method was applied successfully to elasto-static 3D crack problems (*Nishimura et al.*, 1999 ; *Yoshida et al.*, 2001), and to seismic cycle modelling (*Hirahara et al.*, 2009). H-matrix has already been used in the context of quasi dynamic modelling of subduction zone faults (*Ohtani et al.*, 2011).

2.2 Boundary Integral Equation for planar elasticity

Representation Theorem

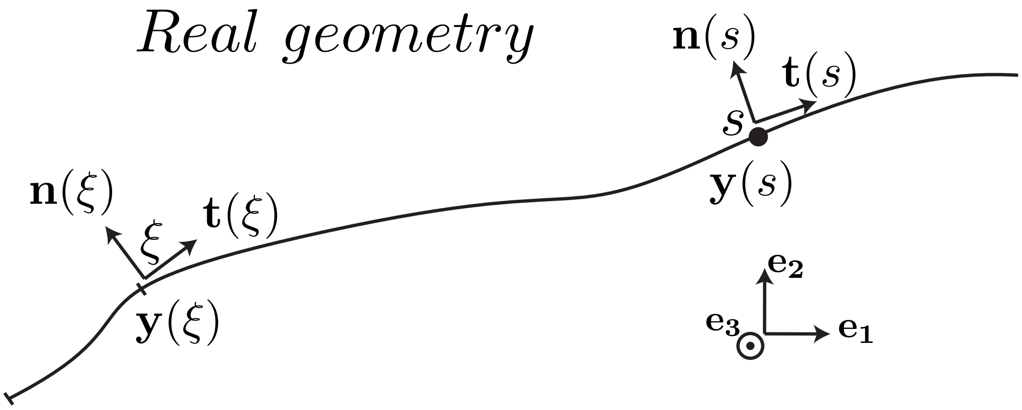

Figure 2.1 – The fault geometry and associated parameters that are needed for equation 2.3

One fundamental question in seismology is probably the following, knowing the displacement or the traction along a fault, and a fundamental response of earth, is it possible to infer the displacement everywhere else at any time ? A solution to that problem comes from the representation theorem, that relates the displacement everywhere, and at any time, to the displacement and traction on the boundary of the system. This theorem is derived from Betty's reciprocal theorem. If we now consider a fault with a slip distribution $\Delta u(\xi) = u^+ - u^-$, where ξ represent the curvilinear abscise on the fault, $u^+(\xi)$ and $u^-(\xi)$ represent respectively the upper/lower side displacement of the fault, the representation theorem for a fault with a slip distribution becomes (*Aki and Richards*, 2002 ; *Udías et al.*, 2014) :

$$\begin{aligned} u_n(\mathbf{y}(s)) &= \int_\Gamma \Delta u_i(\mathbf{y}(\xi)) c_{ijkl} n_j(\xi) \frac{\partial}{\partial y_l(\xi)} G_{nk}(\mathbf{y}(s), \mathbf{y}(\xi)) \mathrm{d}\xi \\ &= -\int_\Gamma \Delta u_i(\mathbf{y}(\xi)) c_{ijkl} n_j(\xi) \frac{\partial}{\partial y_l(s)} G_{nk}(\mathbf{y}(s), \mathbf{y}(\xi)) \mathrm{d}\xi \end{aligned} \tag{2.2}$$

Where s is the curvilinear abscise at the evaluation point. $\mathbf{y}(s)$ is the location of the point s in the global coordinate system $(\mathbf{e_1}, \mathbf{e_2}, \mathbf{e_3})$. u_n represents the n'th component of displacement. $\mathbf{n}(\xi)$ and $\mathbf{t}(\xi)$ are respectively the normal and tangential vector to the fault at point ξ. Their component in the global coordinate system are written with the corresponding subscript.

In this representation (that represents the displacement field due to a slip distribution on a fault), $G_{ni}(\mathbf{x}, \mathbf{y})$ is the n component of the displacement at location **x**, due to a Dirac volume force in the ith direction at location **y**. This function G is the so called Green's function. Because there is a one to one connection with the curvilinear abscise and the position on the fault $s \leftrightarrow \mathbf{y}(s)$, we will write $\tau(s)$ and $G(s, \xi)$ instead of $\tau(\mathbf{y}(s))$ and $G(\mathbf{y}(s), \mathbf{y}(\xi))$. c_{ijkl} is the stiffness tensor that links the stress tensor to the strain tensor for elastic linear material (Hooke's law). Although this theorem is very general, it is only useful when we can derive the Green's function that characterises the medium. Unfortunately, these Green's functions have only known analytic solutions in a few restrictive cases, like an infinite elastic medium in 3D or in 2D. For more complex medium, for example with a free surface, these Green's functions have to be computed numerically. We can now derive the stress field from the displacement field. For this purpose, we apply the Hooke's law (*Tada*, 1995 ; *Tada and Yamashita*, 1997) :

$$\begin{aligned} \sigma_{kl}(\mathbf{x}) &= \frac{1}{2} c_{klrs} \left(\frac{\partial u_s}{\partial x_r} + \frac{\partial u_r}{\partial x_s} \right) \\ &= -\int_\Gamma \Delta u_i(\xi) c_{ijpq} n_j(\xi) \frac{\partial}{\partial x_q} \Sigma_{klp}(\mathbf{x}, \mathbf{y}) \mathrm{d}\xi \end{aligned} \tag{2.3}$$

Where,

$$\Sigma_{klp}(\mathbf{x},\mathbf{y}) = c_{klrs}\frac{\partial}{\partial x_s}G_{rp}(\mathbf{x},\mathbf{y}) \tag{2.4}$$

Conservation of linear momentum for Green's function $\forall(i,k)$:

$$\frac{\partial}{\partial x_j}\Sigma_{ijk} = 0 \tag{2.5}$$

Although this representation theorem may seem easy to use, it is not as straight forward. Indeed, a naive replacement of Green's function by their analytical formulation for infinite elastic medium leads to hyper-singular integral (also called Hadamard finite part integral). These integrals are naturally diverging. However they can regularised by modifying the singular term (*Sladek and Sladek*, 1984 ; *Koller et al.*, 1992) into a weaker singular form known as Cauchy principal value. An approach to regularise these hyper-singular integrals is to perform an integration by parts (*Tada*, 1995 ; *Tada and Yamashita*, 1997).

Boundary Integral Equation for anti-plane strain and stress

In the particular case of out-of-plane strain, the only non-zeros displacement is Δu_3. This results in only two non-zeros stress components : σ_{32} and σ_{31}. The Green's function for an infinite medium expresses as :

$$G_{33}(\mathbf{x},\mathbf{y}) = \frac{-\log(r)}{2\pi\mu} \tag{2.6}$$

Where $r = |\mathbf{x}-\mathbf{y}|$ is the distance between $\mathbf{x}$ and $\mathbf{y}$, μ is the shear modulus. If we inject that expression and regularise the hyper-singular integral obtained in eq. (2.3), we get the shear traction on the fault (*Tada and Yamashita*, 1997) :

$$\begin{aligned}\tau_3(s) &= \mathbf{e}_3\cdot\overline{\overline{\sigma}}(\mathbf{y}(s))\cdot\mathbf{n}(s)\\ &= \int_\Gamma K_{III}(s,\xi)\frac{\partial}{\partial\xi}\Delta u_3(\xi)\mathrm{d}\xi\end{aligned} \tag{2.7}$$

Where :

$$K_{III}(s,\xi) = \frac{\mu}{2\pi}\left(n_1(s)\frac{\gamma_2}{r} - n_2(s)\frac{\gamma_1}{r}\right) \tag{2.8}$$

and $\gamma_1 = \mathbf{e_1}\cdot\dfrac{\mathbf{y}(s)-\mathbf{y}(\xi)}{r}$ and $\gamma_2 = \mathbf{e_2}\cdot\dfrac{\mathbf{y}(s)-\mathbf{y}(\xi)}{r}$

Boundary Integral Equation for in plane strain and stress

In the particular case of in plane strain, the two values $u_1(\mathbf{y})$ and $u_2(\mathbf{y})$ are non-zeros displacements. For convenience we will note the tangential slip on the fault $\Delta u_t(s) = \mathbf{t}(s) \cdot \Delta\mathbf{u}(s)$ (*Tada and Yamashita*, 1997). For in-plane strain, we have this time four components of the Green's function :

$$\begin{aligned} G_{11}(s,\xi) - G_{22}(s,\xi) &= \frac{1}{4\pi\mu}\left[\left(\frac{c_s^2}{c_p^2} - 1\right)(\gamma_2^2 - \gamma_1^2)\right] \\ G_{11}(s,\xi) + G_{22}(s,\xi) &= \frac{1}{4\pi\mu}\left[\left(1 - \frac{c_s^2}{c_p^2}\right) - 2\left(1 + \frac{c_s^2}{c_p^2}\right)\log(r)\right] \\ G_{12}(s,\xi) &= \frac{1}{4\pi\mu}\left(1 - \frac{c_s^2}{c_p^2}\right)\gamma_1\gamma_2 \\ G_{33}(s,\xi) &= \frac{-2}{4\pi\mu}\log(r) \end{aligned} \tag{2.9}$$

Where c_p and c_s are respectively the dilatational and shear wave speed of the medium. Again if we regularised and inject the Green's function in eq. (2.3)(*Tada and Yamashita*, 1997) :

$$\begin{aligned} \tau_t(s) &= \mathbf{t}(s) \cdot \overline{\overline{\sigma}}(\mathbf{y}(s)) \cdot \mathbf{n}(s) \\ &= \int_\Gamma K_{II}^t(s,\xi)\frac{\partial}{\partial\xi}\Delta u_t(\xi)\mathrm{d}\xi \end{aligned} \tag{2.10}$$

$$\begin{aligned} \tau_n(s) &= \mathbf{n}(s) \cdot \overline{\overline{\sigma}}(\mathbf{y}(s)) \cdot \mathbf{n}(s) \\ &= \int_\Gamma K_{II}^n(s,\xi)\frac{\partial}{\partial\xi}\Delta u_t(\xi)\mathrm{d}\xi \end{aligned} \tag{2.11}$$

Where the kernels are :

$$\begin{aligned} K_{II}^t(s,\xi) = \frac{\mu}{\pi}\left(1 - \frac{c_s^2}{c_p^2}\right)\Big\{&[4n_1(s)n_2(s)\gamma_1\gamma_2 + (n_2^2(s) - n_1^2(s))(\gamma_2^2 - \gamma_1^2)]\times \\ &\times\left(n_2(\xi)\frac{\gamma_1}{r} - n_1(\xi)\frac{\gamma_2}{r}\right)\Big\} \end{aligned} \tag{2.12}$$

$$\begin{aligned} K_{II}^n(s,\xi) = \frac{\mu}{\pi}\left(1 - \frac{c_s^2}{c_p^2}\right)\Big\{&\left(n_1(\xi)\frac{\gamma_1}{r} + n_2(\xi)\frac{\gamma_2}{r}\right) + \\ &+ [2n_1(s)n_2(s)(\gamma_2^2 - \gamma_1^2) - 2(n_2^2(s) - n_1^2(s))\gamma_1\gamma_2]\Big\} \end{aligned} \tag{2.13}$$

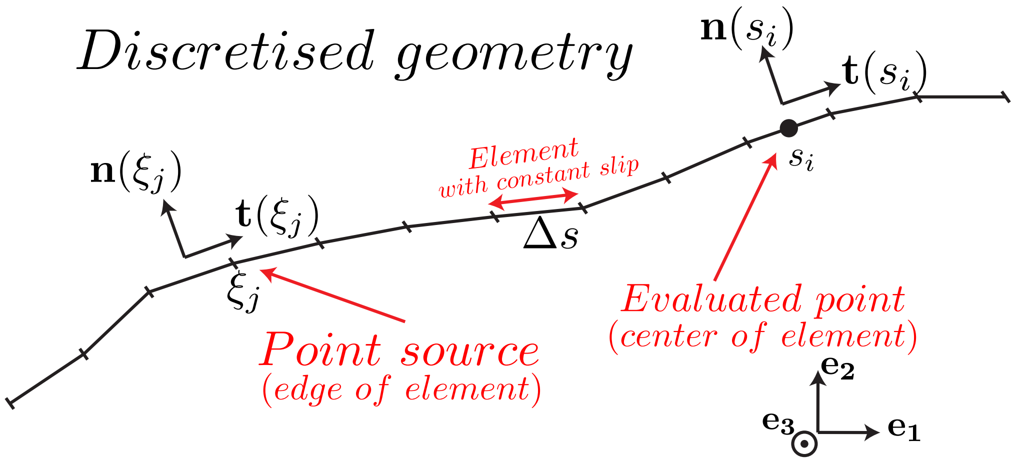

Figure 2.2 – Discretised version of the real fault geometry.

2.2.1 Numerical calculation

In order to evaluate the previous singular integrals in the sense of Cauchy principal values, we will assume piece-wise constant slip over fixed length Δs, centred on **y**(s_i). The slip is discretised as follows (see Fig. 2.2)(*Rice*, 1993 ; *Cochard and Madariaga*, 1994) :

$$\Delta u(s) = \sum_{j=1}^{N} \Delta u(s_j)[\mathcal{H}(s - s_j + \Delta s/2) - \mathcal{H}(s - s_j - \Delta s/2)] \tag{2.14}$$

Where $\mathcal{H}$ is the Heaviside function and N is the number of elements used to discretise the fault. Then the boundary element integral 2.1 becomes a summation :

$$\tau(s_i) = \sum_{j=1}^{N} [K(s_i, \xi_{j+1}) - K(s_i, \xi_j)]\Delta u_j \tag{2.15}$$

The naive implementation of that problem requires to calculate for each $\tau(s_i)$ (N terms) a sum over N terms (for each j), which leads to a computational complexity of $\mathcal{O}(N^2)$. It means that the time required to compute numerically this problem will grow with the square of the problem size. This makes large problems difficult to handle with a naive implementation. However, most of the time in elasticity, the kernel K is smooth when the source point **y**(ξ_j) is far enough from the evaluated point **y**(s_i), or in other words :|**y**$(s_i) -$ **y**$(\xi_j)| >> 1$.

2.3 Fast Fourier Transform

In the particular case of a flat fault, the aforementioned expressions for shear traction can be simplified :

$$\tau_t(x) = \frac{\mu}{2\pi\epsilon}\int_\Gamma \frac{1}{x-\xi}\frac{\partial}{\partial\xi}\Delta u_t(\xi)\mathrm{d}\xi \tag{2.16}$$

Here $\epsilon = 1$ for out of plane formulation, and $\epsilon = 1-\nu$, ν being Poisson's ratio, for in plane formulation. The normal traction due to a slip distribution in in-plane elasticity is zero for the special case where the fault is planar, $\tau_n = 0$. We can recognise here an Hilbert transform of the gradient of slip distribution on the fault. Using the properties of Fourier transform $\mathcal{F}$, it is possible to simplify the calculation of the traction (*Segall*, 2010) : The Fourier transform of a convolution of two functions f and g is the product of the Fourier transform of the functions.

$$\mathcal{F}(f * g) = \mathcal{F}(f)\mathcal{F}(g) \tag{2.17}$$

The derivative is simplified :

$$\mathcal{F}\left(\frac{\partial}{\partial\xi}\Delta u_t(\xi)\right) = ik\mathcal{F}(\Delta u_t(\xi)) \tag{2.18}$$

The Fourier transform of $\frac{1}{x}$ has an analytical form :

$$\mathcal{F}\left(\frac{1}{x}\right) = -i\pi\mathrm{sgn}(k) \tag{2.19}$$

Finally, we get :

$$\mathcal{F}(\tau_t) = -\frac{\mu}{2}|k|\mathcal{F}(\Delta u_t) \tag{2.20}$$

The power of this method is that the Fourier transform can be evaluated with a Fast Fourier Transform method (FFT). This algorithm, allows to decrease the complexity of the algorithm from $\mathcal{O}(N^2)$ to $\mathcal{O}(N\log N)$. This method is widely used in earthquake cycle simulators (*Perrin et al.*, 1995 ; *Liu and Rice*, 2005 ; *Segall*, 2010 ; *Dublanchet et al.*, 2013). However this methods requires two assumptions to be valid, the fault has to be infinite with periodic replication of the behaviour, and the fault has to be planar. This drawback arises because of the necessity for equispaced discretisation when one uses FFT. This makes the FFT method inappropriate for modelling complex geometrical problems, or even multiple fault systems.

2.4 Fast Multipole Method

Another method which can accelerate the computation of summation (eqn. 2.15) is the Fast Multipole Method (FMM). This method was initially used in astrophysics to overcome the complexity of calculation of $N - body$ problems. FMM was first introduced by *Greengard and Rokhlin* (1987). Because of the analogy of the static elastic kernel in mode III and the gravity potential in 2D for N planets of mass m_i located at $\mathbf{x_i}$ ($\phi_{grav}(\mathbf{x}) = \sum_{i=1}^{N} m_i \log \|\mathbf{x} - \mathbf{x_i}\|$), we can use Fast multipole method to accelerate the calculation of the kernel. The fast multipole method is based on four steps : (1) Create a quadtree structure with the position of particles (here these are the fault nodes). (2) Find cluster of particles that are interacting with each other and can be simplified. (3) Do a multipole expansion of group of points that are close enough (we will explicit mathematically what does "close enough" mean in the following section). (4) Do a local Taylor series expansion for the far field of the multipole points.

Instead of calculating each point to point interaction, FMM creates cluster of particles and summarise the effect of the cluster in only one point (an analogy would be calculating a centre of mass). This is what is called the multipole expansion. The local expansion is a way to sum up all the far field interactions coming from all the far cluster of particles.

Mode III

In mode III the shear stress can be easily written in term of a potential on the fault $\phi(s)$:

$$\begin{aligned}
\tau_3(s) &= \frac{\mu}{2\pi}\int_\Gamma \frac{\partial}{\partial\xi}\Delta u_3(\xi)\left[n_1(s)\left(\frac{y_2(s)-y_2(\xi)}{r^2}\right) - n_2(s)\frac{y_1(s)-y_1(\xi)}{r^2}\right]\mathrm{d}\xi \\
&= \frac{\mu}{2\pi}\int_\Gamma \frac{\partial}{\partial\xi}\Delta u_3(\xi)\left[n_1(s)\left(\frac{\mathbf{y}(s)-\mathbf{y}(\xi)}{r^2}\cdot\mathbf{e}_2\right) - n_2(s)\left(\frac{\mathbf{y}(s)-\mathbf{y}(\xi)}{r^2}\cdot\mathbf{e}_1\right)\right]\mathrm{d}\xi \\
&= -\frac{\mu}{2\pi}\mathbf{t}(s)\cdot\int_\Gamma\left(\frac{\partial}{\partial\xi}\Delta u_3(\xi)\right)\left(\frac{\mathbf{y}(s)-\mathbf{y}(\xi)}{r^2}\right)\mathrm{d}\xi \\
&= -\frac{\mu}{2\pi}\mathbf{t}(s)\cdot\int_\Gamma\left(\frac{\partial}{\partial\xi}\Delta u_3(\xi)\right)\nabla_{\mathbf{y}(s)}(\log\parallel\mathbf{y}(s)-\mathbf{y}(\xi)\parallel)\mathrm{d}\xi \\
&= -\frac{\mu}{2\pi}\mathbf{t}(s)\cdot\nabla_{\mathbf{y}(s)}\left[\int_\Gamma\left(\frac{\partial}{\partial\xi}\Delta u_3(\xi)\right)\log\parallel\mathbf{y}(s)-\mathbf{y}(\xi)\parallel\mathrm{d}\xi\right] \qquad (2.21)
\end{aligned}$$

After discretising, the integral becomes :

$$\tau_3(s) = \frac{\mu}{2\pi}\mathbf{t}(s) \cdot \nabla\phi(s) \tag{2.22}$$

Where

$$\phi(s) = \sum_{j=1}^{N} \Delta u_j[\log \parallel \mathbf{y}(s) - \mathbf{y}(\xi_{j+1}) \parallel - \log \parallel \mathbf{y}(s) - \mathbf{y}(\xi_j) \parallel] \tag{2.23}$$

This sum can be reorganised so that :

$$\phi(s) = \sum_{j=1}^{N+1} (\Delta u_{j-1} - \Delta u_j) \log \parallel \mathbf{y}(s) - \mathbf{y}(\xi_j) \parallel \tag{2.24}$$

Where $\Delta u_0 = 0$ and $\Delta u_{N+1} = 0$. Doing so, the computation of two different kernels is avoided. In order to simplify the multipole expansion and the local expansion, and following other authors like *Greengard and Rokhlin* (1987) ; *Carrier et al.* (1988), we will introduce a complex potential :

$$\phi(z) = \sum_{j=1}^{N+1} (\Delta u_{j-1} - \Delta u_j) \log(z - z_j) \tag{2.25}$$

Where the relationship between the real and the complex potential is given by :

$$\phi(\mathbf{x}) = \Re\mathrm{e}(\phi(z)) \tag{2.26}$$

$\Re$e and $\Im$m represent respectively the real part and the imaginary part of the expression in parenthesis. z and z_j are complex numbers that represent respectively the points $\mathbf{y}(s)$ and $\mathbf{y}(\xi_j)$. Likewise we can write an expression of the gradient in term of the complex potential which is :

$$\nabla\phi(\mathbf{x}) = \begin{bmatrix} \Re\mathrm{e}[\phi'(z)] \\ -\Im\mathrm{m}[\phi'(z)] \end{bmatrix} \tag{2.27}$$

FMM provides a fast way to compute the complex potential given in equation (2.25).

2.4.1 Adaptive quad-tree structure

This algorithm needs to create clusters of particles that are spatially close. For this purpose a quad-tree structure is used. Imagine that all the particles are in a square (Fig. 2.3, A). We will recursively subdivide this square into four new squares that are called the children (Fig. 2.3, B,C). We continue this process there remains less than a given number, N_{leaf}, of particles in a square. This naturally defines a quad-tree structure in which each square is called a cell. A square that contains less than N_{leaf} particles is called a leaf. The first cell is called the root. This structure can be divided into several levels, the root is at level 1. If a cell is at level l, then its children are at level $l+1$. Because the subdivision is done based on the number of particles in each square, and that we pruned the empty cells (Fig. 2.3, B,C,D), this quad-tree is called Adaptive.

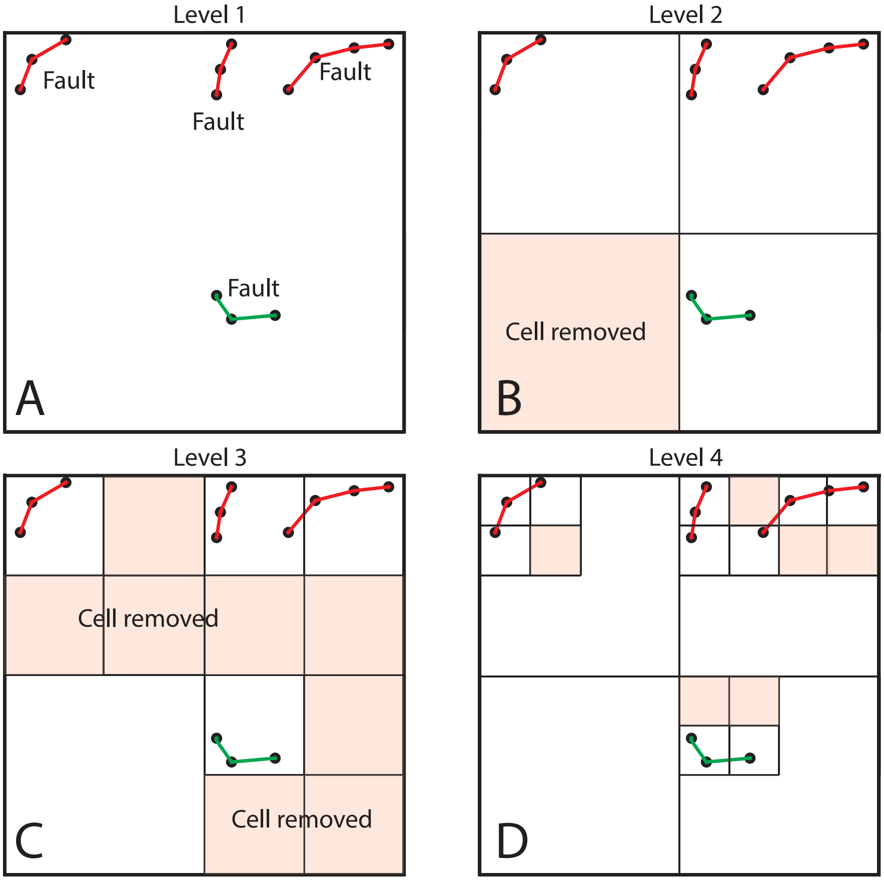

Figure 2.3 – The quad tree construction steps for the specific case where $N_{leaf} = 2$

We will introduce some definitions relative to the quadtree structure (see Fig. 2.4).

Near Neighbours Two cells are said to be near neighbours if they are at the same level and they share at least one boundary point.

Well separated Two cells are said to well separated if they are at the same level and they are not near neighbours.

Interaction list The interaction list of a cell consists into the children of the near neighbours of the cell's parent, which are well separated from the cell.

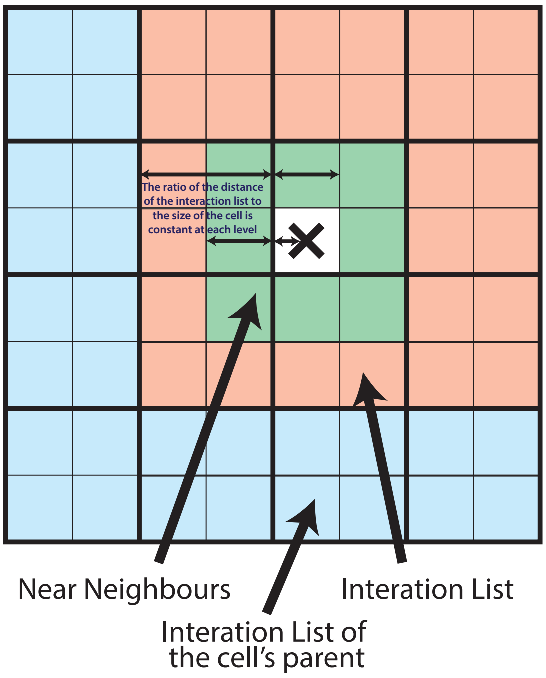

Figure 2.4 – Definition of the interaction list of a cell. The cross denotes the considered cell. Please note that at each level of refinement, the ratio of the size of the cell to the distance from the interaction list is constant. We will see later that this ratio controls the accuracy of the FMM.

2.4.2 Analytic approximation of the kernel

In this section, the kernel is developed assuming some conditions on the distance between points. For clarity, only mathematical developments are shown in this section. Basically, we are introducing two set of points which are respectively the multipole points M_n and the local expansion points L_m. These points are used to perform Taylor series expansion of the kernel. There are two theorems of expansion, one for the multipole expansion and one for local expansion, but also two other theorems to translate the centre of these expansions to new centres.

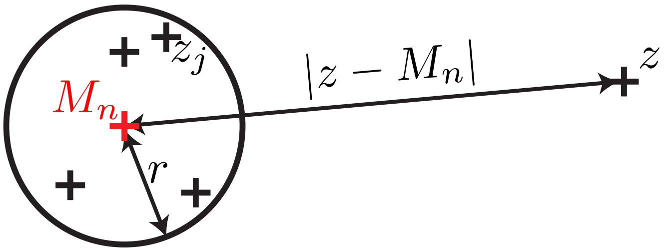

Figure 2.5 – Notations and assumptions for the multipole expansion

Multipole Expansion Imagine that we want to know the potential field due to a group of J point sources z_j far from the point z (Fig. 2.5). The first and exact method is to sum up all the contributions from individual source point using equation (2.25). However the far field potential of those points is smooth, hence we can develop the contribution of each point z_j on a multipole point M_n close to the group. Let choose one point M_n such that $\forall j, \| z_j - M_n \| < r$ and $\| \frac{r}{z - M_n} \| < 1$ (see Fig 2.5). Using a Taylor series expansion, equation (2.25) can then be written (*Greengard and Rokhlin*, 1987) :

$$\phi(z) = a_0 \log(z - M_n) + \sum_{k=1}^{\infty} \frac{a_k}{(z - M_n)^k} \tag{2.28}$$

Where

$$a_0 = \sum_{j=1}^{J} (\Delta u_{j-1} - \Delta u_j) \text{ and } a_k = \sum_{j=1}^{J} -\frac{(\Delta u_{j-1} - \Delta u_j)(z_j - M_n)^k}{k} \tag{2.29}$$

If we decide to truncate the infinite series at order p, we can get an error bound (*Greengard and Rokhlin*, 1987) :

$$\left|\phi(z) - a_0 \log(z - M_n) - \sum_{k=1}^{p} \frac{a_k}{(z - M_n)^k}\right| \leq \left(\frac{A}{p+1}\right)\left(\frac{1}{c-1}\right)\left(\frac{1}{c}\right)^p \tag{2.30}$$

Where

$$c = \left|\frac{z - M_n}{r}\right| \qquad A = \sum_{j=1}^{J} |(\Delta u_{j-1} - \Delta u_j)| \tag{2.31}$$

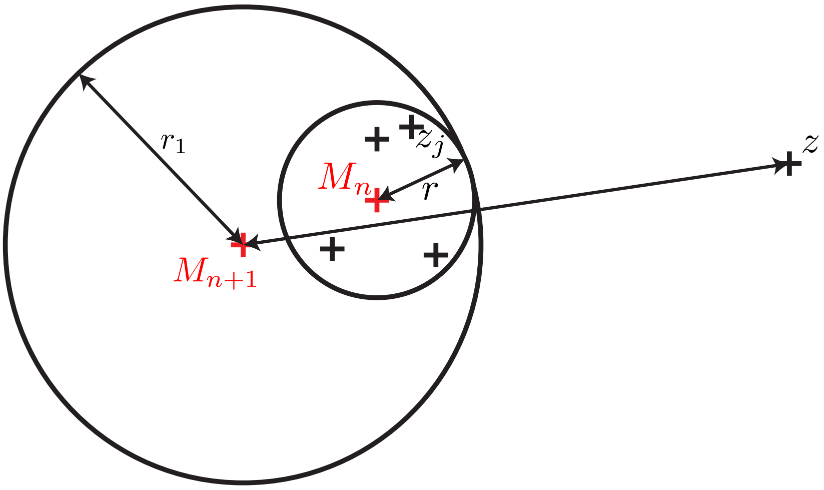

Figure 2.6 – Notations and assumptions for the translation of multipole expansions

Translation of Multipoles Suppose that we have a multipole expansion centered in M_n :

$$\phi(z) = a_0 \log(z - M_n) + \sum_{k=1}^{\infty} \frac{a_k}{(z - M_n)^k} \tag{2.32}$$

If the circle of radius r centered in M_n is included in the circle of radius r_1 centered in M_{n+1} (Fig. 2.6) and that the point z is outside of this circle, we can rewrite this multipole to be centered in M_{n+1} (*Greengard and Rokhlin*, 1987) :

$$\phi(z) = a_0 \log(z - M_{n+1}) + \sum_{l=1}^{\infty} \frac{b_l}{(z - M_{n+1})^l} \tag{2.33}$$

Where

$$b_l = -\frac{a_0}{l}(M_n - M_{n+1})^l + \sum_{k=1}^{l} a_k (M_n - M_{n+1})^{l-k} \binom{l-1}{k-1} \tag{2.34}$$

Moreover the error bound is :

$$\begin{gathered} \left| \phi(z) - a_0 \log(z - M_{n+1}) - \sum_{l=1}^{p} \frac{b_l}{(z - M_{n+1})^l} \right| < \\ \frac{A}{1 - \left| \frac{r_1}{z - M_{n+1}} \right|} \left| \frac{r_1}{z - M_{n+1}} \right|^{p+1} \end{gathered} \tag{2.35}$$

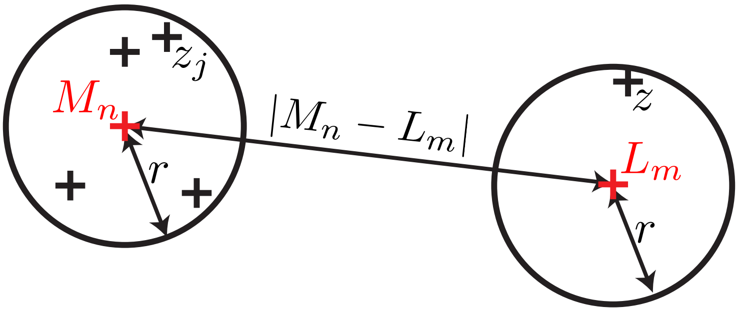

Figure 2.7 – Notations and assumptions for the local expansion

Conversion of multipole expansion into local expansion Now imagine that we calculate several multipole expansion of the points $M_n, n = 1..N$. $|M_n - L_m| > (c+1)R$ where $c > 1$

$$\phi(z) = a_0 \log(z - M_n) + \sum_{k=1}^{\infty} \frac{a_k}{(z - M_n)^k} \tag{2.36}$$

we can transform this expression into (*Greengard and Rokhlin*, 1987) :

$$\phi(z) = \sum_{l=0}^{\infty} b_l (z - L_m)^l \tag{2.37}$$

where

$$b_0 = a_0 \log(L_m - M_n) + \sum_{k=1}^{\infty} \frac{a_k}{(L_m - M_n)^k} \tag{2.38}$$

$$b_l = \frac{-a_0}{l} \frac{1}{(M_n - L_m)^l} + \frac{1}{(M_n - L_m)^l} \sum_{k=1}^{\infty} \frac{a_k}{(L_m - M_n)^k} \binom{l+k-1}{k-1} \tag{2.39}$$

$$\left| \phi(z) - \sum_{l=0}^{p} b_l (z - L_m)^l \right| < \frac{A(4e(p+c)(c+1)+c^2)}{c(c-1)} \left(\frac{1}{c}\right)^{p+1} \tag{2.40}$$

Where e is the base of the natural logarithm.

Translation of Local Expansions Imagine that a local expansion is centered on L_m. We have the following equation :

$$\phi(z) = \sum_{l=0}^{p} a_l (z - L_m)^l \tag{2.41}$$

This expression can be transformed into a local expansion centered about L_{m+1} using Horner's method (*Beatson and Greengard*, 1997) :

$$\phi(z) = \sum_{l=0}^{p} b_l (z - L_{m+1})^l \tag{2.42}$$

```
for j from 0 to p-1 do
    for k from p-j-1 to p-1 do
        $a_k := a_k - (L_m - L_{m+1}) a_{k+1}$
    end
end
```

Algorithm 1 : Horner's method. The coefficients a_k are then updated to b_k

Algorithm

Initialisation The first step of FMM is to build a tree based on a maximum number of points we want in the leafs of the tree. The accuracy of the solver will depend on the number of points.

Upward pass FMM start from the leafs and compute each coefficients of the multipole expansion (Fig.2.8, A). It is possible because the coefficients only depend on the particles that are in the cell : the multipole point, which is chosen to be the centre of the cell, the location of points in the cell, and their associated strength. Then the expansions at higher level are done by : 1) translating the multipole expansion of children to the centre of the parent cell (Fig.2.8, B, C), 2) adding up these multipole expansions (Fig.2.8, B, C).

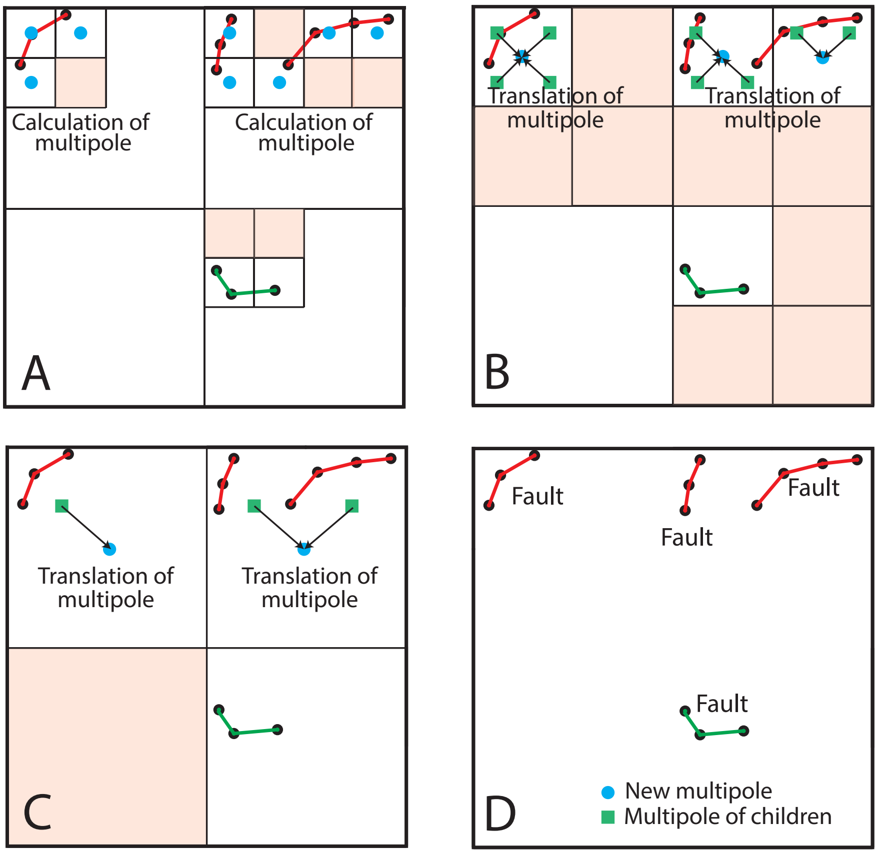

Figure 2.8 – Illustration of the upward pass of FMM

Downward pass The compute the local expansion, we start from the highest level, and compute the local expansion at the centre of the cell i of all cells in cell i's interaction list (Fig.2.9, C). Obviously, for the two-first levels, there is no cell in the interaction list (Fig.2.9, A, B). Then, this local expansion is shifted to the children's centre cells, and added to the local expansion of the children's interaction list (Fig.2.9, D). This procedure is done recursively until the cell has no children (it is a leaf cell).

Direct calculation Finally the interaction of near neighbours are computed directly.

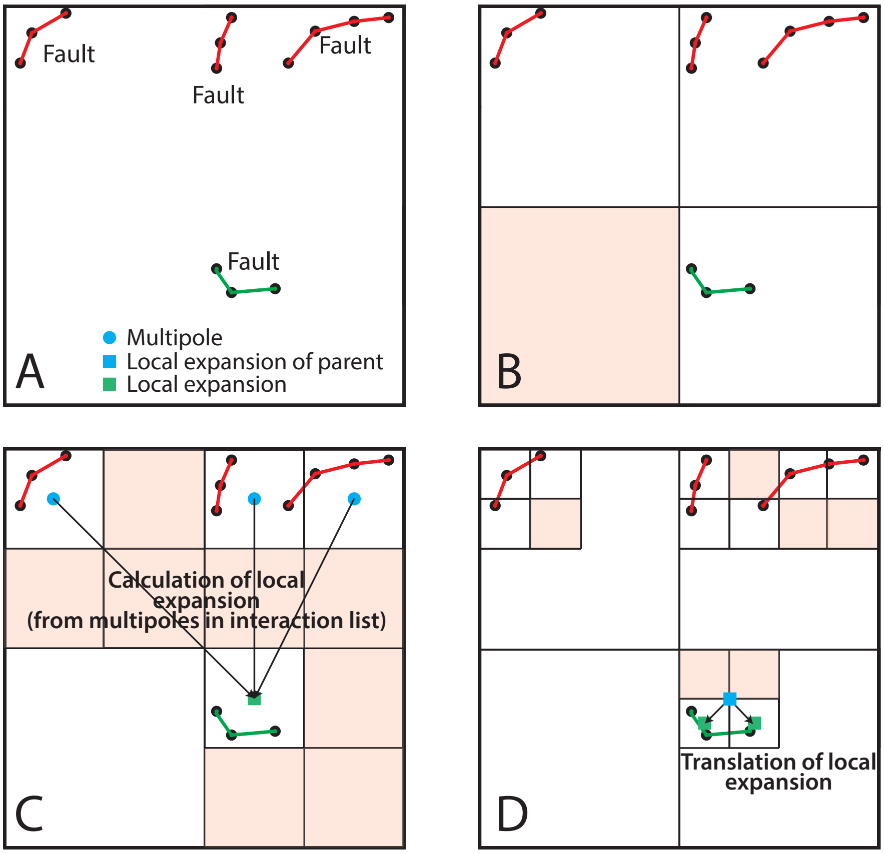

Figure 2.9 – Illustration of the downward pass of FMM

Limitation and Mode II kernels

The limitation of FMM is that it requires the development of a new algorithm for each different type of kernel. For mode III we showed that the kernel has the same expression as for the gravitational kernel. Doing so, we were able to use a preexisting FMM code from Prof. Greengard to compute the shear stress on the fault. However the kernels in mode II are more complex, because the Green's functions do not only depend on the distance between two points, hence the multipole expansion can be really tricky. To overcome this limitation of kernel dependency, new algorithms are emerging, sometimes called kernel-independent FMM. Hierarchical matrices are one of these kernel-independent Fast Multipole Method.

2.5 Hierarchical Matrices

2.5.1 Introduction

FMM shows a drastic diminution in the complexity of calculation to perform the matrix-vector product that appears in equation 2.25. However this analytical development of the kernels can be tricky. For the mode II, the development is not easy, and especially it has not been yet done for this particular problem. In order to be able to apply the same conceptual ideas as in FMM, for a general kernel, one can ask the following question : what is the form of the equation 2.25 after we performed the multipole expansion ? The assumption that we made were that the group of J source points was far enough the evaluated point. Starting from the general equation :

$$\phi(z_i) = \sum_{j=1}^{J} (\Delta u_{j-1} - \Delta u_j) K(z_i, z_j) \tag{2.43}$$

We were able to write :

$$\phi(z_i) = \sum_{j=1}^{J} \sum_{l=0}^{p} (\Delta u_{j-1} - \Delta u_j) K_l^1(z_i) K_l^2(z_j) \tag{2.44}$$

Where $K_l^1(z_i) = (z_i - M_n)^{-l}$ and $K_l^2(z_j) = \dfrac{(z_j - M_n)^l}{l}$. Kernels that can be written as a product of two functions, each of these functions depending on only one variable are called degenerated kernels. Degenerated kernels are very useful because they allow to simplify the calculation (*Beatson and Greengard*, 1997). Indeed, a direct calculation of the sum in equation (2.43) is of complexity $\mathcal{O}(J^2)$. However if we use equation (2.44), we can reorder the sum :

$$\phi(z_i) = \sum_{l=0}^{p} K_l^2(z_i) \sum_{j=1}^{J} (\Delta u_{j-1} - \Delta u_j) K_l^1(z_j) \tag{2.45}$$

If we calculate the second sum, defining new coefficients c_l

$$c_l = \sum_{j=1}^{J} (\Delta u_{j-1} - \Delta u_j) K_l^1(z_j) \tag{2.46}$$

This calculation requires Np operation. Then is remains to calculate the sum :

$$\phi(z_i) = \sum_{l=1}^{p} c_l K_l^2(z_i) \tag{2.47}$$

If we calculate this sum for all the value of z_i this sum is again of the order of Np. Thus the complexity is $\mathcal{O}(2Np)$. If p is small compared to $N/2$, this calculation becomes much more efficient. If we translate that into a matrix point of view, $K_{i,j} \leftrightarrow K(z_i, z_j)$, according to equations (2.43) and (2.44), we should be able to write :

$$K_{i,j} = \sum_{l=0}^{p} K_{i,l}^2 K_{j,l}^1 \tag{2.48}$$

Now if we write $(K_{i,l}^2) = \mathbf{u}_l$ and $(K_{j,l}^1) = \mathbf{v}_l$ this equation becomes :

$$(K_{i,j}) = \sum_{l=0}^{p} \mathbf{u}_l \mathbf{v}_l^T \tag{2.49}$$

This means that applying a multipole expansion to the kernel is equivalent to find a representation of the $(K_{i,j})$ as a sum of the product of the two vectors $\mathbf{v}_l$,$\mathbf{u}_l$. Such a representation can be actually obtained from rank factorisation. Such a rank factorisation is not unique and there exist different ways to obtain a rank factorisation. For example, the Singular Value Decomposition is a way to obtain a rank factorisation. H-matrix can thus be viewed as the algebraic analogue of FMM (*Ohtani et al.*, 2011).

Definition

In this section we recall some definitions that will be useful for the description of H-matrices.

Column rank, row rank, rank The *column rank* of a general matrix $K \in \mathbb{C}^{i \times j}$ is the maximum number of the linearly independent column vectors of this matrix. Likewise, the *row rank* is the maximum number of the linearly independent row vectors of this matrix (*Desiderio*, 2017). A fundamental result in linear algebra is that the column rank and row rank are always equal, we define this number to be the *rank* of the matrix.

Full-rank, rank deficient A matrix $K \in \mathbb{C}^{i \times j}$ is said to be *full-rank* when the rank of this matrix is equal to the minimum dimension of the matrix. On the contrary, if the rank of a matrix is less than the minimum dimension of the matrix, this matrix is said to be *rank deficient*.

Frobenius norm To measure the distance of an approximation of a matrix to the original matrix, a norm is needed. A natural norm on the algebra of matrices is the Frobenius norm which is defined for a matrix $A \in \mathbb{R}^{m,n}$ whose coefficient are $a_{i,j}$ by :

$$\|A\|_F = \sqrt{\sum_i^m \sum_j^n a_{i,j}^2} \tag{2.50}$$

Rank factorisation The rank factorisation of a matrix $A \in \mathbb{R}^{m,n}$ of rank k is a decomposition of the matrix A into the product of two matrices $C \in \mathbb{R}^{m,r}$ and $D \in \mathbb{R}^{r,n}$.

$$A = CD \tag{2.51}$$

This rank factorisation always exists for a matrix, but is not unique.

Low rank approximation For a given accuracy ϵ, and a given norm, we define the low rank approximation of a matrix $A \in \mathbb{R}^{m,n}$ to be the minimum rank k of the matrix $A_k \in \mathbb{R}^{m,n}$ such that

$$\|A - A_k\| \leq \epsilon \|A\| \tag{2.52}$$

Singular value decomposition The Singular Value Decomposition (*Desiderio*, 2017) (SVD) of a matrix $A \in \mathbb{R}^{m,n}$ is

$$A = \sum_{l=1}^{r} \mathbf{u}_l s_l \mathbf{v}_l^T = U \Sigma V^T \tag{2.53}$$

Where $\Sigma \in \mathbb{R}^{m,n}$ is a diagonal matrix, U and V are orthogonal matrices ($UU^T = I = VV^T$). $\mathbf{u}_l$ and $\mathbf{v}_l$ are respectively the column and row vector of U and V. $s_1 > s_1 > ... > s_k$ are the square roots of the eigenvalues of $A^T A$ organised from the biggest one to the lowest one. If $A \in \mathbb{R}^{m,n}$ is a matrix then $A_k \in \mathbb{R}^{m,n}$ is its truncated SVD at rank k. The Eckart-Young-Mirsky theorem states that this is the best low rank approximation that exists.

Layout

Like FMM, H-matrices require the following ingredients : 1) to separate the space into clusters, which is done through a binary tree, 2) A block partitioning of the kernel matrix 3) A simple manner to check whether a block can be correctly approximated by a lower rank matrix.

2.5.2 Construction of a binary tree

In order to organise the particles, H-matrices follow the same idea as FMM using a cluster tree. In the specific algorithm of H-matrix that we are using, the tree is binary. The initialisation is done by placing all the particles in a rectangle cell (Fig. 2.10, A). Then each cells are iteratively divide into two new cells which are called the children (Fig. 2.10, B, C, D, E, F). The recursion for a cell stops when the number of particles in that cell is less than N_{leaf} (Fig. 2.10, F).

2.5.3 Construction of the structure of the matrix

In the subdivision of space, cells containing particles where formed. To build the H matrix, we need to define non overlapping blocks of interacting particles. Blocks are formed recursively, by going through the binary tree. At each level of the binary tree, two cells ω and ν are picked. If one of this cells is a leaf of the cluster tree, the recursion stops. The recursion will also stop if these two cells forms a matrix block suitable for a low rank approximation. The last blocks formed in this recursion are called the leaf blocks. It does not mean that they are formed from the leaf of the cluster tree. To know if a matrix block formed of two cells is suitable for low rank approximation, an *admissibility condition* function is introduced (*Börm et al.*, 2003).

2.5.4 Admissibility condition

The admissibility condition is here to say if a block-cluster can be approximated by a lower rank matrix or if it needs further subdivision. The admissibility condition depends on a parameter η. It we note ω and ν two cells that

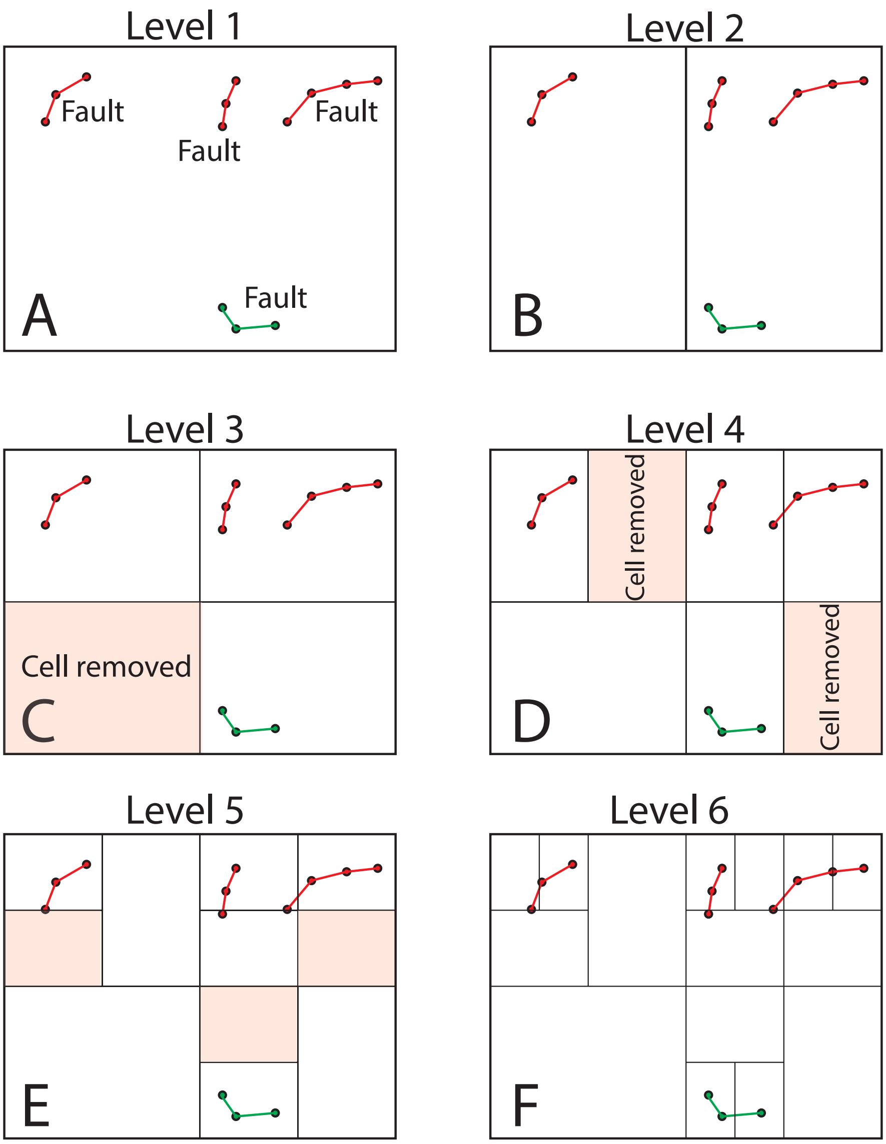

Figure 2.10 – The binary tree construction steps for the specific case where $N_{leaf} = 2$

are at the same level, then the admissibility condition is given by :

$$\text{Adm}(\omega, \nu) = \text{true} \Leftrightarrow \min\{\text{diam}(\omega), \text{diam}(\nu)\} \leq \eta \, \text{dist}(\omega, \nu) \qquad (2.54)$$

Where the diameter of the two cells are given by the length of their diagonal, and the distance between the two cells is the minimum distance between their boundaries (see Fig. 2.12). This is called admissibility condition

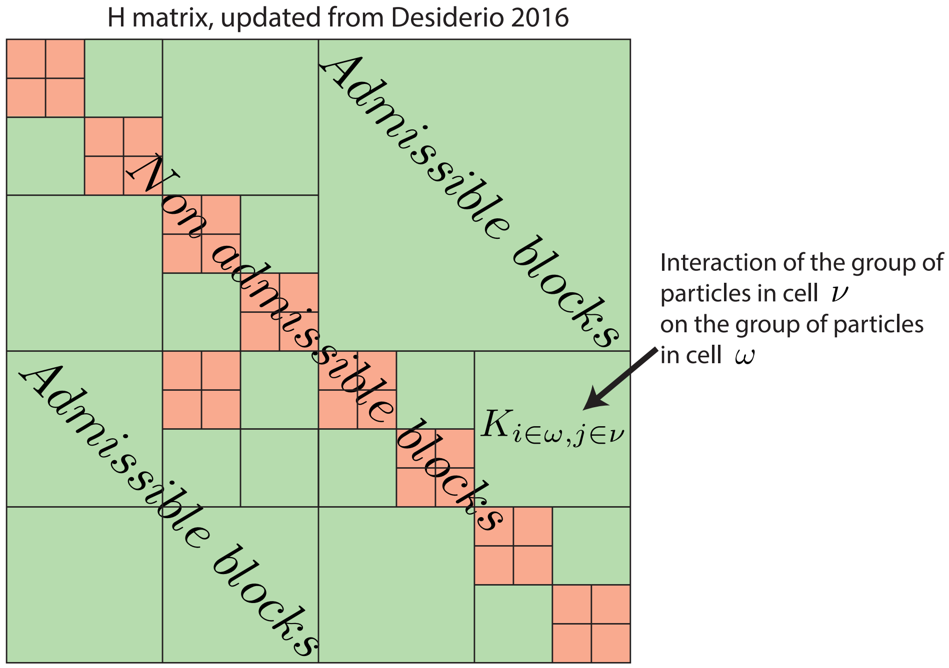

Figure 2.11 – One example of the final structure of an H-matrix

by bounding boxes (*Börm et al.*, 2003).

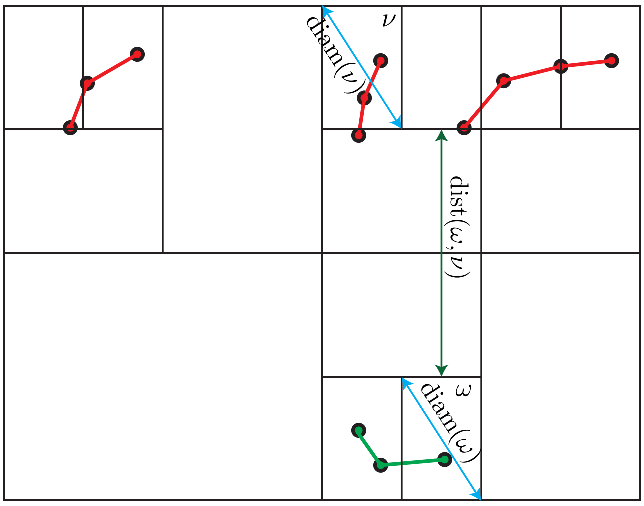

Figure 2.12 – Figure of the binary tree shown in *real space*. The definition of distance between two cells and diameter of a cell are given.

2.5.5 Low rank approximation

Singular Value Decomposition

The Eckartâ□□Youngâ□□Mirsky theorem says that the SVD provides the best low rank approximation to a matrix $A \in \mathbb{R}^{m,n}$ for the Frobenius norm. However SVD can not be used because this algorithm is really greedy in term of calculation time $\mathcal{O}(nm^2 + mn^2)$

Adaptive Cross Approximation

The Adaptive Cross Approximation (*Bebendorf and Rjasanow*, 2003) (ACA) provides a recursive procedure to decompose a matrix into a product of vectors. We will first illustrate the algorithm. Imagine a matrix $A \in \mathbb{R}^{3,3}$ with a being a non zero coefficient :

$$\underbrace{\begin{bmatrix} a & b & c \\ d & e & f \\ g & h & i \end{bmatrix}}_{A} \rightarrow \underbrace{\begin{bmatrix} a & b & c \\ d & e & f \\ g & h & i \end{bmatrix}}_{R_0=A} - \underbrace{\begin{bmatrix} 1 \\ d/a \\ g/a \end{bmatrix}}_{\mathbf{u}_1} \underbrace{\begin{bmatrix} a & b & c \end{bmatrix}}_{\mathbf{v}_1^T} = \underbrace{\begin{bmatrix} 0 & 0 & 0 \\ 0 & e-bd/a & f-cd/a \\ 0 & h-bh/a & i-ch/a \end{bmatrix}}_{R_1} \tag{2.55}$$

The aim is to minimise the matrix R_k (the residual matrix) by iteratively removing a product of two vectors. By considering this procedure and saving the vector $\mathbf{u}_k$ and $\mathbf{v}_k$, the matrix A is finally decomposed into a product of vectors :

$$A = \sum_{k=1}^{3} \mathbf{u}_k \mathbf{v}_k^T \tag{2.56}$$

The ACA algorithm uses this procedure to find a rank approximation of the matrix A. Instead of choosing the first coefficient a in the matrix, ACA looks for the maximum coefficient in the matrix, called the pivot, and removes the associated column and row. This procedure is applied iteratively to obtain a k-rank approximation A_k of the matrix A. The stop criteria is set for a given ϵ accuracy when :

$$\|A - A_k\| = \|R_k\| \leq \epsilon \|A\| \tag{2.57}$$

```
Data : a matrix $A$, a given accuracy $\epsilon_{ACA}$
Result : A low rank approximation of the matrix A
$S_0 := 0$;
$R_0 := A$;
while $\|A - S_k\| > \epsilon_{ACA}\|A\|$ do
    // Calculate the pivot
    $\gamma_k :=$ inverse of the maximum coefficient in $R_k$;
    $i :=$ row index of the maximum coefficient in $R_k$;
    $j :=$ column index of the maximum coefficient in $R_k$;
    // Calculate the two vectors
    $\mathbf{v}_{k+1} := \gamma_k (R_k)_{i,.}$;
    $\mathbf{u}_{k+1} := \gamma_k (R_k)_{.,j}$;
    // Update $R_k$ and $S_k$
    $R_{k+1} := R_K - \mathbf{u}_{k+1}\mathbf{v}_{k+1}^T$;
    $S_{k+1} := S_K + \mathbf{u}_{k+1}\mathbf{v}_{k+1}^T$;
end
```

Algorithm 2 : ACA

This algorithm can also be greedy, the number of operations needed is $\mathcal{O}(knm)$ for k-rank a matrix $A \in \mathbb{R}^{m,n}$ (*Bebendorf and Rjasanow*, 2003).

Partially pivoted ACA

Another way to avoid computing the whole matrix A is to choose the pivot differently. In the partially pivoted ACA, only one row and one column is computed at each time.

$$\underbrace{\begin{bmatrix} a & b & c \\ ? & ? & ? \\ ? & ? & ? \end{bmatrix}}_{\text{Initial matrix}} \rightarrow \begin{bmatrix} a & b & c \\ ? & e & ? \\ ? & h & ? \end{bmatrix} - \underbrace{\begin{bmatrix} 1 \\ e/b \\ h/b \end{bmatrix}}_{\mathbf{u}_1} \underbrace{\begin{bmatrix} a & b & c \end{bmatrix}}_{\mathbf{v}_1^T} = \underbrace{\begin{bmatrix} 0 & 0 & 0 \\ ? & 0 & ? \\ ? & 0 & ? \end{bmatrix}}_{R_1} \tag{2.58}$$

Here we started the with the first line. We find the maximum coefficient b in this line and this is used as a pivot. The associated column is computed. In this column, the maximum coefficient except the pivot is found. This is e, and the line associated to e will be used in the next recursion. The new matrix R_k is computed.

$$\underbrace{\begin{bmatrix}0 & 0 & 0\\ d^* & 0 & f^*\\ ? & 0 & ?\end{bmatrix}}_{R_1} \rightarrow \begin{bmatrix}0 & 0 & 0\\ d^* & 0 & f^*\\ ? & 0 & i^*\end{bmatrix} - \underbrace{\begin{bmatrix}0\\ 1\\ i^*/f^*\end{bmatrix}}_{\mathbf{u}_2} \underbrace{\begin{bmatrix}d^* & 0 & f^*\end{bmatrix}}_{\mathbf{v}_2^T} = \underbrace{\begin{bmatrix}0 & 0 & 0\\ 0 & 0 & 0\\ ? & 0 & 0\end{bmatrix}}_{R_2} \tag{2.59}$$

Where $d^* = d - ae/b$, $f^* = f - ce/b$ and $d^* = d - ae/b$. The amount of work required for this algorithm is of order $\mathcal{O}(k^2(m+n))$ (*Bebendorf and Rjasanow*, 2003). The complete algorithm can be find in *Bebendorf and Rjasanow* (2003). The error cannot be computed like in fully pivoted ACA, because it requires the knowledge of the full matrix. A way to overcome this issue is to stop the recursion when the newly calculated rank $k+1$, does not provide any gain in accuracy (*Bebendorf and Rjasanow*, 2003) :

$$\| \mathbf{u}_{k+1} \|_2 \| \mathbf{v}_{k+1} \|_2 \leq \epsilon_{ACA} \left\| \sum_{j=1}^{k+1} \mathbf{u}_j \mathbf{v}_j^T \right\|_F \tag{2.60}$$

Where $\| \sum_{j=1}^{k+1} \mathbf{u}_j \mathbf{v}_j^T \|_F$ can be computed recursively :

$$\left\| \sum_{j=1}^{k+1} \mathbf{u}_j \mathbf{v}_j^T \right\|_F^2 = \left\| \sum_{j=1}^{k} \mathbf{u}_j \mathbf{v}_j^T \right\|_F^2 + 2 \sum_{l=1}^{k} \mathbf{u}_{k+1}^T \mathbf{u}_l \mathbf{v}_l^T \mathbf{v}_{k+1} + \| \mathbf{u}_{k+1} \|_F^2 \| \mathbf{v}_{k+1} \|_F^2 \tag{2.61}$$

Recompression of the blocks

After performing a low rank approximation with ACA or partially pivoted ACA, a further compression can be obtain using SVD without any loss in accuracy (it is the optimal low rank approximation). This SVD does not cost a lot because it is done on a already compressed matrix.

2.5.6 Conclusion of H-matrix

Because of the degeneration of the kernel in many sub-blocks of the matrix, a matrix vector product can be done more efficiently.

2.6 Model of earthquake cycle

In order to set the model of earthquake cycle, we chose the compression negative sign convention.

2.6.1 Rate and State Friction

We will model the strength of our fault with a rate and state friction law :

$$\tau^f = -\sigma_n f = -\sigma_n \left[f_0 + a \log\left(\frac{V}{V_0}\right) + b \log\left(\frac{\theta V_0}{D_c}\right) \right] \tag{2.62}$$

With ageing state evolution law :

$$\dot{\theta} = 1 - \frac{\theta V}{D_c} \tag{2.63}$$

2.6.2 Loading

The loading will be done through global stress state rate.

$$\dot{\overline{\overline{\sigma}}} = \begin{bmatrix} \dot{\sigma}_{11} & \dot{\sigma}_{12} \\ \dot{\sigma}_{12} & \dot{\sigma}_{22} \end{bmatrix} \tag{2.64}$$

If we consider the particular point given by the position **y** on the fault, the tangential loading traction is then given by

$$\tau_t^{load}(\mathbf{y}) = \mathbf{t}(\mathbf{y}) \cdot \overline{\overline{\sigma}} \cdot \mathbf{n}(\mathbf{y}) \tag{2.65}$$

The same manner we can defined the normal loading traction :

$$\tau_n^{load}(\mathbf{y}) = \mathbf{n}(\mathbf{y}) \cdot \overline{\overline{\sigma}} \cdot \mathbf{n}(\mathbf{y}) \tag{2.66}$$

2.6.3 Radiation damping term

The radiation damping term was first introduced by *Rice* (1993). It was later shown that this term is exactly accounting for the instantaneous shear stress drop of the fault due to sliding (*Cochard and Madariaga*, 1994) :

$$\tau^{rad}(s) = -\frac{\mu}{2c_s} V(s) \tag{2.67}$$

We use that term together with the static kernel to account for some dynamics in the system. Without this term, the slip on the fault during one event would be unbounded (*Rice*, 1993).

2.6.4 Governing equations for Quasi-Dynamic earthquake cycle models

Balance of forces requires the strength of the fault to be equal to the elastic shear traction (due to slip) plus the far-field loading traction plus radiation damping term. This is :

$$\tau^f(s) = \tau_t^{el}(s) + \tau^{load}(s) + \tau^{rad}(s) \tag{2.68}$$

If we differentiate this equation, it can be recast into a set of coupled ODEs. The slip acceleration is given by :

$$\dot{V} = \frac{\overbrace{\dot{\tau}^{load}}^{\text{shear loading}} + \overbrace{\int_{faults} K^t(s,\xi)\frac{\partial}{\partial \xi}V \mathrm{d}\xi}^{\text{shear traction change } \textbf{(H-Matrix)}} + \overbrace{\dot{\sigma}_n f}^{\text{normal stress variations}} + \overbrace{\sigma_n b \frac{\dot{\theta}}{\theta}}^{\text{state evolution}}}{\underbrace{\frac{\mu}{2c_s}}_{\text{radiation damping}} - \underbrace{\frac{a\sigma_n}{V}}_{\text{direct effect}}} \tag{2.69}$$

From this equation, it is easy to see that the denominator would go to zero and hence the acceleration would go to infinity if there were no radiation damping term. The normal stress rate due to loading and/or sliding (mode II) :

$$\dot{\sigma}_n = \underbrace{\int_{faults} K^n(s,\xi)\frac{\partial}{\partial \xi}V \mathrm{d}\xi}_{\text{normal traction change } \textbf{(H-Matrix)}} + \underbrace{\dot{\tau}_n^{load}}_{\text{normal loading}} \tag{2.70}$$

and the state evolution law :

$$\dot{\theta} = 1 - \frac{V\theta}{D_c} \tag{2.71}$$

This set of ODEs is then solved at each centre of element, using the adaptive time step ODE solver algorithm called Bulirsch-Stoer (*Bulirsch and Stoer*, 1966).

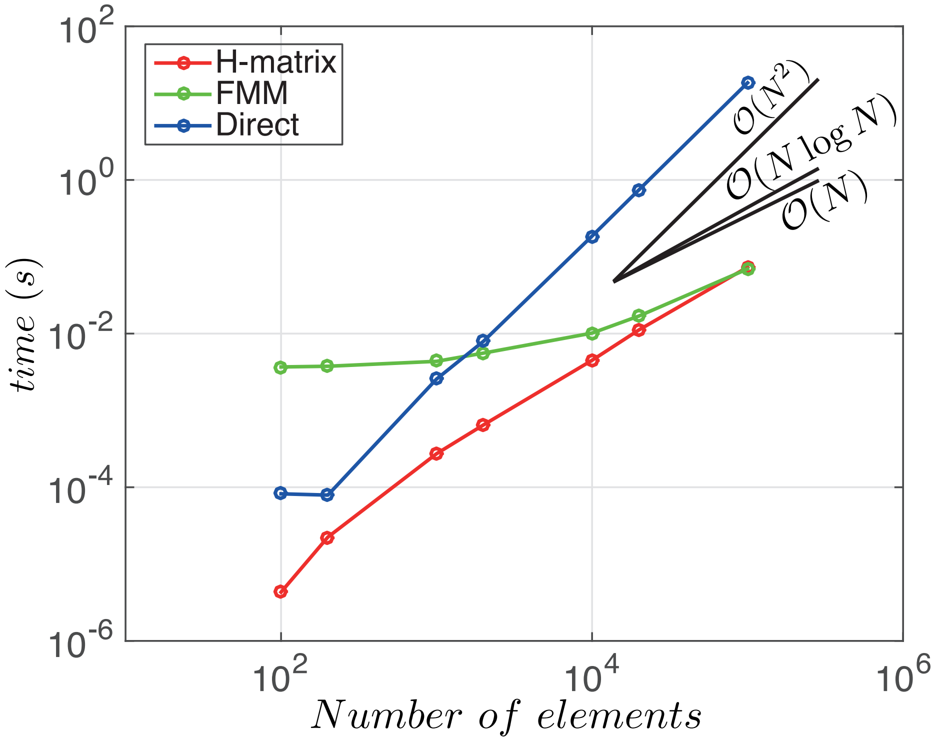

Figure 2.13 – Speed comparison of H-matrix, FMM, and the direct calculation.

2.7 Comparison of H-matrices and Fast Multipole Method

2.7.1 Speed of methods

To test the speed of the different methods, a single fault was used, a slip distribution was provided and we calculated the time to compute equation (2.15). The time used to compute the structure (trees, and block interaction), in both FMM and H-matrix was not taken into account. This is justified by the fact that this step is only done one time at the beginning of the simulation. Figure 2.13 shows that when the fault is discretised by 100 points to 100 000 points, H-matrix is the faster. As expected, the direct method has a complexity that grows as $\mathcal{O}(N^2)$. It is difficult to infer the complexity of H-matrix and FMM from this plot, but it seems that it is a bit more than $\mathcal{O}(N \log N)$. FMM seems to become more efficient than H-matrix for more than 10^5 particles.

2.7.2 Accuracy

The first method to test the accuracy was to see if the result from one time step would be accurate. To test that, a flat fault was assumed, with an imposed slip on it. For some particular slip on the fault, it is possible to calculate an analytical solution for the boundary integral equation (personal communication Robert Viesca, Fig 2.14) :

$$g(x) = \frac{1}{2\pi}\int_{-1}^{1}\frac{f(\xi)}{x-\xi}\mathrm{d}\xi \tag{2.72}$$

For the particular form of $f(\xi)$:

$$f(\xi) = -3\xi\sqrt{1-\xi^2} \tag{2.73}$$

Which corresponds to the following slip distribution :

$$\Delta u(\xi) = (1-\xi^2)^{\frac{3}{2}} \tag{2.74}$$

The analytical solution is given by :

$$g(x) = -\frac{3}{4}\begin{cases} 1-2\xi^2-2\xi\sqrt{\xi^2-1}, & \text{if } \xi < -1 \\ 1-2\xi^2, & \text{if } -1 \leq \xi \leq 1, \text{Inside the crack} \\ 1-2\xi^2+2\xi\sqrt{\xi^2-1}, & \text{if } \xi > 1 \end{cases} \tag{2.75}$$

Figure 2.15 shows the distance to the analytical solution of the direct BEM, FMM-BEM, and the H-matrix-BEM versus the number of points used to discretised the fault. This distance was measure with $\| \cdot \| = \sqrt{(\frac{1}{N}\sum_{i=1}^{N}(\cdot)^2)}$.The error of these three methods are perfectly matching for the aforementioned analytical solution. Another test of the accuracy was to see if the error is accumulated with time. At each time step in our simulations, the ODE-solver calls the BEM about 10 times, and the model runs for several 10000 of time steps. For this purpose, a simulation was run for FMM-BEM, H-matrix BEM, and direct BEM. For each of this method, and because for a flat fault mode II and mode III are equivalent, we also test the code for these two modes. Figure 2.16, gives the maximum velocity over time of each of the above types of simulation. On the last cycle, we checked if the earthquake was happening at the same time for each of this method. It appears that after 8 cycles

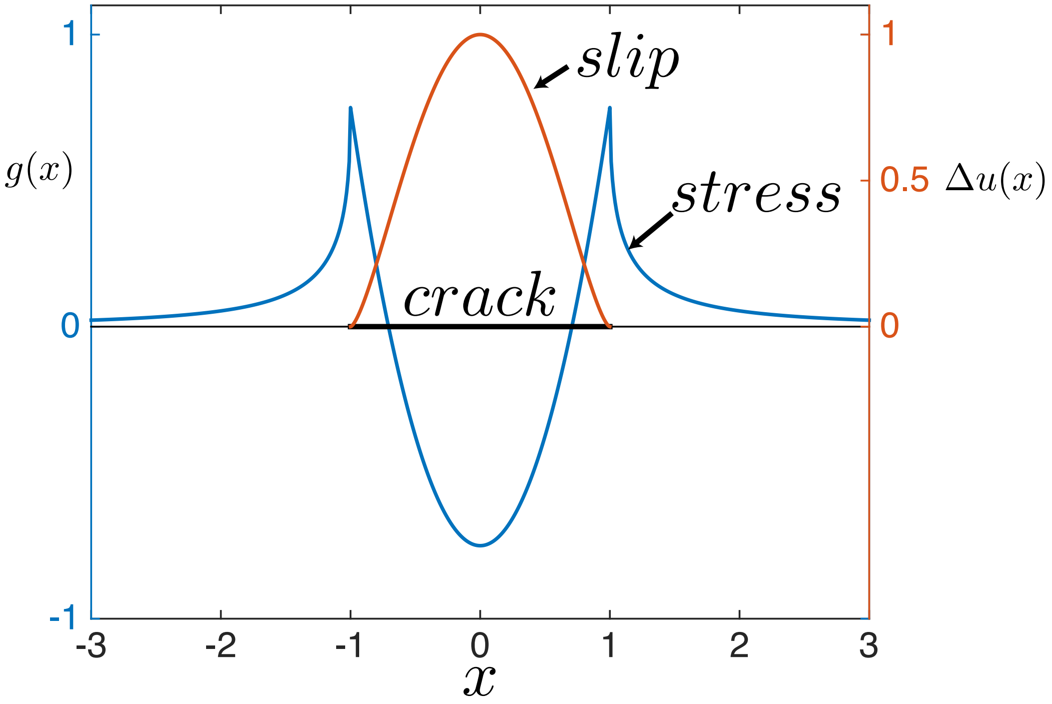

Figure 2.14 – Analytical solution

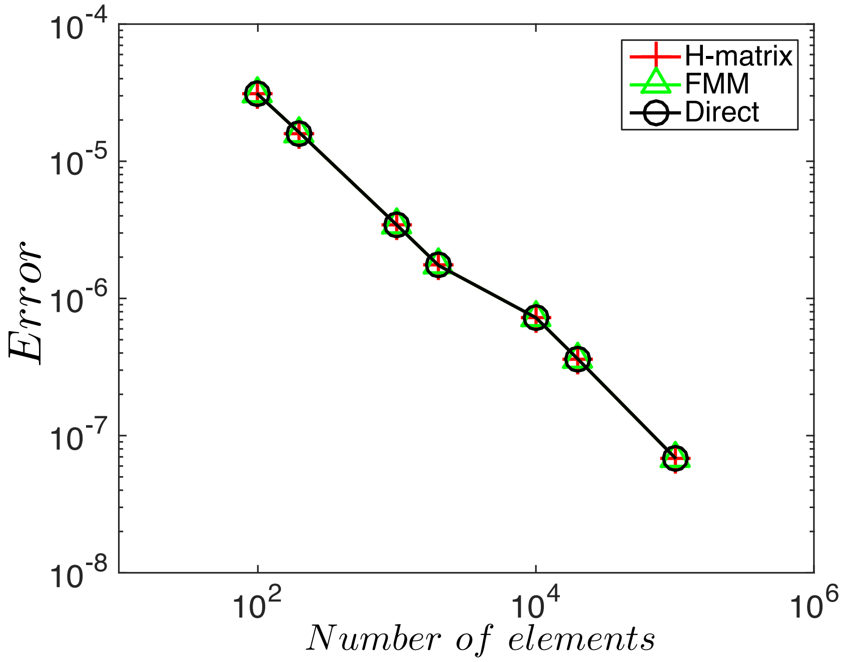

Figure 2.15 – Error calculation to the analytical solution (norm L_2). The three methods have the same accuracy.

over 160 years ($\sim 5 \times 10^9 s$) the offset between the earthquakes was only of the order of second. The two methods are in fact very accurate. The error in FMM is fully controlled because of the error bounds of each step. However in H-matrix the error is completely controlled only in the case where fully pivoted ACA, or SVD is used.

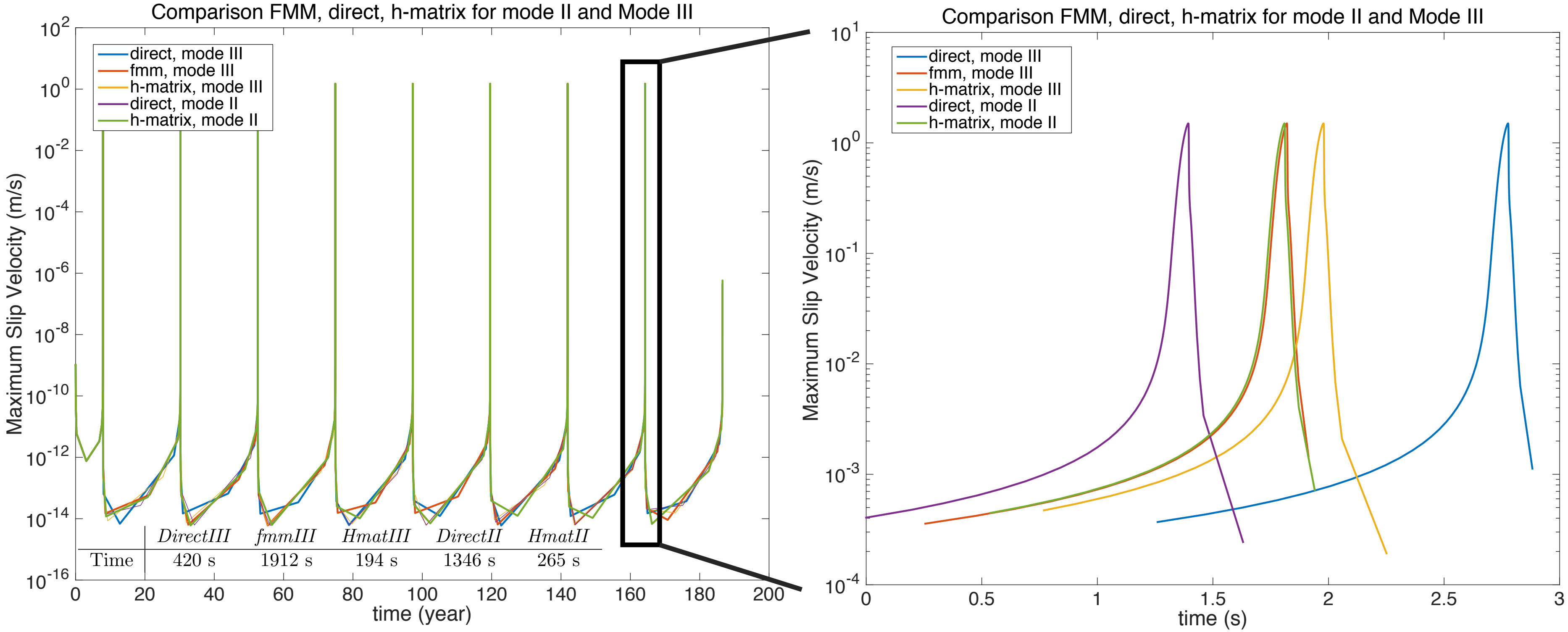

	$DirectIII$	$fmmIII$	$HmatIII$	$DirectII$	$HmatII$
Time	420 s	1912 s	194 s	1346 s	265 s

Figure 2.16 – Error calculation to the analytical solution (norm L_2). The three methods have the same accuracy. This simulation was done for a flat fault of length $L = 95$m, and $a/b = 0.8$. The other parameters can be found in table 3.2 .

2.8 Conclusion

We successfully developed a new paradigm were earthquake cycles are no longer restricted to single planar faults, but can be run on complex geometries with multiple faults. For general simulation of size $N \sim 10000$, the use of FMM or H-matrix, can increase the speed by a factor of about 100, which makes these methods extremely efficient for large simulations compared to the direct calculation. These two methods have very little drawbacks, because for FMM the accuracy is controlled at each step and for H matrix, it can be controlled if we use SVD or ACA to perform low rank approximation. The accuracy is guaranteed with these two methods. It is worth mentioning that in the elasto-static problem, the kernel does not depend on time and hence, the H-matrix needs to be calculated only one time. That means that all the low rank approximation has to be calculated only once, therefore it would be possible to use more elaborate low rank approximation like ACA or SVD. Because of the speed of these methods, a large set of parameters can be explored, for any fault geometry. We will take advantage of the speed gain in the following chapters, where we will use this model to explore a large set of parameters, also compute statistics on the outcome of results.

Chapitre 3

Overlapping faults in mode III

Avant-propos

Ce chapitre est une adaptation d'un article soumis à *Nature Geoscience*. Les résultats se concentrent majoritairement sur l'élasticité ”out-of-plane” (la direction de glissement est perpendiculaire au plan considéré), parce que les matrices hiérarchiques, qui permettent de faire aussi de l'élasticité ”in-plane” (ou la direction du glissement est dans le plan considéré), n'ont été implémentées dans FastCycles qu'en mai 2017. Dans ce chapitre, nous prenons avantage de la rapidité de *FastCycles* et du fait de pouvoir modéliser des systèmes complexes de failles pour explorer la relation entre deux failles dont une partie se superpose. Nous avons choisi cette configuration car cela est l'un des systèmes de failles les plus simples que l'on puisse considérer. La première partie présente les résultats attendus quand le cycle d'une unique faille est simulé. La deuxième partie présente les résultats quand deux failles dont une partie se superpose, interagissent entre elles. Le comportement du système de deux failles dépend majoritairement du ratio de la distance entre les failles par la longueur de nucléation D/L_{nuc}, de la proportion de superposition, du ratio de la longueur des failles par la longueur de nucléation L/L_{nuc} et du ratio de a/b. A partir de nos simulations, nous avons construit plusieurs diagrammes de phase qui permettent d'identifier les domaines où les comportements de ces deux failles diffèrent. Après une brève description de chacun de ces domaines, nous nous concentrons plus spécifiquement sur le domaine où des évènements de glissements lents apparaissent. Dans ce domaine particulier, nous avons montré que le moment des évènements de glissement lent et des tremblements de terre suivait une loi d'échelle qui peut se rapprocher de la loi d'échelle trouvée par *Ide et al.* (2007).

3.1 Introduction

This chapter is a broader discussion of an article entitled ”Fast and slow earthquakes emerge due to fault geometrical complexity” that was submitted to *Nature Geoscience*.

Since their discovery in the late nineties, Slow-Slip Events (SSE) have been widely observed along various subduction zones (Central Ecuador (*Vallee et al.*, 2013), Bungo Channel (*Hirose et al.*, 1999), Guerrero (*Lowry et al.*, 2001), Cascadia (*Dragert et al.*, 2001 ; *Rogers and Dragert*, 2003), Hikurangi (*Douglas et al.*, 2005), Northern Chile (*Ruiz et al.*, 2014) and others). The discovery of SSEs mainly came from the development and the installation of networks of permanent GPS stations around subduction zones. Although GPS is still nowadays the main SSE detection tool, new observations now allow for the detection of slow-slip, like networks of sea-bottom pressure gauge (*Ito et al.*, 2013 ; *Wallace et al.*, 2016) or via the migration of micro-seismicity, repeating earthquakes and tremors (*Igarashi et al.*, 2003 ; *Kato et al.*, 2012), thus increasing significantly the probability of their detection.

SSEs, like earthquakes, correspond to an accelerating slip front propagating along a fault. However, unlike earthquakes, SSEs do not radiate any detectable seismic waves and are hence sometimes nicknamed “silent events”. Until the discovery of SSEs, it was thought that only earthquakes release the accumulated strain energy along a fault. Since SSEs also contribute to this release of energy, they should play an important role in estimating the seismic hazard of subduction zones (*Obara and Kato*, 2016). In addition, SSEs exhibit very specific characteristics. Their propagation speed along the fault (about 0.5 km/h in Cascadia (*Dragert et al.*, 2004) to about 1 km/day in Mexico (*Franco et al.*, 2005)) contrasts with the rupture propagation speed of earthquakes (at about 3 km/s). The slip velocity of SSEs (from about 1mm/yr in the Bungo Channel, Japan to about 1 m/year in Cascadia) is around one or two orders of magnitude greater than plate convergence rates but orders of magnitude smaller than earthquakes slip rates (of the order of 1m/s)

(*Schwartz and Rokosky*, 2007).

Although the exact influence of SSEs in the seismic cycle is not yet fully understood, they seem closely related to earthquakes. Several seismic and geodetic observations suggest that SSEs may have happened just before and in regions overlapping with earthquakes. The 2011 $\mathrm{M_w}$ 9.0 Tohoku-Oki event and the 2014 $\mathrm{M_w}$ 8.1 Iquique event are two examples in subduction zones were a SSE apparently occurred just before the earthquake, within a region overlapping with the area where seismic slip nucleated (*Kato et al.*, 2012 ; *Brodsky and Lay*, 2014 ; *Ruiz et al.*, 2014 ; *Mavrommatis et al.*, 2015). More recently, geodetic evidence of a large SSE triggering an earthquake was pointed out in the Guerrero subduction zone (*Radiguet et al.*, 2016). There are also suggestions that SSEs may be triggered by earthquakes either by stress-waves and/or static stress transfer (*Itaba and Ando*, 2011 ; *Zigone et al.*, 2012 ; *Kato et al.*, 2014). On the other hand some SSEs occur without an accompanying large earthquake as in the Cascadia subduction zone, where SSEs occur periodically (*Rogers and Dragert*, 2003), or in the Hikurangi subduction zone (*Wallace et al.*, 2016). Yet, despite numerous observations and quantifications, the underlying physical mechanism driving SSEs remains largely unexplained. All SSEs have the same sense of slip as earthquakes, i.e. opposite to the plate convergence direction, and are accompanied by a positive stress drop which corresponds to a reduction in the accumulated strain energy. In the absence of external forcing mechanism, this necessitates SSEs to occur in a strength weakening region which is also prone to rupture as a fast dynamic event. These observations, put together, raise the first question. *What physical mechanism explains slow-slip and fast, dynamic earthquakes occurring on similar sections of active faults under similar frictional boundary conditions ?*

Furthermore, earthquakes and SSEs seem to follow different scaling laws (*Ide et al.*, 2007). The seismic moment of earthquakes scales with the cube of their duration ($M \propto T^3$) whereas the corresponding moment of SSEs is proportional to their duration ($M \propto T$), raising the second question. *Is such different scaling a general feature of earthquakes and SSEs, highlighting different physical mechanisms ? Or, is the gap in between these scaling laws simply resulting from a lack of observation (Ide et al., 2008 ; Peng and Gomberg, 2010) ?* We address the above questions using physics-based numerical modeling of active faults governed by rate-and-state friction (*Dieterich*, 1978) and develop a unified framework that addresses all the observations about earthquakes and SSEs mentioned above.

SSEs were first discovered to emerge spontaneously from numerical models in the rate-and-state framework for the modelling of subduction zones (*Liu and Rice*, 2005, 2007). In this framework, fault areas with weakening properties will preferentially host seismic slip (i.e. earthquakes) while strengthening regions will host stable continuous creep or post-seismic slip. Numerical experiments and theoretical works have shown that the main physical control on the emergence of SSEs in models is how the characteristic length of a weakening patch compares to the specific nucleation length scale (*Ruina*, 1983 ; *Rice*, 1983 ; *Dieterich*, 1992 ; *Rubin and Ampuero*, 2005). If the length of a fault patch is large compared to the nucleation length scale, earthquakes have enough room to grow and become dynamic, so this fault patch will generate only dynamic, seismic events. If the length of the fault is small compared to this length scale, earthquakes can never grow large enough to become dynamic or no events will occur at all (i.e. permanent creep). It is therefore necessary, under this framework, to tune for the right fault length compared to the nucleation length scale to allow modelling of both slow and fast ruptures. Given the observed spatial size over which some SSEs propagate i.e. on the order of tens of kilometres, this would lead to unrealistically large nucleation sizes, preventing the occurrence of any earthquakes. A possible explanation for such large nucleation lengths could be the presence of high-pressure pore fluids released during metamorphic dehydration reactions. However it has been shown recently that regions of high fluid pressure and slow slip events do not necessarily overlap along all the subduction zones (*Saffer and Wallace*, 2015). One solution to overcome this issue is to appeal to other competing frictional mechanisms like dilatant-strengthening (*Segall and Rice*, 1995 ; *Rubin*, 2008 ; *Segall et al.*, 2010) with or without thermal-pressurization (*Segall and Bradley*, 2012b). Although we do not include these additional frictional mechanisms, we acknowledge that it would broaden the range over which we are able to observe slow-slip.

Our work here differs from the above line of reasoning as we do not impose any lateral variation in the rheological properties of the fault. Our aim is to introduce no a priori complexity in initial and boundary conditions and let the variety of modes of slip emerge spontaneously. As the above models suggest, a set of competing mechanisms are required for slow-slip and earthquakes to coexist. We introduce this competition by appealing to the well known fact that faults are rarely planar over length scales of tens of kilometres. In fact, fault segmentation and geometric complexity are visible at multiple scales (*Candela et al.*, 2012). This non-planarity of faults introduces a natural stress based interaction between faults that can encourage or inhibit slow-slip. There are several lines of evidence that hint at geometric complexity being a viable candidate to explain the various observed slip dynamics. Aseismic slip has been observed with earthquake swarms in the northern Appenines (Italy) along splay faults (*Gualandi et al.*, 2017). It has been seen around a step-over in Haiyuan fault (China) (*Jolivet et al.*, 2013), along the North Anatolian Fault (*Rousset et al.*, 2016 ; *Bilham et al.*, 2016) or, in earlier publications, along the San Andreas Fault (*Murray and Segall*, 2005). SSE's have been observed in the very shallow part of subduction zones, where faults are invariably complex, as in Hikurangi (*Wallace et al.*, 2016), Nankai (*Araki et al.*, 2017) among others.

Friction on both faults is controlled by rate-and-state friction with ageing state evolution. Frictional resistance decreases with increasing slip rate and is spatially uniform i.e. the fault is rate-weakening. Loading is imposed using a constant rate of shear stress increase on the fault. We model elastic interactions using out-of-plane static stress interactions with radiation damping approximation (*Rice*, 1993). The computation of static stress interactions is accelerated using Fast Multipole Method (*Greengard and Rokhlin*, 1987 ; *Carrier et al.*, 1988).

To better understand the role of multi-fault interactions on slow and fast dynamics we explored the influence of the distance between faults, D, the length of the faults, L, and the ratio of the constitutive frictional parameters, a/b. For rate-weakening faults, a/b ranges between 0 and 1. Because of the importance of the nucleation length scale L_{nuc} in this problem, all geometrical parameter are non-dimensionalized by L_{nuc},

$$\begin{cases} L_{nuc} = 2 * 1.3774 * L_b & 0 \leq a/b < 0.3781 \\ L_{nuc} = 2 * \dfrac{L_b}{\pi(1-a/b)^2} & a/b \to 1 \end{cases} \tag{3.1}$$

where, a and b are rate-and-state constitutive friction parameters, D_c is the characteristic slip distance, μ is the shear modulus of the medium and σ_n the normal stress acting on the fault (*Rubin and Ampuero*, 2005 ; *Viesca*, 2016). This formulation provides good insights on the nucleation phase of earthquakes along a fault that is mildly rate-weakening ($a/b \rightarrow 1$) or extremely rate weakening ($a/b \rightarrow 0$).

3.2 Single planar fault

	$a/b < 0.4$	$a/b = 0.7$	$a/b = 0.8$	$a/b = 0.85$	$a/b = 0.9$	$a/b = 0.95$
L_{nuc}	83m	212m	477m	849m	1910m	7639m

Table 3.1 – Table of nucleation length scales for different value of a/b. The remaining parameters are listed in Table 3.2.

First we show two examples of single planar fault systems for high $a/b = 0.8$ and low $a/b = 0.2$. In that particular context, the fault behavior does not show any particular complexity. Here we chose long enough fault compared to the nucleation length scale that we only earthquakes (*Rubin*, 2008 ; *Veedu and Barbot*, 2016). Figure 3.1 shows in left panel the maximum slip velocity versus time, and in right panel the slip velocity evolution along the fault. Numbers are associated to events. On the right panel, for the first earthquake, the nucleation, and subsequent propagation along the fault are emphasized. Since the early quasi-dynamic simulation of *Rice* (1993), it is known that a well discretized fault with only constant friction parameters does not lead to any complexities. The fault is periodically rupturing into earthquakes and all the events are similar (Fig. 3.1 with $a/b = 0.8$ and Fig. 3.2 with $a/b = 0.2$), with the nucleation occurring at the same location, the velocity being similar and the duration of event being in the same order of magnitude. It is worth noting that for the $a/b = 0.2$ case, the nucleation length predicted by *Rubin and Ampuero* (2005) is perfectly matched (Fig. 3.2).

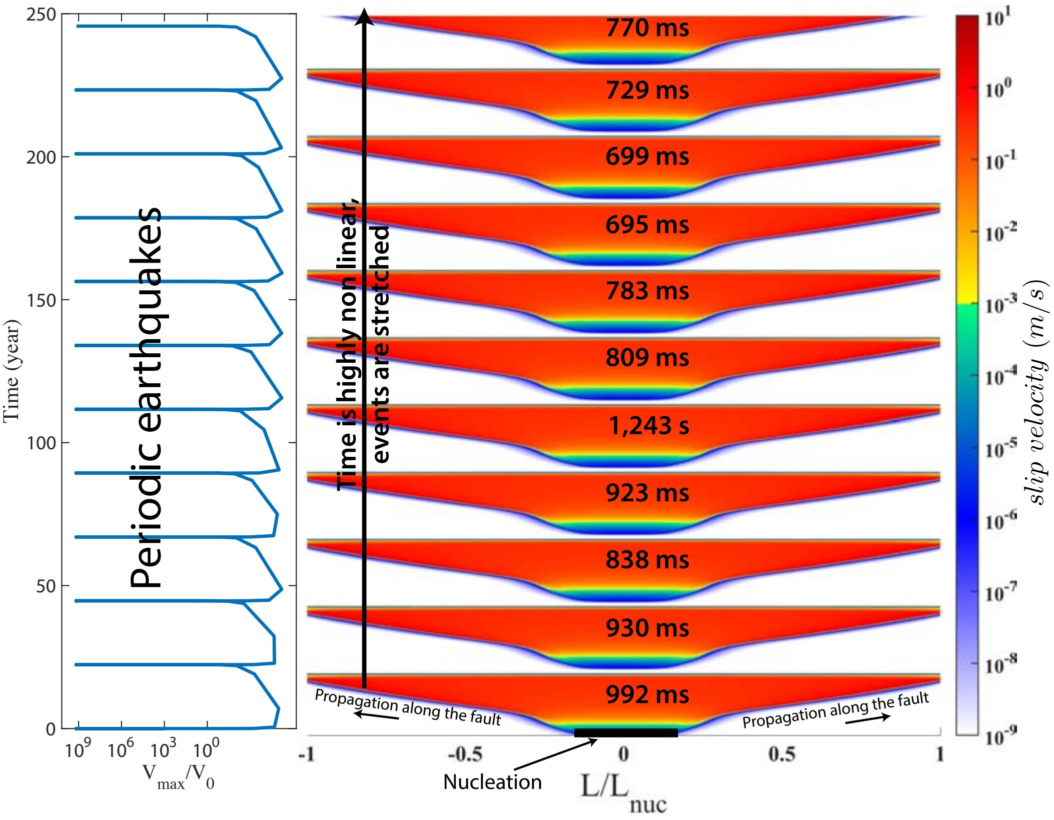

Figure 3.1 – Single fault simulation on a fault of length greater than the nucleation length ($L = 2L_{nuc}$). The frictional ratio is $a/b = 0.8$. All events look similar, they always nucleate at the centre of the fault and rupture the entire fault. They are completely periodic (left panel), and the duration of events, when slip velocity is higher than $V > 1mm/s$, is relatively constant.

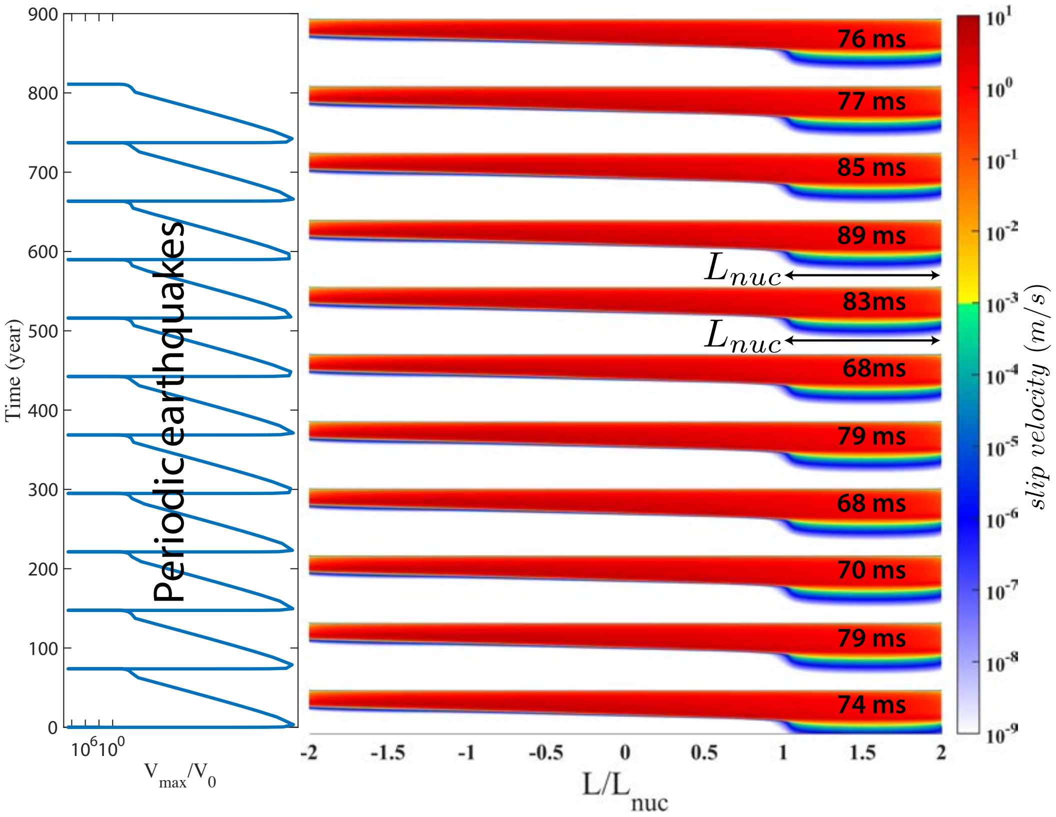

Figure 3.2 – Single fault simulation of length greater than the nucleation lengthscale ($L = 4L_{nuc}$). The frictional ratio is $a/b = 0.2$. All events look similar, they always nucleate at the right end of the fault and rupture the entire fault. They are completely periodic (left panel), and the duration of events, when slip velocity is higher than V > 1mm/s, is relatively constant.

3.3 Two overlapping faults

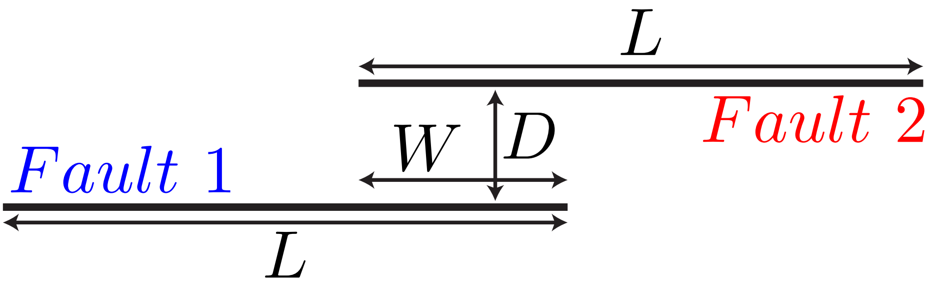

Figure 3.3 – Geometry of the system of two overlapping faults.

In the simplest “conceptual”model where the faults are geometrically complex, we consider two overlapping faults of the same length L that interact with each other (see geometry in Fig. 3.3 or in Fig. 3.9). This geometry was chosen to illustrate the effect of complex stress interaction between neighbouring faults and is in no way supposed to be interpreted as the only geometrical configuration of faults in a fault network. The choice of such geometry brings realistic perturbations in stress along the fault leading to the emergence of a wide variety of modes of slip. The novelty of this work is that slow-slip events can also emerge spontaneously on the same parts of the fault (whose lengths are larger than the nucleation length) that hosted dynamic earthquakes. Without the introduction of a second fault, and its associated stress perturbations, the fault behaves like a simple spring-slider system with weakening properties, with similar earthquakes happening periodically like it was shown in the previous section.

This section is mainly a presentation of the different kind of behaviors that happen in our simulation. For all these simulations, it is possible to separate different groups of behaviors, that mainly depend on the length of the considered fault to the nucleation lengthscale, and the ratio a/b of frictional parameters (see the phase diagram Fig 3.4). In each of the domain, one or two simulations (represented by a blue cross) are shown to illustrate the behavior.

The overlap will be at first considered to be half of the fault and the two faults will have the same size (Fig. 3.3). In this section, we explore

Name	symbol	Value
Reference friction coefficient	f_0	0.6
Reference velocity	V_0	10^{-9} m/s
Critical slip distance	D_c	0.1 mm
Rate and state parameter	b	0.01
Shear rate loading	$\dot{\tau}_t$	0.01 Pa/s
Normal stress	σ_n	100 MPa
Shear modulus	μ	30 GPa
Shear velocity	c_s	3000 m/s

Table 3.2 – Table of constant parameters among all the simulation shown in this section.

the influence in this particular setting of the length of the fault $L/L_{nuc} \in [0.1 \quad 0.5 \quad 1.0 \quad 2.0 \quad 3.0 \quad 4.0 \quad 5.0]$, the distance between the faults $D/L_{nuc} \in [0.1 \quad 0.5 \quad 1.0 \quad 2.0 \quad 3.0 \quad 4.0 \quad 5.0]$, and the friction parameters on the faults $a/b \in [0.05 \ 0.1 \ 0.2 \ 0.3 \ 0.35 \ 0.7 \ 0.8 \ 0.85 \ 0.9 \ 0.95]$ (490 simulations in total). Parameters that does not vary among different simulations can be found in table 3.2.

In this section, we will also explore the effect of the overlap distance.

3.3.1 Overlapping faults with constant overlap at close distance to each other

Damped zone

When the length of the fault is smaller than 10% of the nucleation lengthscale, the system is not able to produce any event. It is rapidly damped from the initial condition to a constant velocity of sliding. This behaviour is stationary, or constantly creeping. Figure 3.5 shows an example of such a behaviour where the maximum velocity in the system reaches a constant value. If a stationary solution exist in that system, the equation (2.69) can be simplified :

$$0 = \dot{\tau}^{load} + \int_{faults} K^t(s,\xi)\frac{\partial}{\partial \xi}V \mathrm{d}\xi \tag{3.2}$$

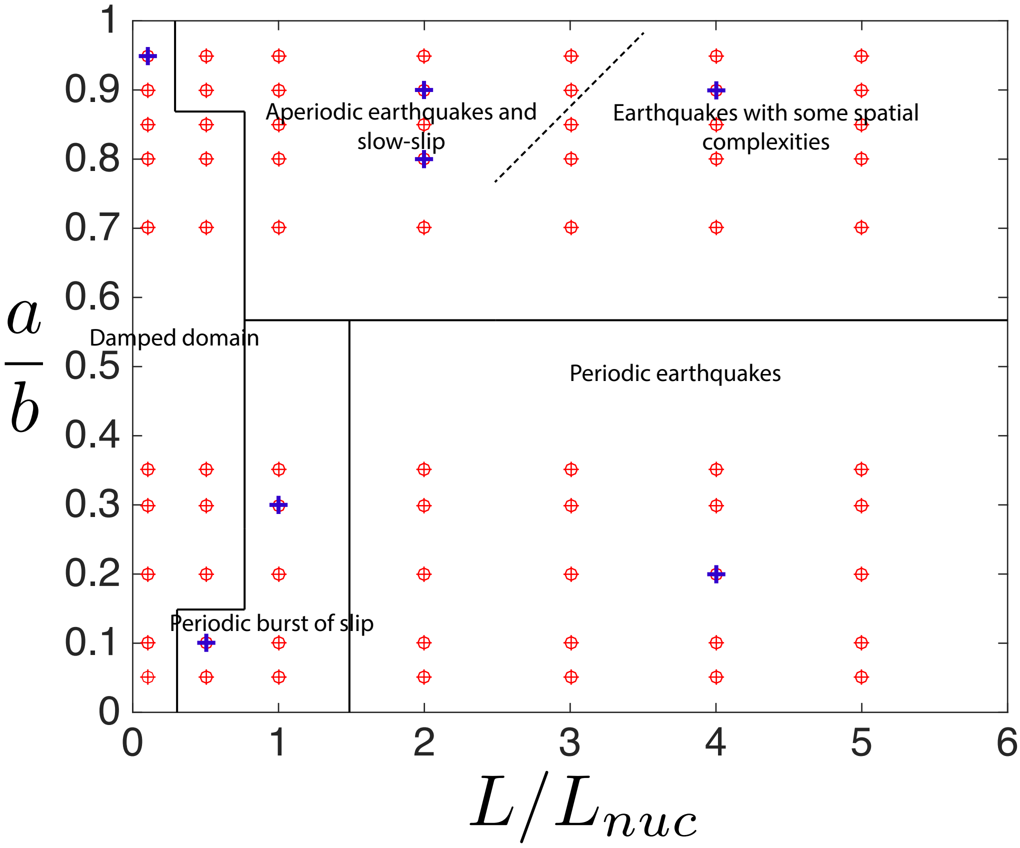

Figure 3.4 – Phase diagram showing the behaviour of two overlapping faults system. The distance between the fault is set to 10% of L_{nuc}. We can identify several domains, each of these showing different behaviour of the fault network. The blue cross are simulation that are shown in the following sections.

This equation is similar to a crack equation, where the slip on the fault gives a constant stress drop. It is possible to integrate in time this equation, it give :

$$0 = \dot{\tau}^{load} t + \int_{faults} K^t(s,\xi) \frac{\partial}{\partial \xi} \Delta u \mathrm{d}\xi + \tau_0^t \tag{3.3}$$

Where τ_0^t is an initial shear traction on the fault at time $t = 0s$. Finally this is a crack whose amplitude grows linearly with time. It is worth mentioning that a solution of this equation is not necessary known in the case of complex geometry and multiple faults. In the particular case of a single planar fault, the slip has an elliptical distribution over the entire fault, and the amplitude at each point of the fault is growing linearly with time.

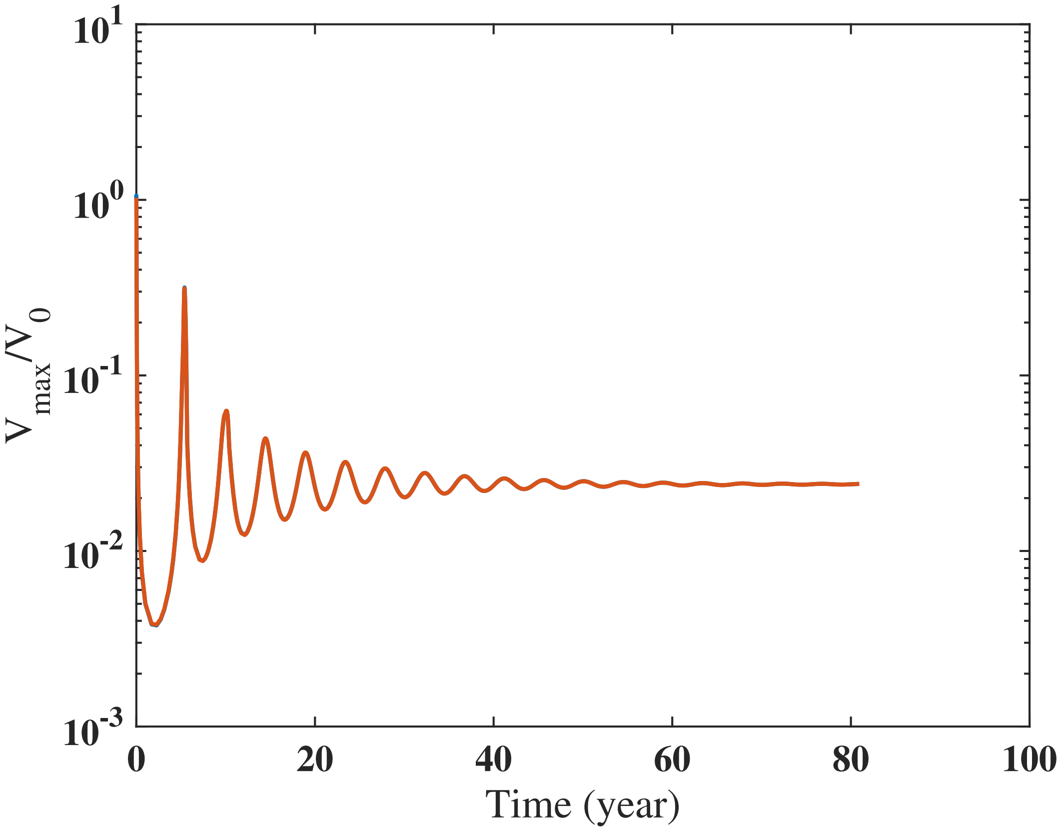

Figure 3.5 – Figure showing the maximum velocity on the fault when the system is in the damped domain. The length of the fault here is $L = 0.1 \times L_{nuc}$, the ratio $a/b = 0.95$ and the distance between the faults $D/L_{nuc} = 0.1$.

Sudden Burst of slip

Burst of slip are sudden acceleration of slip velocity that is affecting the entire fault at the same time without any apparent propagation of the rupture on the fault. This behaviour appears when a/b<0.4 and when the length of the fault is lower than, but close to the nucleation lengthscale. For extremely small ratio of $a/b < 0.1$, this phenomena seems to emerge even for faults whose length is half the nucleation lengthscale (Fig. 3.6). This behaviour was already observed in *Rubin and Ampuero* (2005), and it was called the *no-healing regime*. These authors also showed that this behaviour only happens for small ratio of $a/b < 0.3781$. Here we just confirmed what they were observing but in the quasi-dynamic approximation. As it has been already shown in figure 1.8, the nucleation lengthscale for small ratio $a/b < 0.4$ seems to be a robust estimation. In this domain, the interaction between the faults can bring some variability in the extend, and the location of the nucleation of earthquakes (Fig. 3.7), however the behaviour remains periodic.

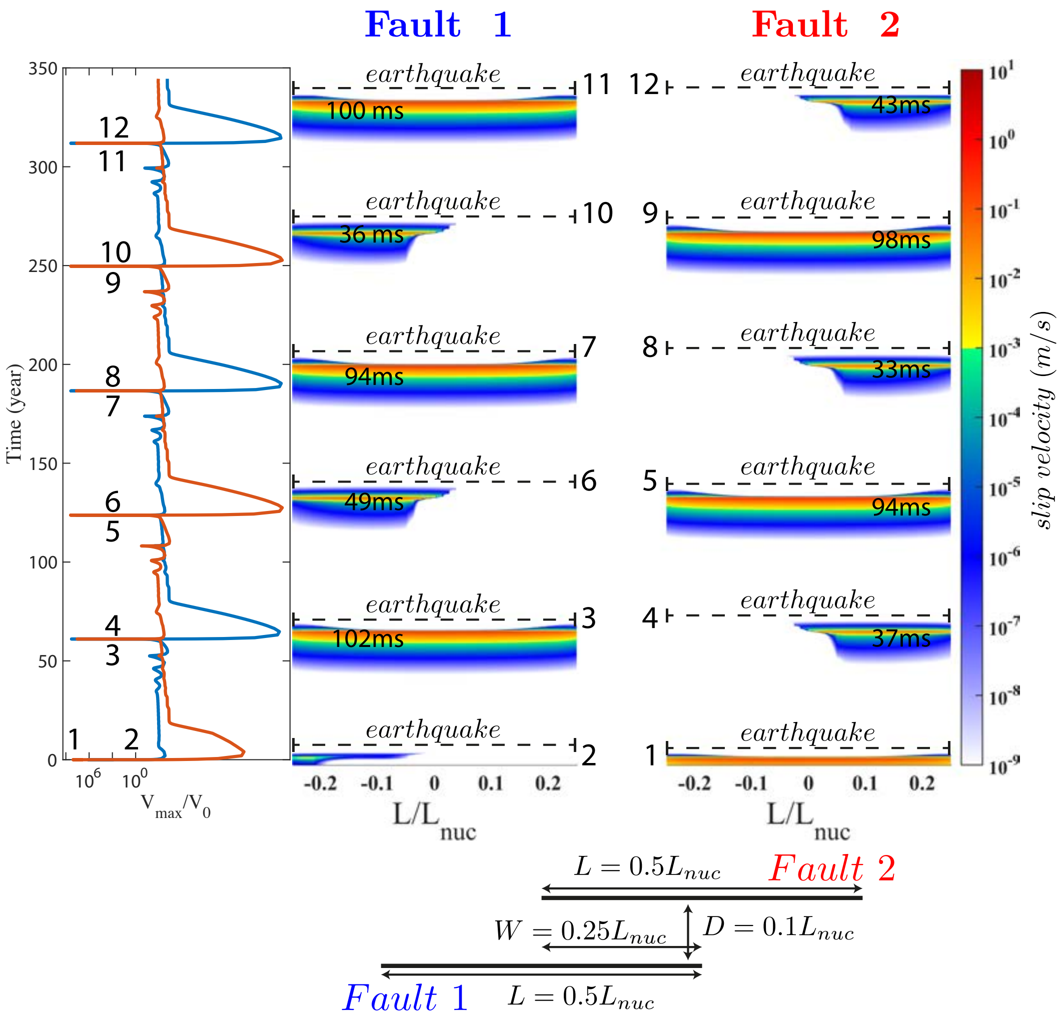

Figure 3.6 – Sudden burst of slip, there is no propagation of the rupture here. The whole fault is destabilized at the same time. This simulation is a particular case where the system is not damped although the length of the fault is half the nucleation lengthscale. This only happens when the ratio $a/b < 0.1$. Here the ratio is $a/b = 0.1$, the length of the fault is $L = 0.5L_{nuc}$ and the distance between the faults $D/L_{nuc} = 0.1$.

Slow and fast events, with spatiotemporal complexities

In this particular domain, it is possible to get all modes of slip, from extremely slow to fast events. We see regular earthquakes with a clear nuclea-

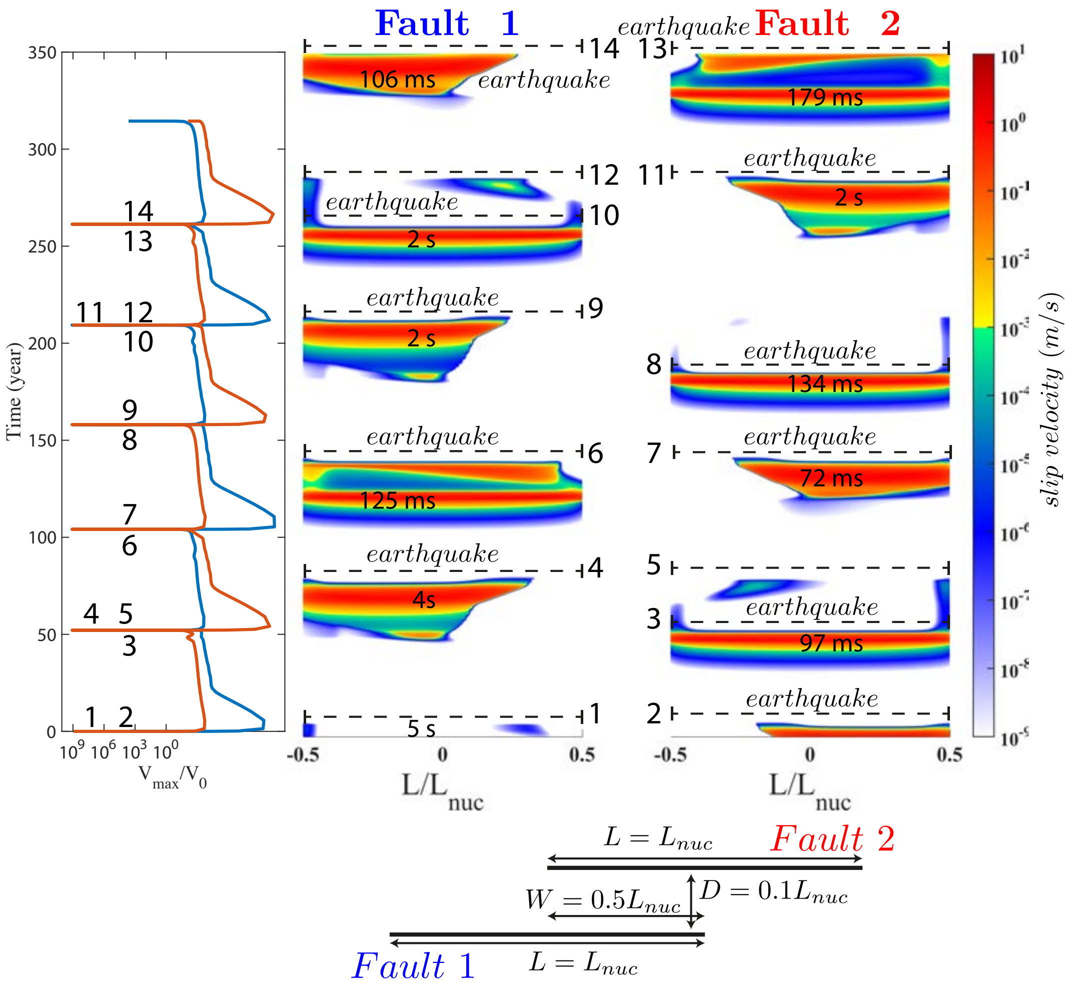

Figure 3.7 – Sudden burst of slip. The whole fault is destabilised at the same time. It seems that higher ratio of a/b shows more variability. It is possible to see partial rupture and the duration of events shows variability. Here the ratio is $a/b = 0.3$, the length of the fault is $L = 1L_{nuc}$ and the distance between the faults $D/L_{nuc} = 0.1$.

tion, dynamic and afterslip phases. These dynamic events happen without any evident periodicity. This is the domain where the behavior of the fault system is the most complex, we observe : seismic events slow-slip events, partial ruptures, afterslip, aperiodicity of the events. The figure 3.8 shows an example of such a complexity for $a/b = 0.8$. In this domain all events show a propagation along the fault, contrary to the *burst of slip domain*.

This complexity of behavior seems to increase with increasing ratio a/b (see the evolution for $a/b = 0.8$, Fig 3.8 and for $a/b = 0.9$, Fig. 3.9).

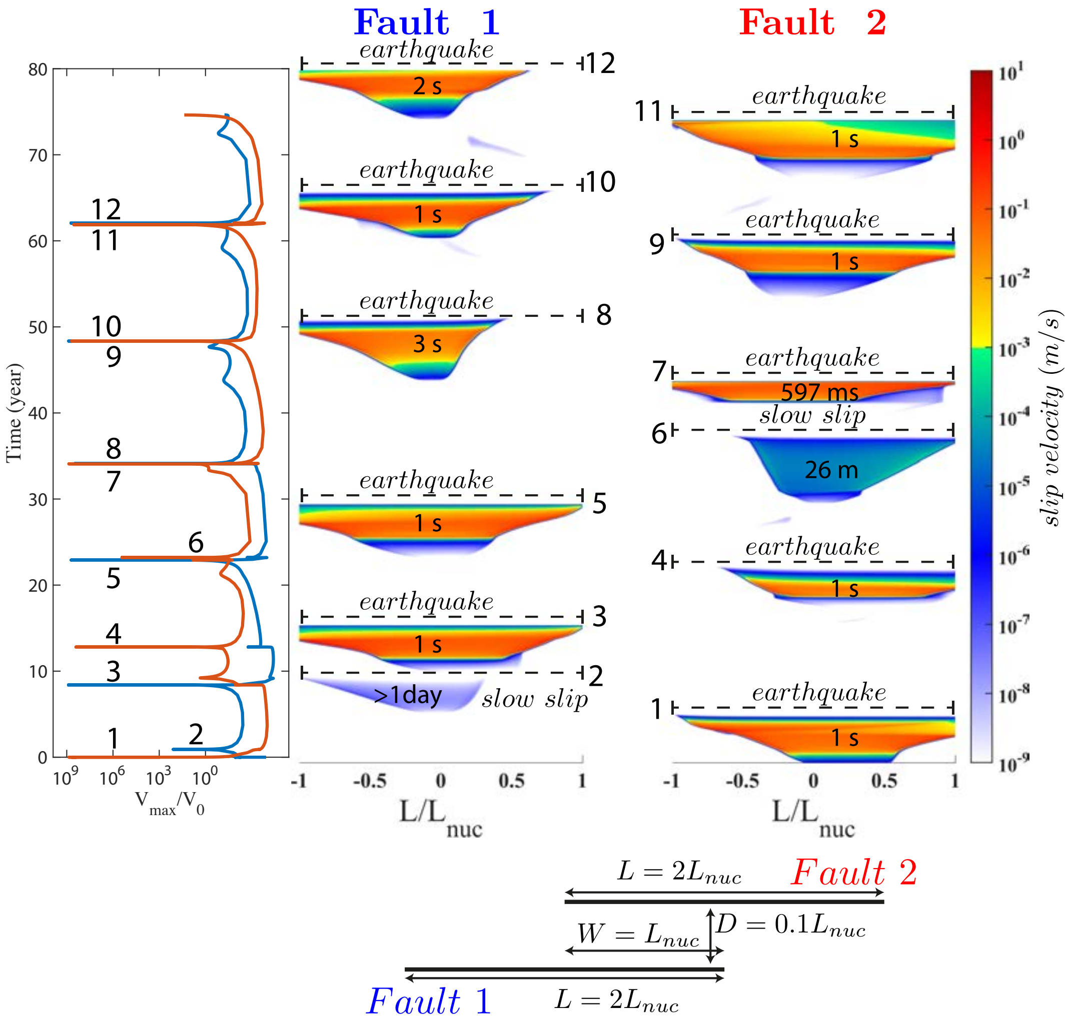

Figure 3.8 – Slow and fast events, with spatiotemporal complexities. We observe aperiodicity, with both slow and fast dynamics on the faults. Here the ratio is $a/b = 0.8$, the length of the fault is $L = 2L_{nuc}$ and the distance between the faults $D/L_{nuc} = 0.1$.

Periodic earthquakes

For extremely small ratio of a/b, and faults greater than the nucleation lengthscale, the two fault network only shows simultaneous earthquakes on both faults. These earthquakes are extremely periodic (see Fig. 3.10). In this domain the only complexity comes from the nucleation area and shape of the events.

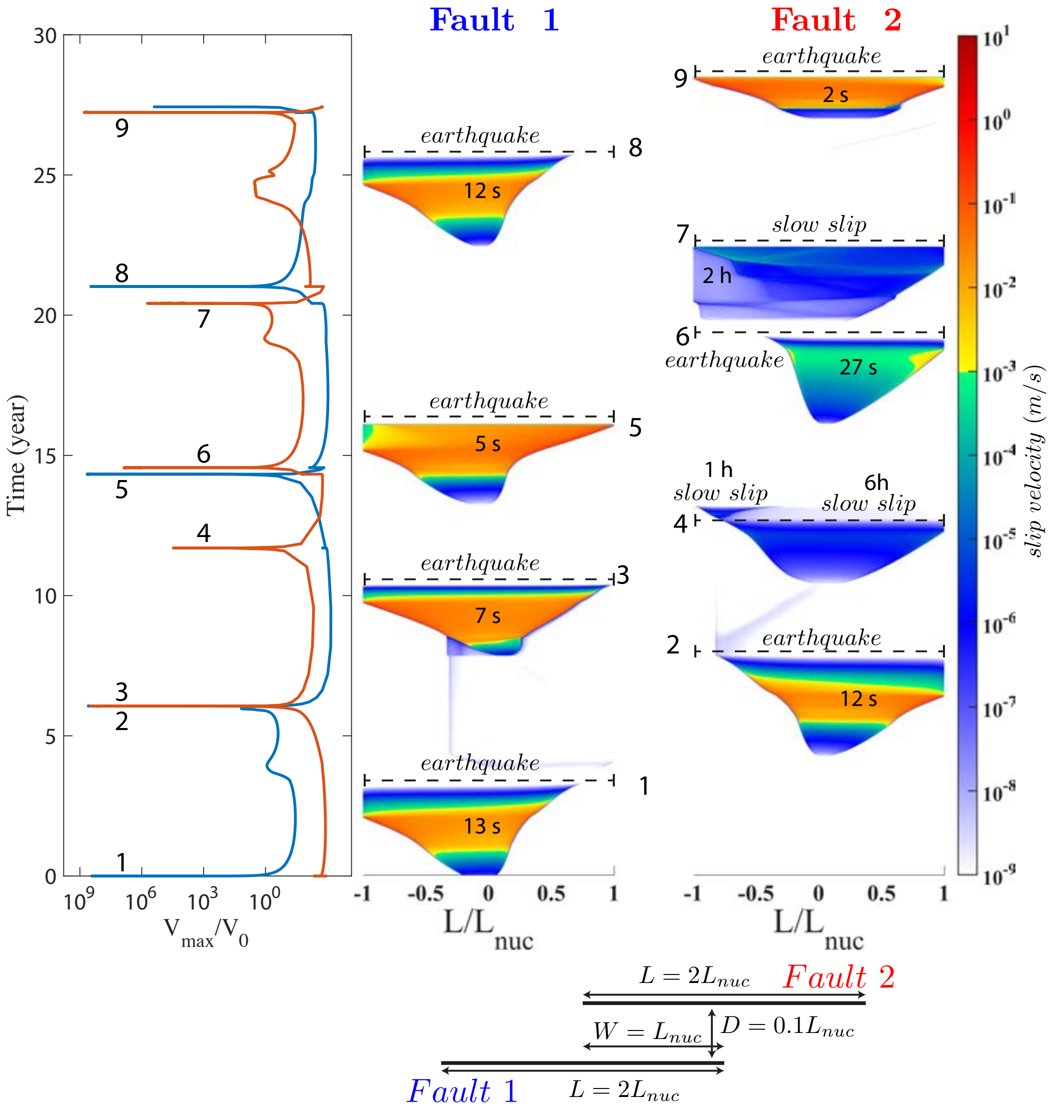

Figure 3.9 – Example of a calculation that gives rise to complex slip behaviour on faults. Here $L/L_{nuc} = 2$, $D/L_{nuc} = 0.1$ and $a/b = 0.9$. To avoid any artefact from initial conditions, the first 10 events of the simulation shown were removed. Left panel shows the maximum slip velocity for fault 1 (blue) and fault 2 (red). Right panel represents the space-time evolution of slip velocity on the faults. The highlighted duration of events corresponds to the time when the slip velocity exceeds 1μs for the first time to the time when it decelerates below 1μs. Bottom panel gives the geometry used for this example. Events 2,3 and 6 are slow-slip events. Events 1, 4, 5, 7 and 8 are earthquakes. Event 5 and 7 are small earthquakes that did not rupture the entire fault. Event 1 and 7 clearly show afterslip contrary to events 4 and 8.

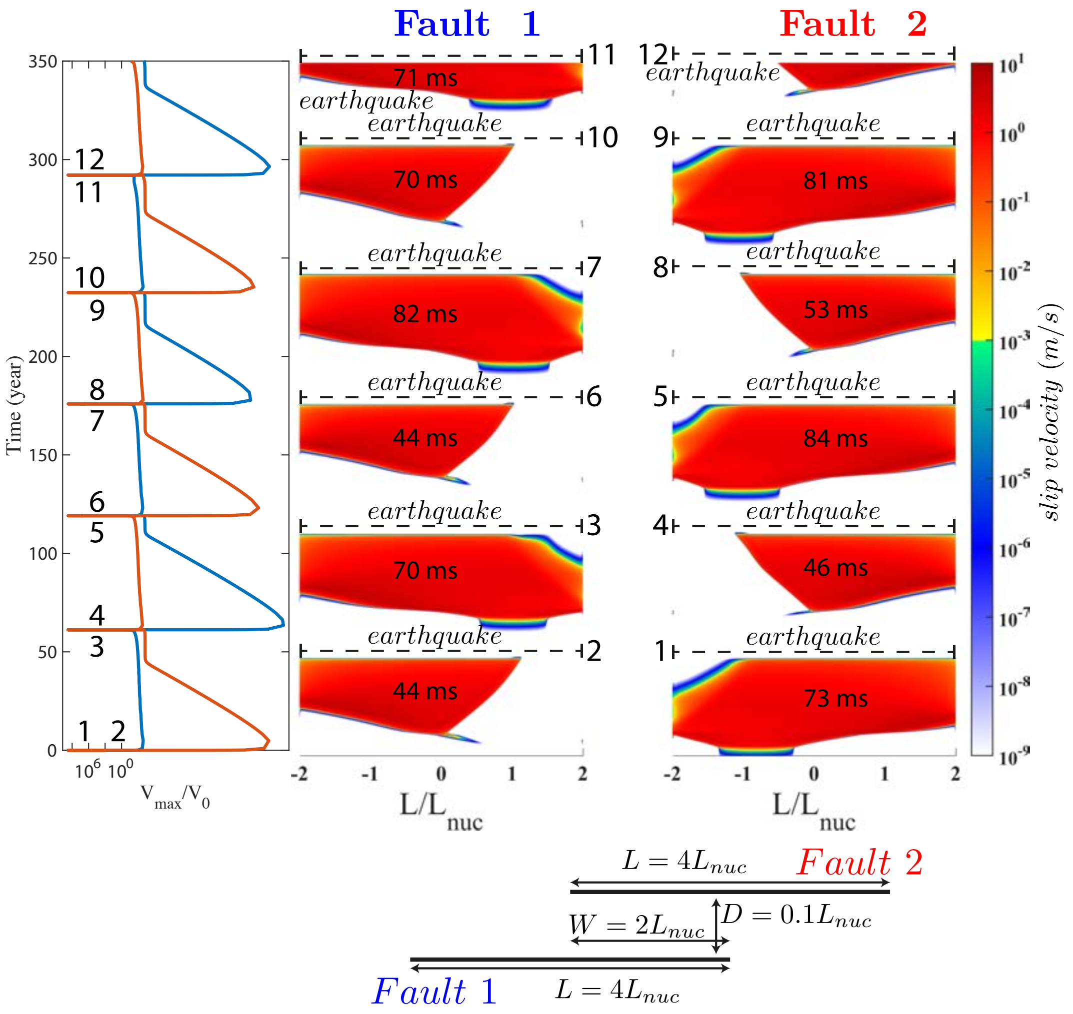

Figure 3.10 – Periodic earthquakes. Here the ratio is $a/b = 0.2$, the length of the fault is $L = 4L_{nuc}$ and the distance between the fault $D/L_{nuc} = 0.1$.

Earthquakes, with some spatial complexities

In this domain, the fault is too long to be able to host any slow events. It seems that this domains shows two different effects : with increasing ratio of a/b, the aperiodicity and complexity of events increase and the contrary effect holds for the increase in fault length. Actually, the distinction of this domain with the *”Slow and fast events, with spatiotemporal complexities”* domain is not obvious, and shows rather a continuum.

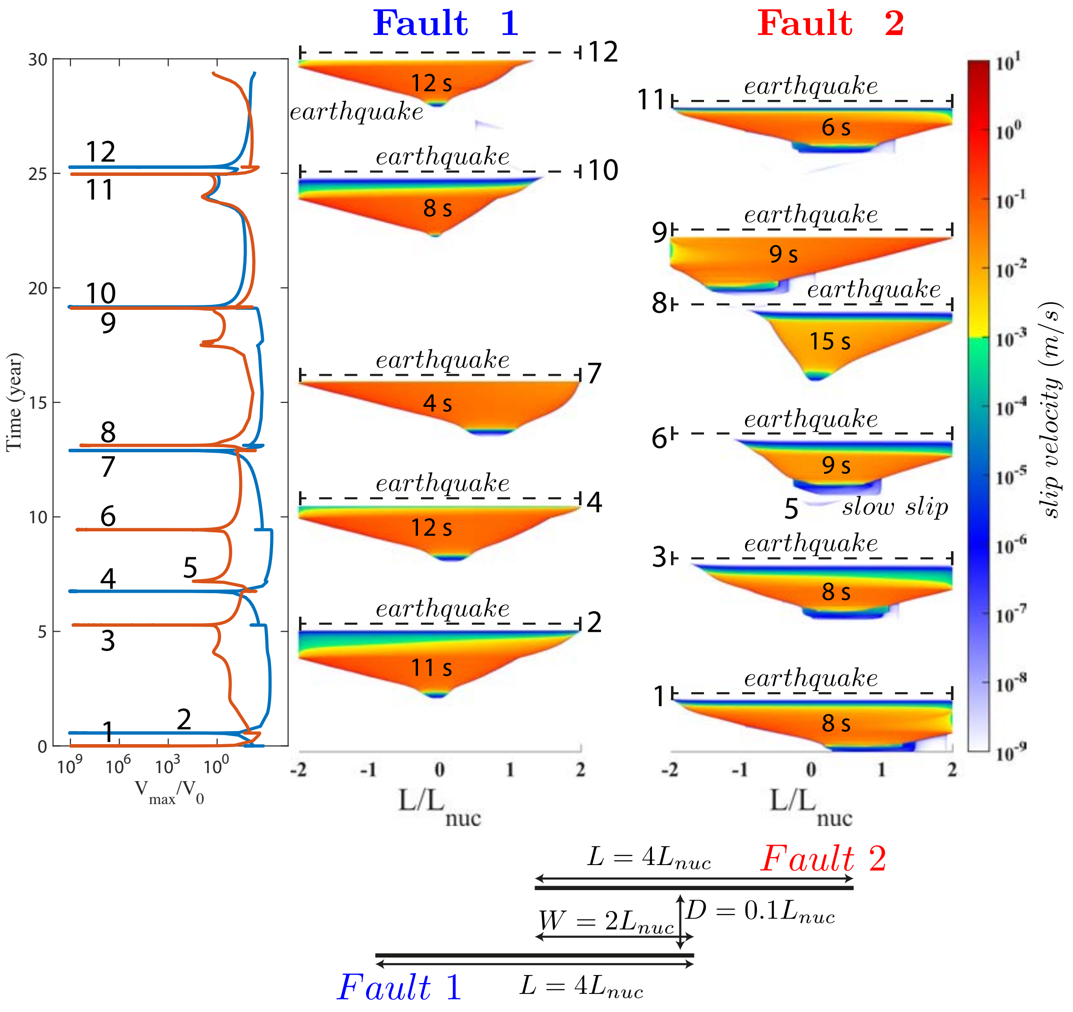

Figure 3.11 – Earthquakes, with some spatial complexities. Here the ratio is $a/b = 0.9$, the length of the fault is $L = 4L_{nuc}$ and the distance between the fault $D/L_{nuc} = 0.1$.

3.3.2 Overlapping faults with constant overlap at far distance to each other

In this section, the influence of distance between the two fault is explored. Basically, the effect of distance between the fault is the one that is expected : further the faults are from each other, less they interact and finally they look like a single faults behavior. To illustrate the effect of distance, the simulation where $a/b = 0.8$ and $L = 2L_{nuc}$ is used. The behavior of this simulation when the fault is alone (Fig. 3.1) and when two close overlapping faults are considered $D/L_{nuc} = 0.1$ (Fig. 3.8) have already been shown. In the following

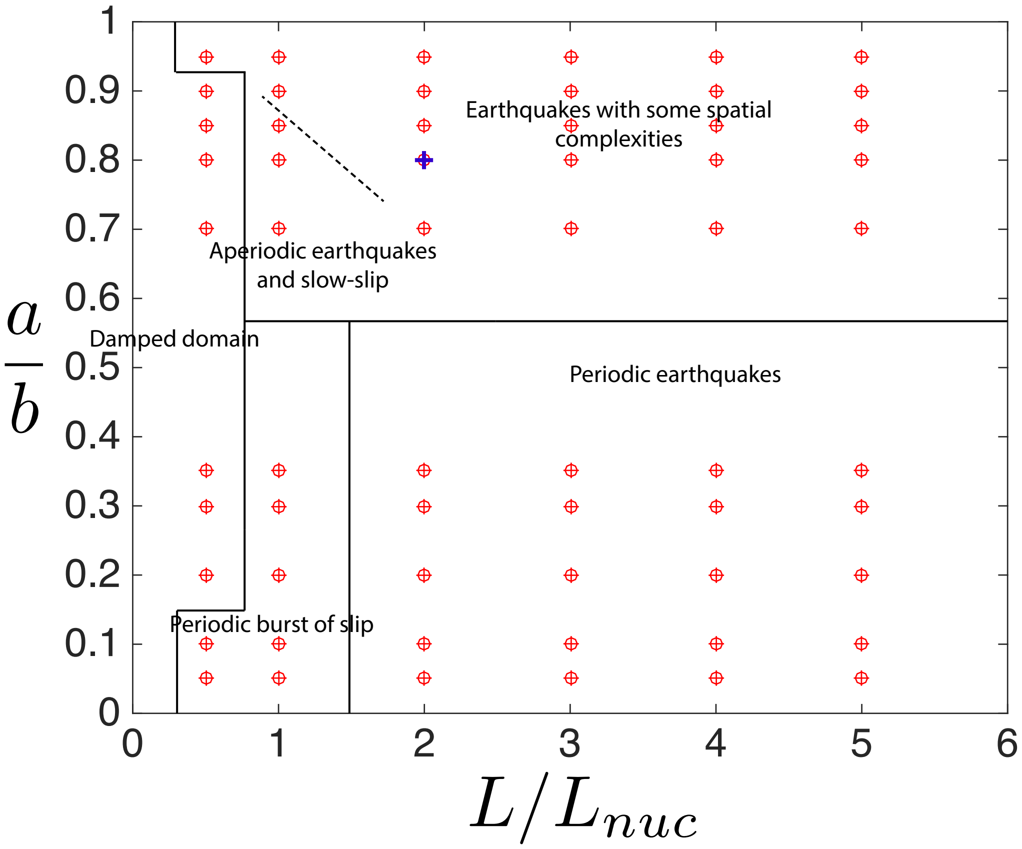

Figure 3.12 – Phase diagram showing the behaviour of two overlapping faults system. The distance between the fault is set to 50% of L_{nuc}. We can identify several domains, each of these showing different behaviour of the fault network. The blue cross are simulation that are shown in the following sections.

figure the distance is progressively increased to $D/L_{nuc} = 0.5$ (Fig. 3.14), $D/L_{nuc} = 1$ (Fig. 3.15) and finally $D/L_{nuc} = 5$ (Fig. 3.16). Although the first event was artificially nucleated on fault 1, the faults are synchronized after a few cycles. It seems that they tend to rupture closely in time. This effect was observed in paleoseismic studies in Eastern California shear zone where the 1992 M_w 7.3 Landers earthquake occurred (*Rockwell et al.*, 2000 ; *Ganev et al.*, 2010). On figures 3.12 and 3.13 the evolution of the phase diagram can be followed when the distance between the faults is increased. Basically, the domain of coexistence of slow and fast events shrinks for $D/L_{nuc} = 0.5$ and disappear for larger distance D/L_{nuc}.

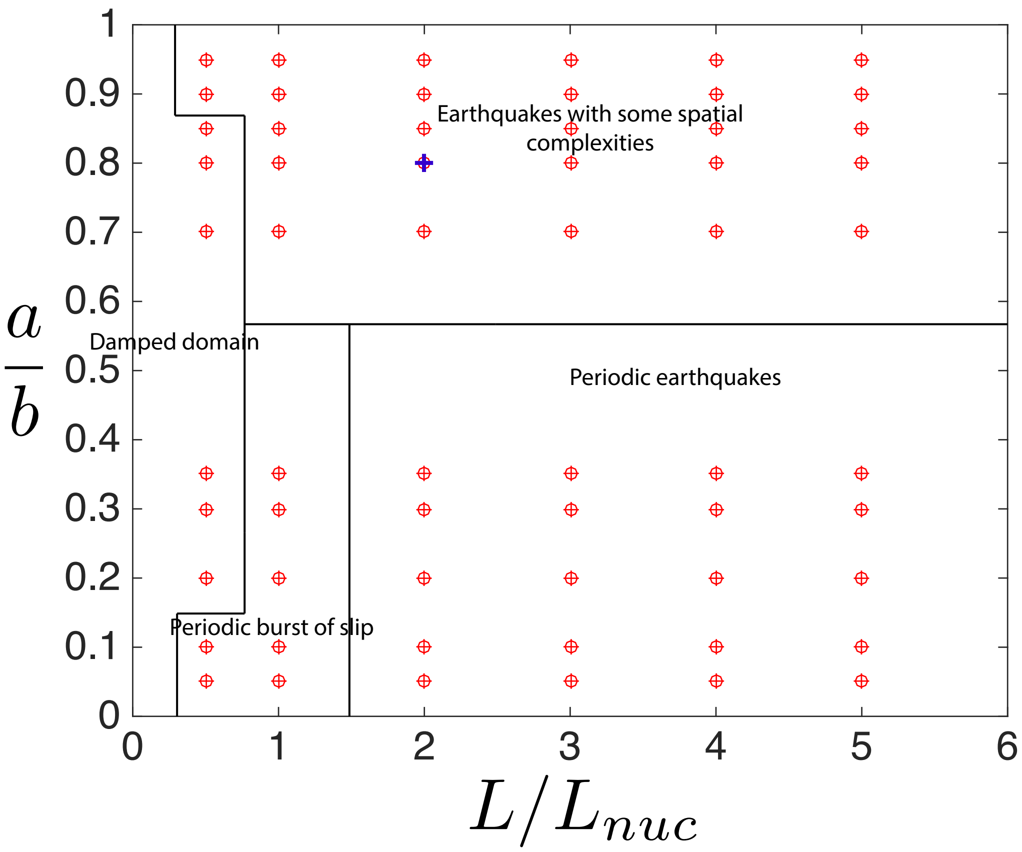

Figure 3.13 – Phase diagram showing the behaviour of two overlapping faults system. The distance between the fault is set to L_{nuc}. We can identify several domains, each of these showing different behaviour of the fault network. The blue cross are simulation that are shown in the following sections.

3.3.3 Variation around the geometry

Here we explored variation around the geometry of two overlapping faults. The distance between the faults is $D/L_{nuc} = 0.1$. The two parallel faults network (Fig. 3.17) and no overlap fault network (Fig. 3.20) do not show any slow events and all earthquake are extremely periodic. It seems that in a simple configuration like this one, a non zero overlap is necessary in order to get aperiodicity and complex nucleation and propagation of earthquakes. The two parallel fault network is the only configuration where earthquake seem not to synchronize but rather be well separated in time. In intermediate overlap (25% and 75%) a natural complexity arise, with slow slip events, afterslip and some small aperiodicity. Partial ruptures are only happening in the 75% overlap simulation (Fig. 3.18).

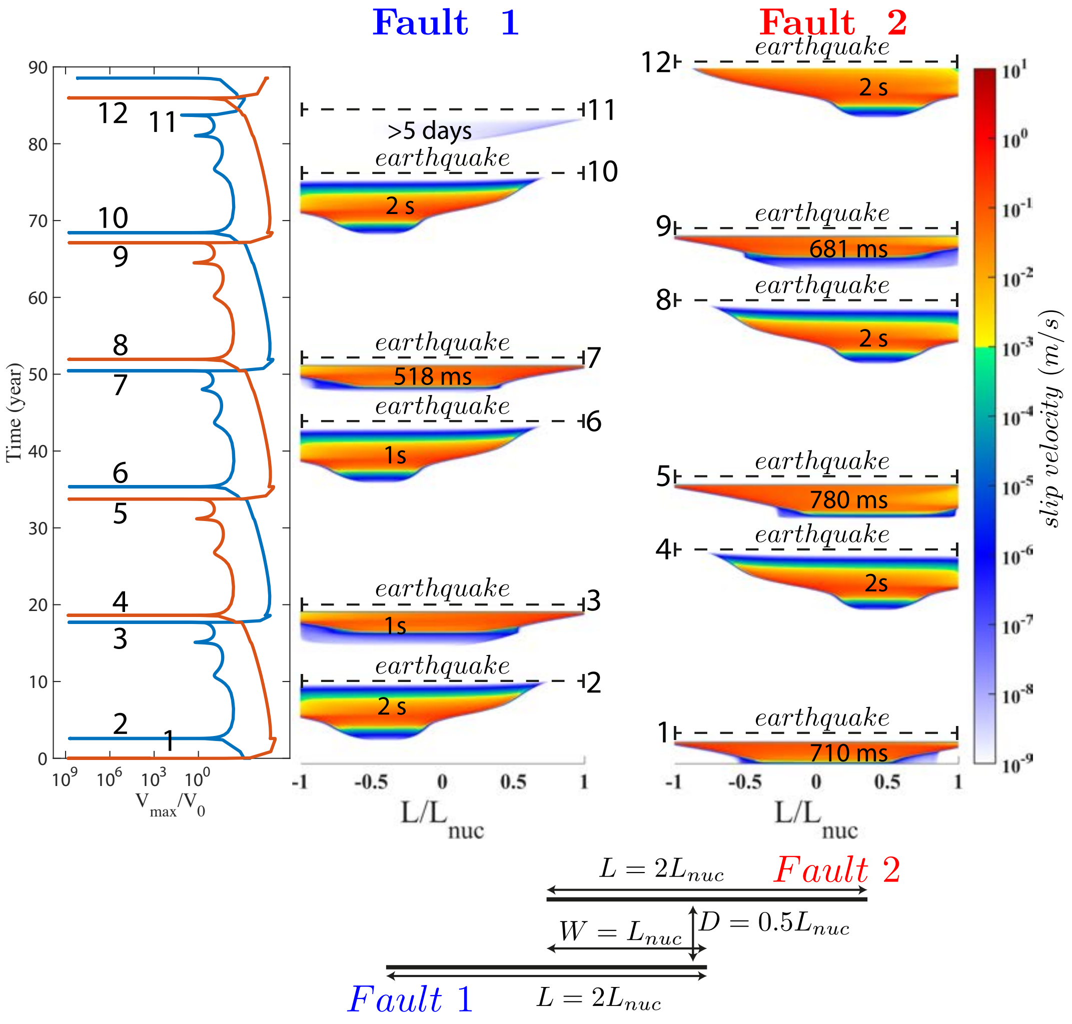

Figure 3.14 – Here the ratio is $a/b = 0.8$, the length of the fault is $L = 2L_{nuc}$ and the distance between the fault $D/L_{nuc} = 0.5$. It seems that the behaviour is in a limit cycle of compose of 2 regular cycles.

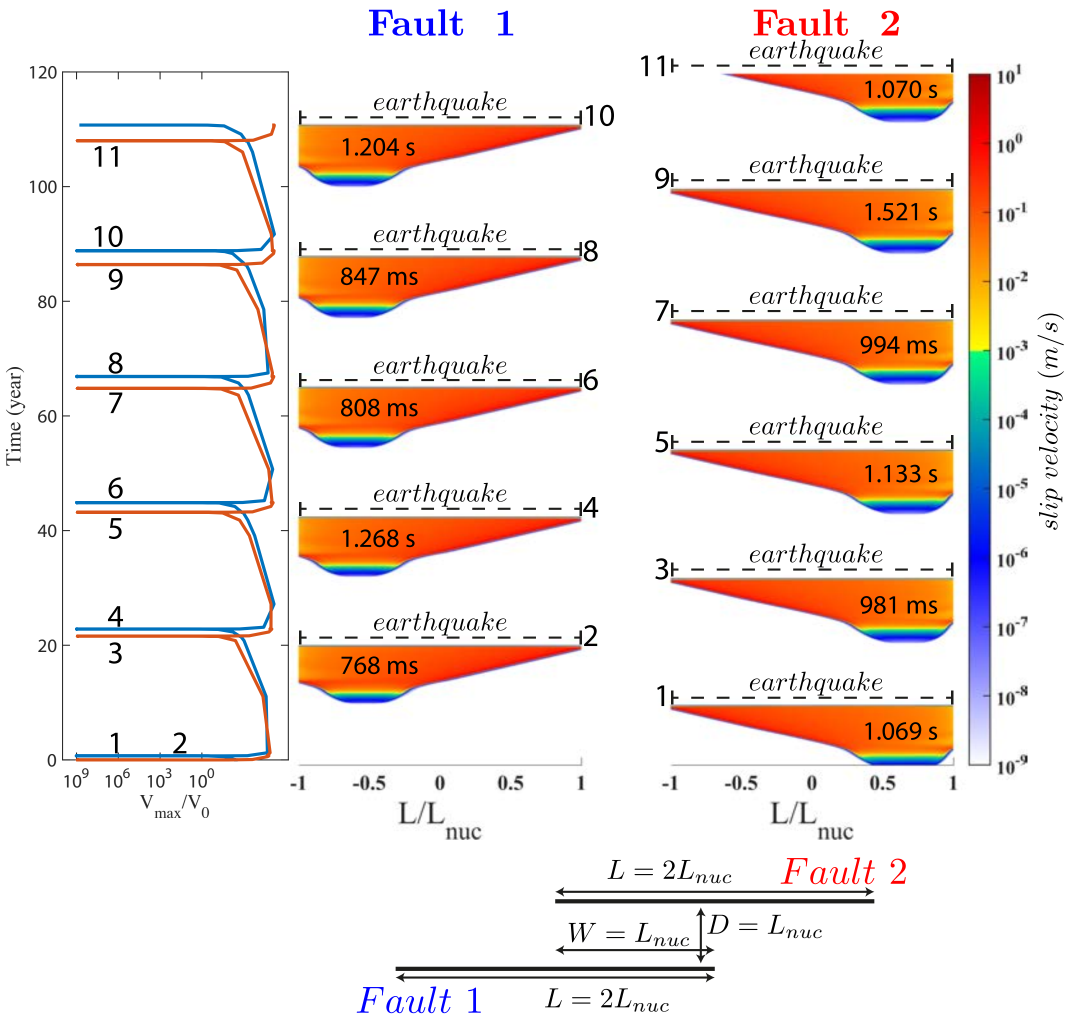

Figure 3.15 – Here the ratio is $a/b = 0.8$, the length of the fault is $L = 2L_{nuc}$ and the distance between the fault $D/L_{nuc} = 1$. The fault here is periodically rupturing into an earthquake. The only difference with the single fault simulation is the variability in the earthquake recurrence time and the location of the nucleation.

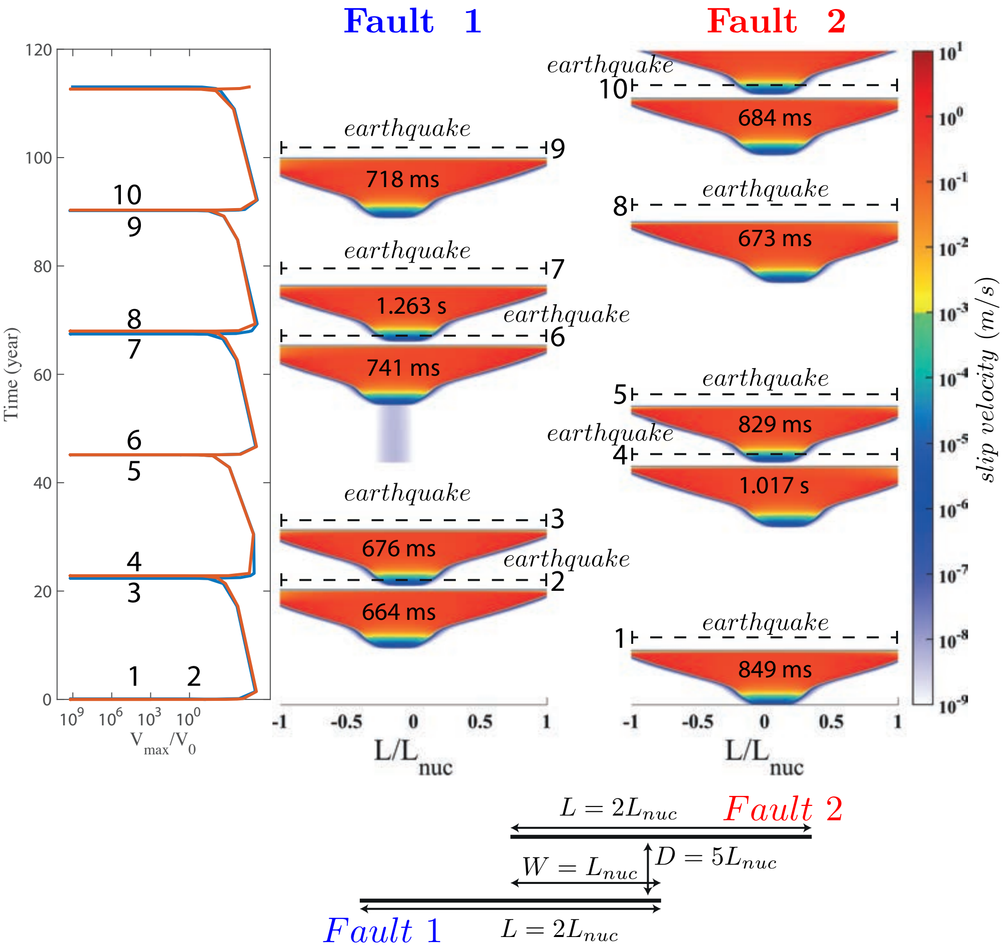

Figure 3.16 – Here the ratio is $a/b = 0.8$, the length of the fault is $L = 2L_{nuc}$ and the distance between the fault $D/L_{nuc} = 5$. Although the fault are quite far, their rupture time is close to each other like if they were synchronizing.

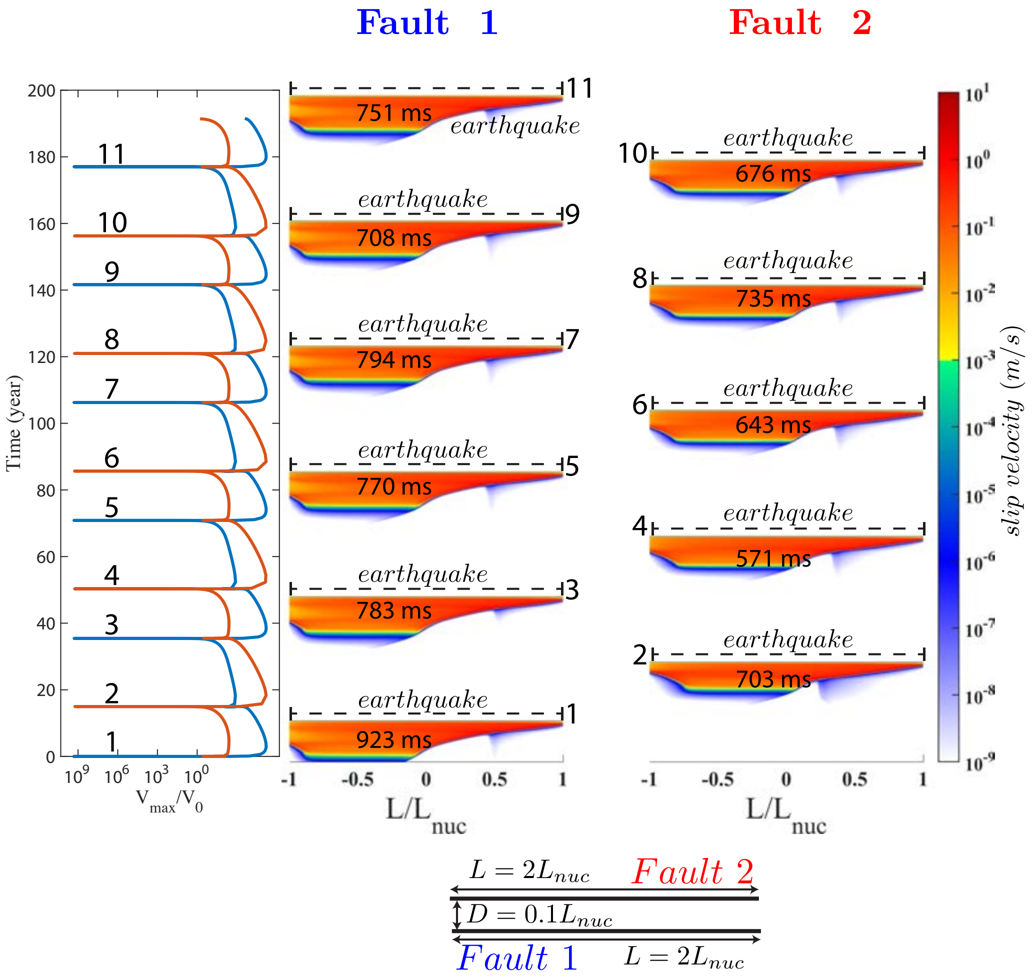

Figure 3.17 – Here the ratio is $a/b = 0.8$, the length of the fault is $L = 2L_{nuc}$ and the distance between the fault $D/L_{nuc} = 0.1$.

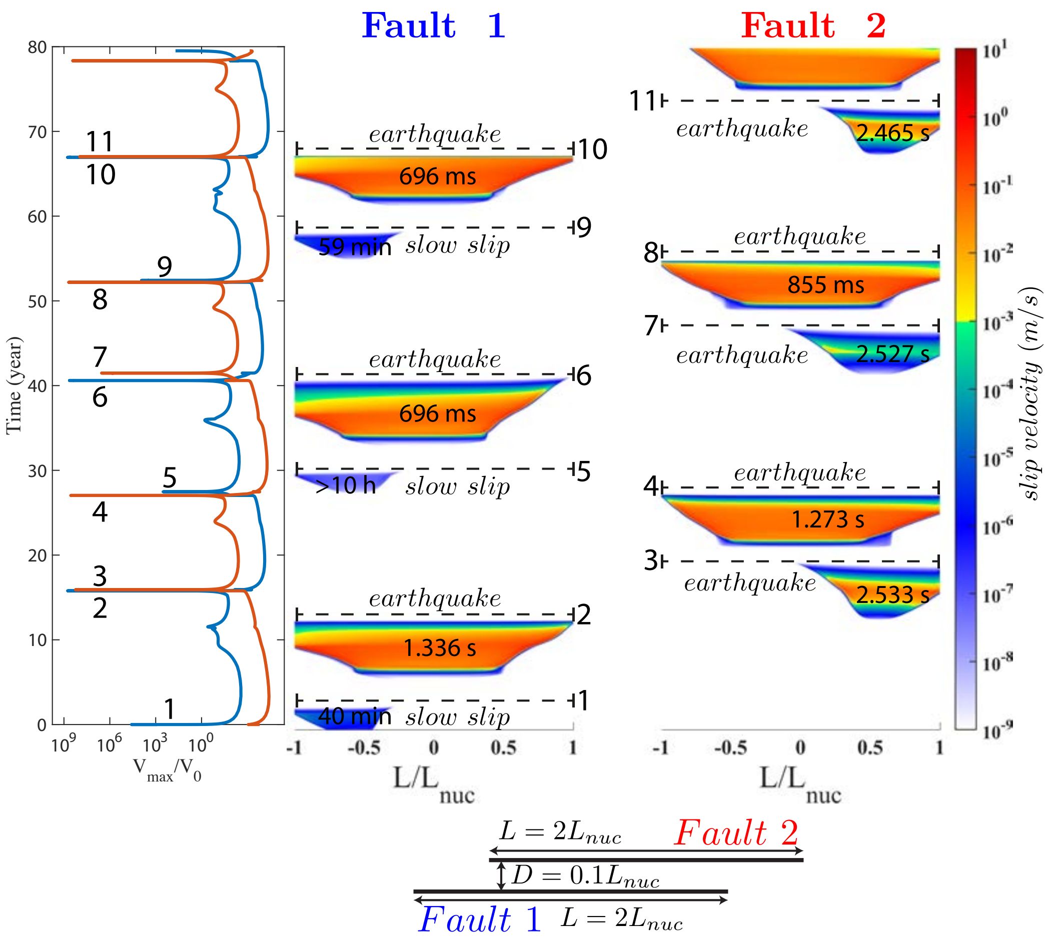

Figure 3.18 – Here the ratio is $a/b = 0.8$, the length of the fault is $L = 2L_{nuc}$ and the distance between the fault $D/L_{nuc} = 0.1$.

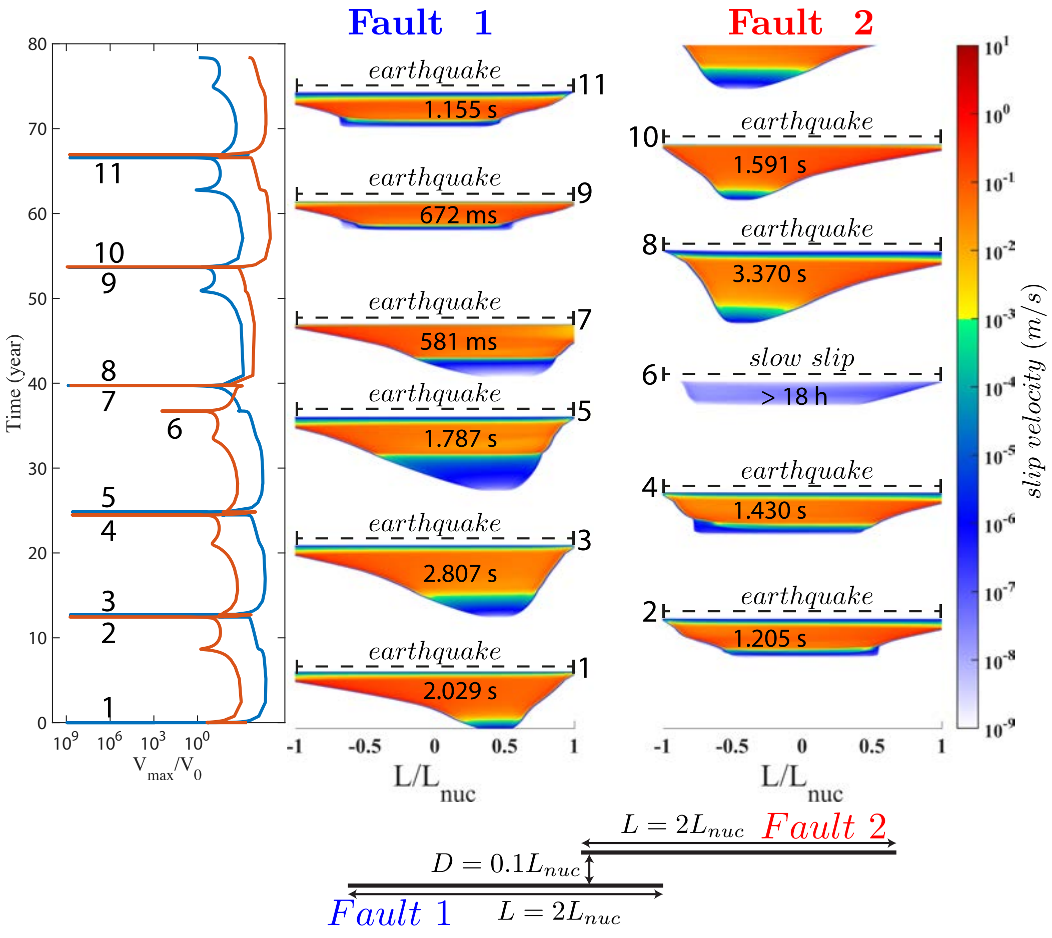

Figure 3.19 – Here the ratio is $a/b = 0.8$, the length of the fault is $L = 2L_{nuc}$ and the distance between the fault $D/L_{nuc} = 0.1$.

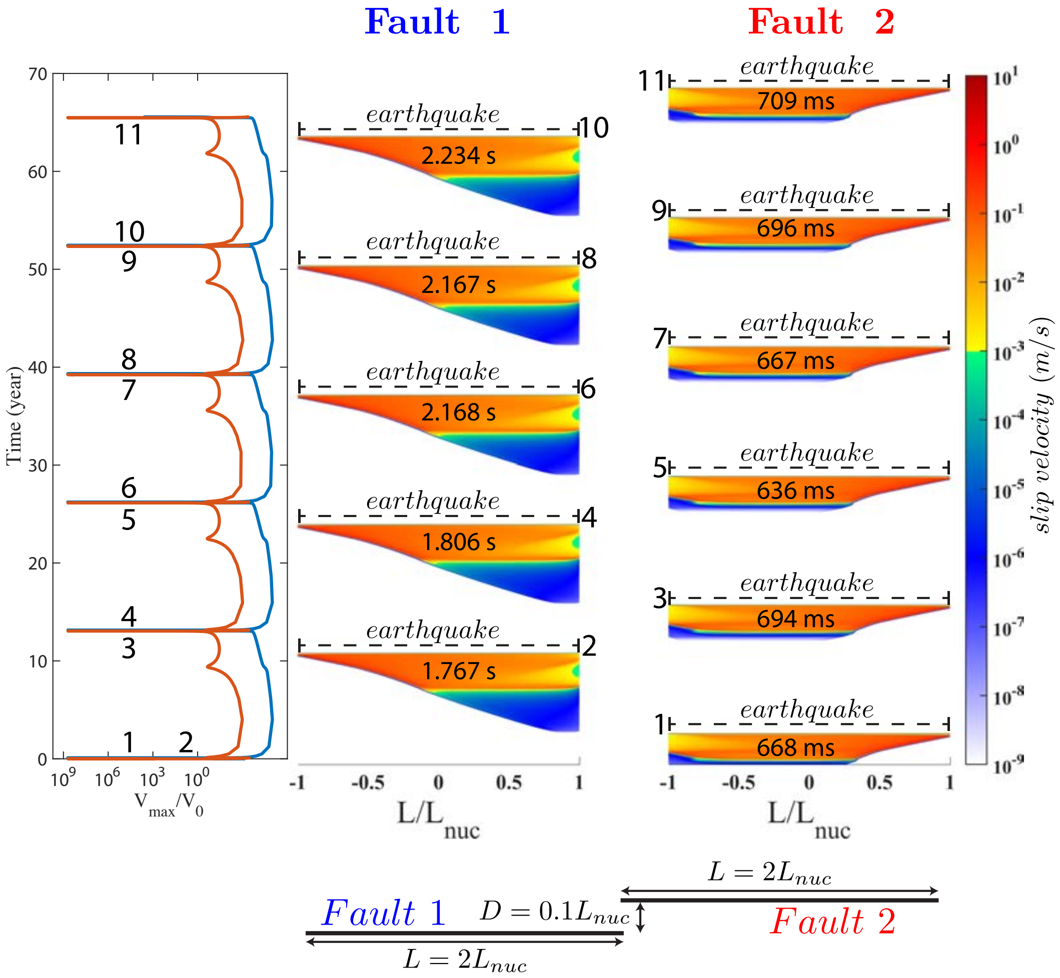

Figure 3.20 – Here the ratio is $a/b = 0.8$, the length of the fault is $L = 2L_{nuc}$ and the distance between the fault $D/L_{nuc} = 0.1$.

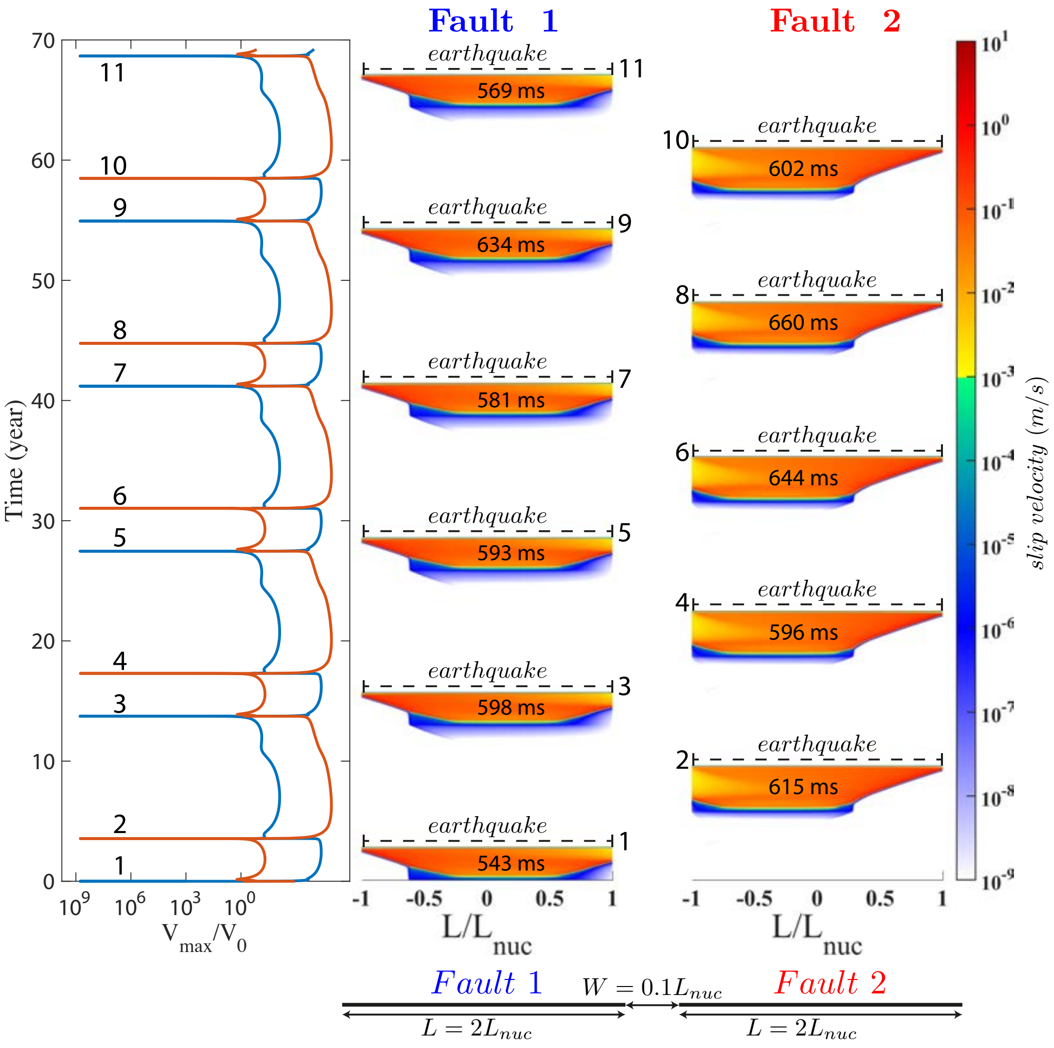

Figure 3.21 – Here the ratio is $a/b = 0.8$, the length of the fault is $L = 2L_{nuc}$ and the distance between the fault $D/L_{nuc} = 0.1$.

3.4 Statistics of slow and fast events

To study systematically the statistic of slow and fast events, a smaller subset of the simulation is taken where slow events are happening : $L/L_{nuc} \in \{1, 2, 3, 4\}$, $D/L_{nuc} \in \{0.1, 0.5, 1, 2, 3, 4\}$, $a/b \in \{0.7, 0.8, 0.85, 0.90, 0.95\}$.

For each of the parameters identified above we spin up the model, allowing the faults to undergo multiple earthquake cycles before measuring the slip and rupture velocity of each slow and dynamic event. We identify SSEs and earthquakes based on their slip and rupture velocity. SSEs are events with a slip velocity V in the range of 1μm/s to 1 mm/s and a rupture velocity V_{rup} lower than $0.01c_s$, where c_s is the shear wave speed. Earthquakes are events with a slip velocity greater than 1 mm/s and a rupture velocity greater than $0.01c_s$. We purposefully chose a relatively small threshold value for rupture velocity, because quasi-dynamic simulations lead to much slower rupture velocity than dynamic simulations (*Thomas et al.*, 2009). As our faults are one dimensional, we define the equivalent moment for a seismic or aseismic event as $M = \mu \bar{D} L_{rup} \times 1km$, where L_{rup} is the total length of the fault that slipped during an event (SSE or earthquake) and $\bar{D}$ is the slip averaged over the length L_{rup}. For earthquakes, we compute separately the seismic moment during the nucleation phase and the dynamic phase. For SSEs, moment accounts for the entire duration when the slip velocity exceeds 1 μm/s. We obtained about 3000 individual earthquakes and about 500 SSEs in our calculations when the faults hosted both earthquakes and SSEs. We find that the moment of both seismic and aseismic events modelled by rate and state friction law follows the same scaling as for events in nature from observational data (*Ide et al.*, 2007 ; *Peng and Gomberg*, 2010) (Fig. 3.22). Because we conducted our calculations in 2D, the moment of a dynamic event scales with its duration squared : $M \propto T^2$. Moment of our simulated events clearly depends on the ratio of constitutive parameters a/b. Since the nucleation length L_{nuc} increases with a/b and since we compare models with non-dimensionalised fault length, the real length of the fault, L, also increases when $a/b \to 1$, leading to bigger moment release and longer duration for events. To verify the robustness of this scaling law, we changed the maximum slip velocity criteria used to distinguish SSEs and earthquakes by one order of magnitude. This did not change the observed scaling.

The scaling emerges naturally from our conceptual model of fault geo-

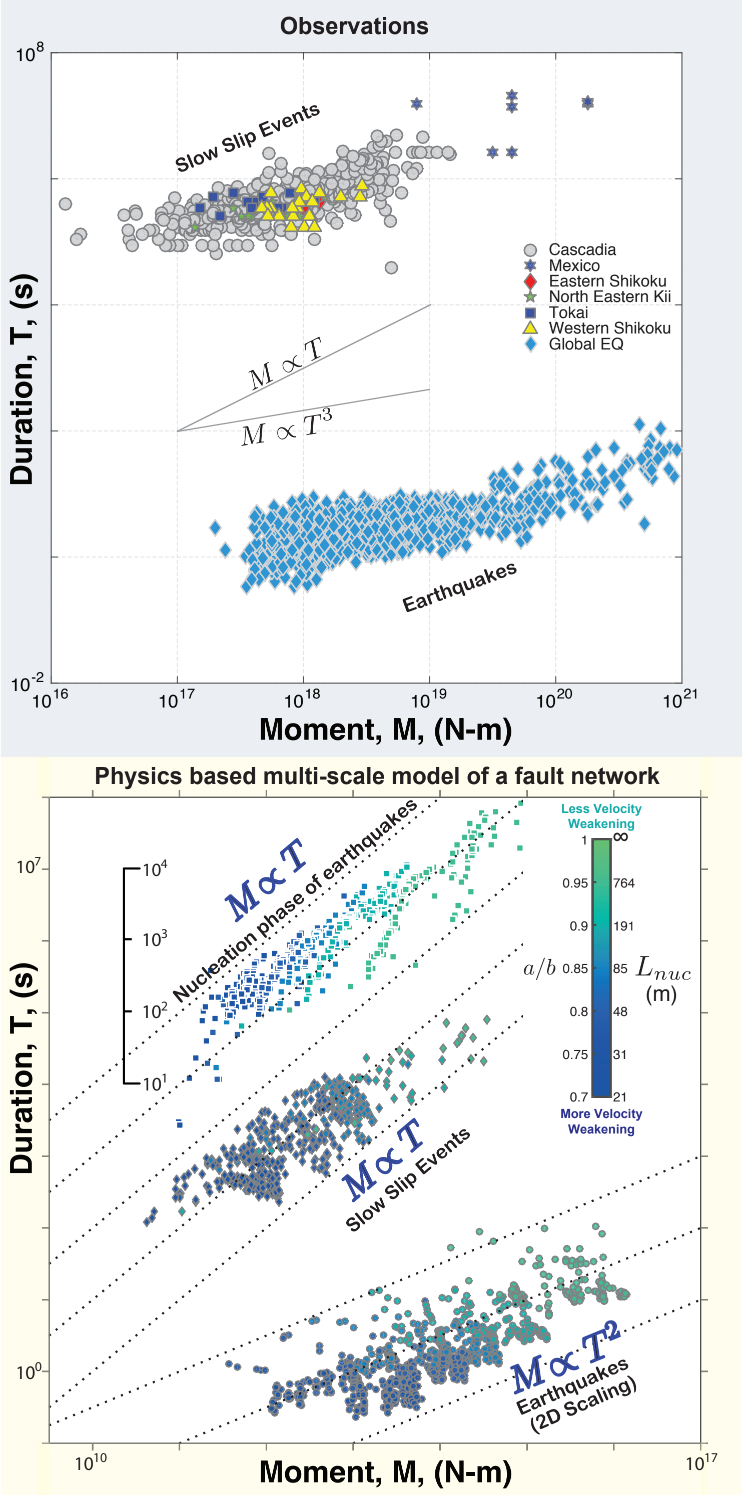

Figure 3.22 – Comparison of the scaling law for observational data (top panel) and from our all our calculations (bottom panel). We only used the seismic moment of the dynamic part of an earthquake.

metric complexity, without imposing any complexity in the spatial variation of frictional properties. However, we do not preclude the possibility that other models that have produced SSE's and earthquakes also reproduce such scaling laws. Another interesting feature that emerges from our calculations is that the moment of the nucleation phase of earthquakes also follows the same linear scaling with duration as slow-slip events. However, this similarity in scaling may disappear in 3D. We also notice that by adding the nucleation and after-slip moment's of earthquake, the clear scaling distinction between earthquakes and SSEs start vanishing and a continuum between the two modes of slip can be seen (Fig. 3.23).

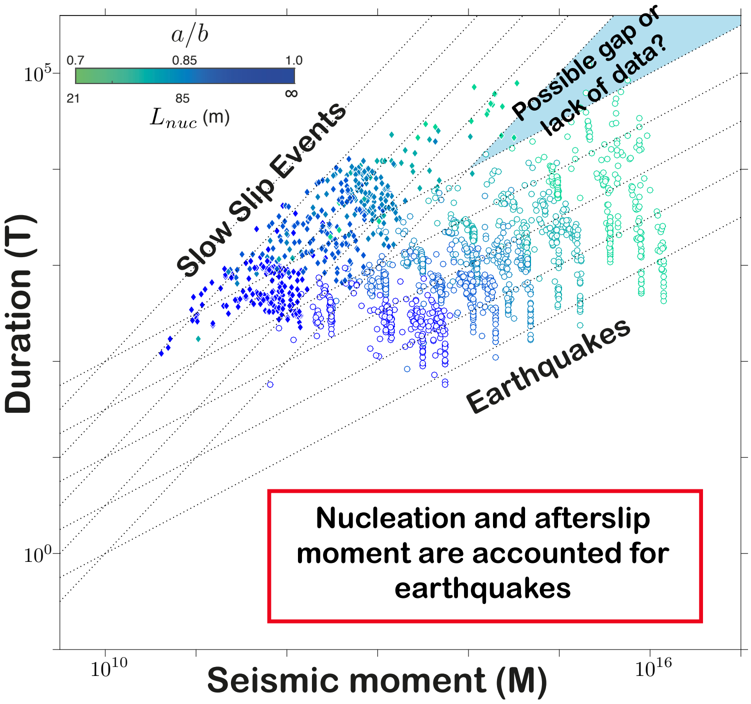

Figure 3.23 – Same as Fig. 3.22 but the moment of the earthquakes includes the nucleation and afterslip phases.

The temporal evolution of rupture length and slip for each event provides hints about the relative scaling between SSEs and earthquakes (Fig. 3.24). For earthquakes, the average growth of both rupture length and slip are linear with event duration, independent of a/b, hence independent of the actual length of the fault as we non-dimensionalised length scales by L_{nuc}. As a consequence, seismic moment grows quadratically with event duration. In other words, earthquakes propagate as an expanding crack : slip and rupture length are proportional to each other. For SSEs, however, the temporal evolution of slip and rupture length show a clear dependence on the fault length. For a given a/b, final rupture length is constant i.e. its independent of event duration. However, slip grows linearly with duration. If we now increase the fault length (i.e. increase a/b), the accumulated slip decreases (compared to the low a/b case) while the final rupture length increases (see arrows in slow-slip panel in Fig. 3.24). These two effects exactly counterbalance each other, such that the final moment scales linearly with duration and is independent of fault length (i.e. for different a/b). This highlights an interesting fact that SSEs are not necessarily self-similar at least in our calculations.Another interesting scaling that emerges is in the evolution of the moment of the nucleation phase with duration. It is also linear as for SSEs. The evolution of slip and rupture length for the nucleation phase is scale independent contrary to SSEs. Slip and final rupture length for nucleation phases evolve, individually, with the square root of the event duration.

Another interesting feature that emerges from our simulations lies in the static stress drop of both types of slip events i.e. SSEs and earthquakes (Fig. 3.25). We evaluated this parameter in three different ways (*Noda et al.*, 2013) : Seismological stress-drop is related to the seismic moment, M_0 and the length of the rupture, L_{rup}, as

$$\Delta\sigma_M = \frac{4}{\pi}\frac{M_0}{L_{rup}^2} \tag{3.4}$$

Spatial average of the stress-drop is evaluated using,

$$\Delta\sigma_A = \frac{\int_{L_{rup}} \Delta\sigma(l)\, dl}{L_{rup}} \tag{3.5}$$

And finally, the slip average stress drop is evaluated using the slip distribution, $\Delta u(x)$, as

$$\Delta\sigma_E = \frac{\int_{L_{rup}} \Delta\sigma(l)\Delta u(l)\, dl}{\int_{L_{rup}} \Delta u(l)\, dl} \tag{3.6}$$

Regardless of the method, the stress drops of SSEs and earthquakes are of similar order of magnitude. Earthquake stress drops are, on an average, about twice as large as those for SSEs. Also, as expected, the stress drop scales with the moment of individual earthquakes and SSEs. Such observation emphasises the relative importance of slow events in the stress/energy budget of active faults.

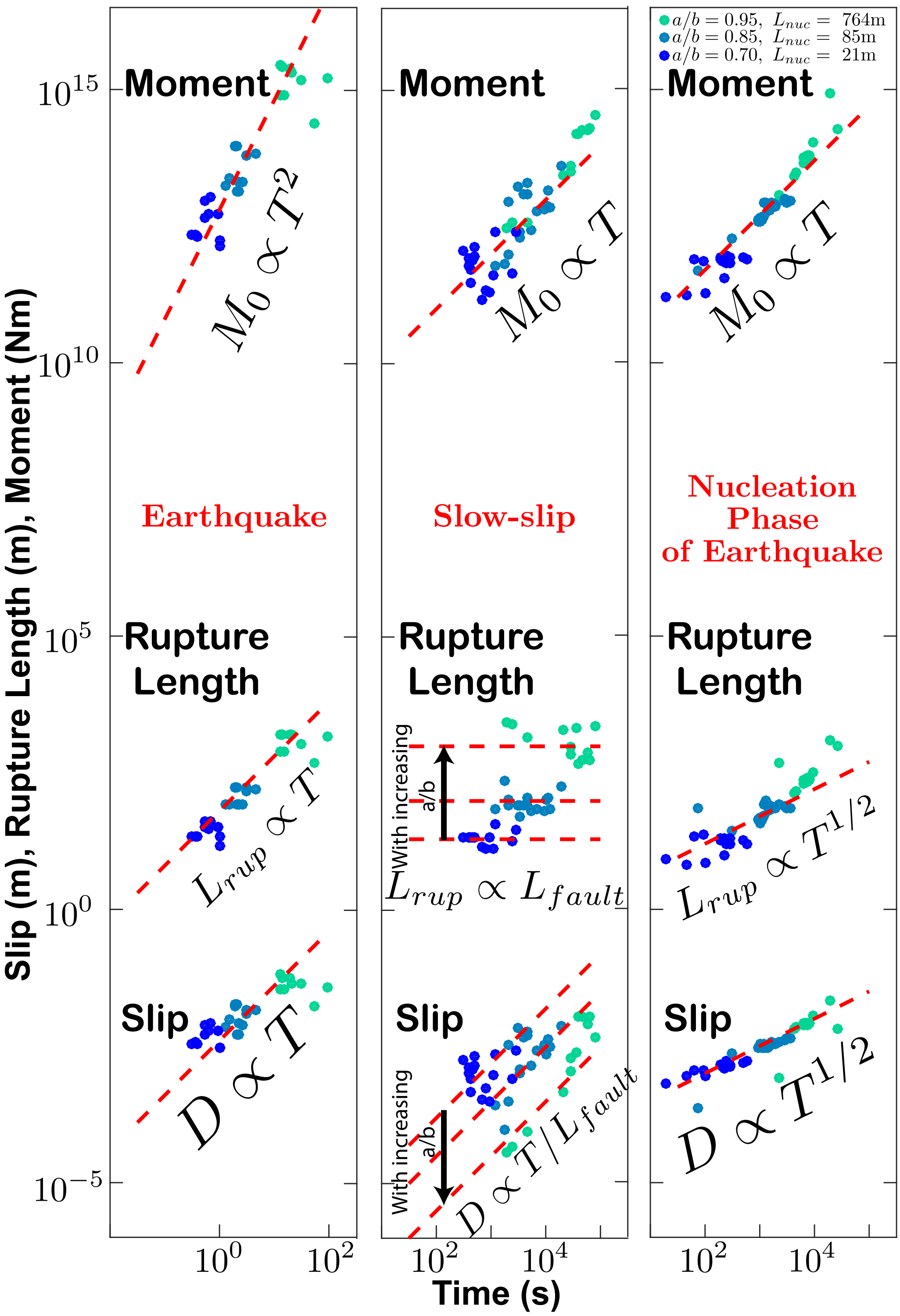

Figure 3.24 – Final moment, slip and rupture length with time for slow-slip events, earthquakes and nucleation phase of earthquakes.

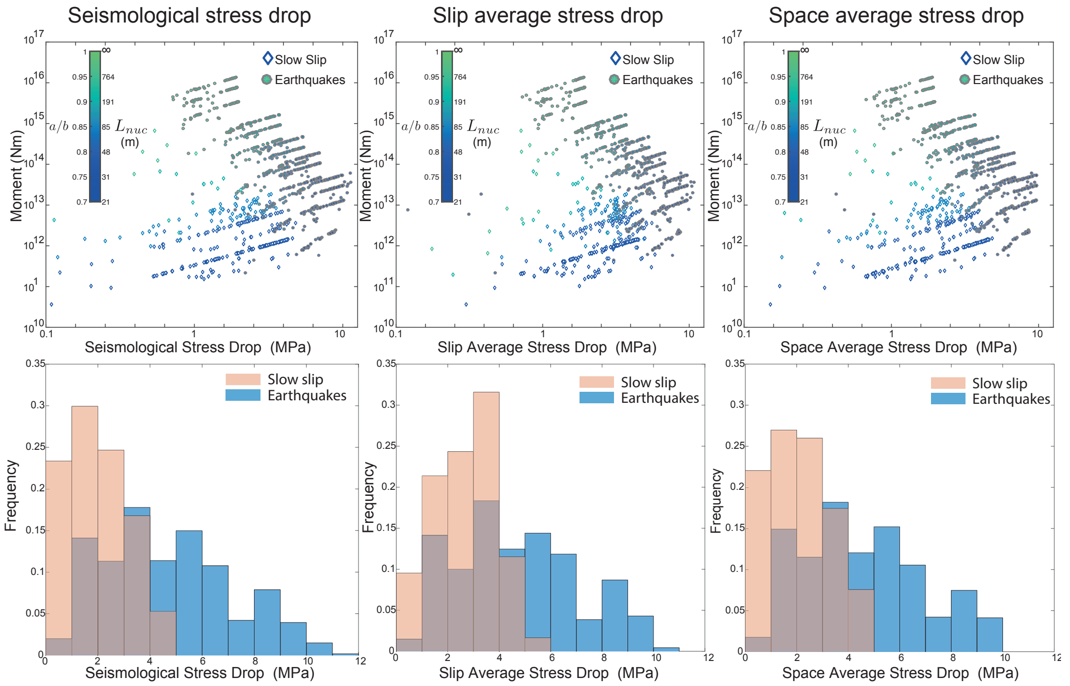

Figure 3.25 – Comparison of seismological, slip average and spatially averaged stress drops and their distributions for slow-slip events and earthquakes.

3.5 Conclusion

Our work here suggests that slow-slip event dynamics may be controlled by fault geometrical complexities just as it has been shown to control the dynamics of ordinary earthquakes (*Lay and Kanamori*, 1981). Unlike the current *planar fault* asperity based rate-and-state models (with rate-strengthening and rate-weakening patches), the faults in our model are uniformly rate-weakening. Thus, the same segment of a fault can host both slow-slip events and earthquakes (events 5,6 and 8 in Fig. 3.9). This is not possible in the asperity based models since a large rate-weakening asperity ($L > L_{nuc}$) will always rupture seismically and a small rate-weakening asperity ($L \sim L_{nuc}$) will sometimes lead to aborted nucleation of dynamic events (*Veedu and Barbot*, 2016). However, as we have shown in Fig. 3.24, the rupture length and slip during the nucleation phase follow different scaling behaviour as opposed to slow-slip events.

Numerous natural observations like occurrences of unexpected spontaneous slow-slip events (*Rousset et al.*, 2016 ; *Wallace et al.*, 2016), and more generally all SSEs, cannot be explained by the current asperity-based rate-and-state models without appealing to competing mechanisms. Within our framework, there is no need to exclusively invoke more complex weakening processes in rate-strengthening zones, like thermal pressurization, to explain shallow slip or to ad-hoc tuning of parameters. The greatest strength of the asperity based model is to explain the occurrence of afterslip by the relaxation of a large stress perturbation in a rate-strengthening region of a fault (*Perfettini et al.*, 2010). Our model shows that a fault segment next to a rupture zone can undergo aseismic slip as it would do in the case of afterslip (Fig. 3.9). Now that we have shown that complex stress perturbations, like those induced by complex fault geometry, lead to the emergence of a whole complexity of modes of slip, it would not be unsafe to imagine active faults with only weakening properties, either spatially homogeneous or heterogeneous. However, it is quite possible that natural faults do obey an asperity based model but a unified model that explains all the observations has to invariably account for geometric segmentation and/or the non-planar nature of the subduction zone faults that results in a spatio-temporally inhomogenous stress accumulation rate (*Mitsui and Hirahara*, 2006 ; *Matsuzawa et al.*, 2013 ; *Li and Liu*, 2016).

We showed that a simple, conceptual, physics based mechanical model (two interacting faults with an overlap) can produce slow-slip events and earthquakes on the same rate-weakening segment of a fault whose length is much larger than the nucleation length. We also reproduce the observed scaling law of moment with the duration of an event. This is, to the authors knowledge, the first time that the scaling law for slow and fast events is reproduced in the rate and state framework with uniform frictional properties. The only key ingredient needed in our model is continuous, aperiodic, stress perturbations from nearby faults. This is quite easily testable, as a ‘single fault’ inferred from seismology or geodesy is in fact a network of faults at various length scales (*Candela et al.*, 2012).

Chapitre 4

Perspectives

Avant-propos

Cette section présente des résultats récents et qui mériteraient d'être approfondis. C'est le seul chapitre où l'on utilise véritablement les simulations d'élasticité dans le plan (in-plane). Cela est dû au fait que l'implémentation des matrices hiérarchiques, qui permet de simuler le mode II, est relativement récente : c'est le fruit d'une collaboration avec Stéphanie Chaillat, qui travaille à l'ENSTA, en avril 2017. Dans ce chapitre nous présentons trois problèmes que notre modèle permet d'explorer. Ceci est une présentation préliminaire des premiers résultats obtenus en élasticité "in-plane". Dans un premier temps nous explorons la rugosité des failles et montrons qu'une complexité emerge naturellement en élasticité "in-plane", mais pas en élasticité "out-of-plane". Le deuxième problème est une injection de fluide sur une faille, pour ce faire, nous avons modélisé la diffusion de pression de pore. Nous regardons l'effet de la diffusivité ainsi que de la localisation du puit d'injection. Le troisième problème est un problème de cycle sismique dans une géométrie complexe de faille. Nous avons choisi la géométrie de l'Eastern California Shear Zone, où a eu lieu le séisme de Landers.

4.1 Fault roughness

4.1.1 Introduction

Natural faults show geometrical roughness at all scales (*Power et al.*, 1987 ; *Schmittbuhl et al.*, 1993 ; *Lee and Bruhn*, 1996 ; *Renard et al.*, 2006 ; *Candela et al.*, 2009, 2012). However, this problem of fault geometrical roughness has been poorly addressed in the earthquake source community. Particularly, the effect of fault roughness on the seismic cycle remains poorly understood. We still do not know what is the mechanical effect of roughness on the rupture propagation. How does the roughness of the fault affect the long term behavior of faults ? Will some parts of the fault be completely blocked after a few cycles due to the roughness ? Does this make parts of the faults more eligible for sliding ? Does this emphasize slow-slip events ? Can the roughness itself stop a rupture ? Do scaling laws emerge from this kind of complexity ? In this work, we took advantage of the new method we developed, to try to answer some of these questions.

We generated self-similar profiles of fault following *Dunham et al.* (2011). We considered 1D profiles that have the form :

$$y = h(x) \tag{4.1}$$

Given such a profile, a measure of the roughness is the root mean square height of a given length of the fault L (*Dunham et al.*, 2011) :

$$h_{rms}(L) = \sqrt{\frac{1}{L}\int_{-L/1}^{L/2} h^2(x)\mathrm{d}x} \tag{4.2}$$

In the particular case of self similar profile, the h_{rms} is proportional to the length of the fault (*Dunham et al.*, 2011) :

$$h_{rms}(L) = \alpha L \tag{4.3}$$

Where α is the amplitude to wavelength ratio. This parameter is being used to define the roughness of our faults. Usually real faults shows amplitude to wavelength ratio of order $10^{-2} - 10^{-3}$ (*Power and Tullis*, 1991).

4.1.2 Rough fault in out-of-plane configuration

Figure 4.1 and figure 4.2 show two examples of seismic cycles on a rough fault. The faults are in out-of plane geometry, the direction of slip is perpen-

Name	symbol	Value
Reference friction coefficient	f_0	0.6
Reference velocity	V_0	10^{-9} m/s
Critical slip distance	D_c	0.1 mm
Rate and state parameter	a	0.008
Rate and state parameter	b	0.01
Shear rate loading	$\dot{\sigma}_{23}$	0.001 Pa/s
Normal stress	σ_n	10 MPa
Shear modulus	μ	30GPa
Shear velocity	c_s	3000 m/s
Dilatational velocity	c_p	5000 m/s
Resulting nucleation length scale (out-of-plane)	L_{nuc}	477 m
Resulting nucleation length scale (in-plane)	L_{nuc}	611 m

Table 4.1 – Table of constant parameters among all the simulation shown in this section.

dicular to the propagation of rupture. For a normal range of roughness of the fault $\alpha = 0.001$ (Fig. 4.1), the behavior of the seismic cycle is close to the behavior of a single fault system : earthquakes are rupturing periodically, and they all look similar. However, the only specificity of this simulation of a rough fault is the location of the nucleation that is not at the center of the fault. The nucleation happens in an area where the normal stress is globally decreasing. If we now consider the upper range of roughness of natural faults $\alpha = 0.01$ (Fig. 4.2), the only difference with the first simulation is that the size of the nucleation is slightly increasing. This is an hint that in out-of-plane simulations, the roughness of the fault does not lead to natural complexity of the seismic cycle.

4.1.3 Rough fault in in-plane configuration

What is changing ?

The previous section was realised using exclusively out-of-plane geometry. In this particular setting, the rupture propagation is perpendicular to the slip direction on the fault. If we considered some roughness of the fault, it

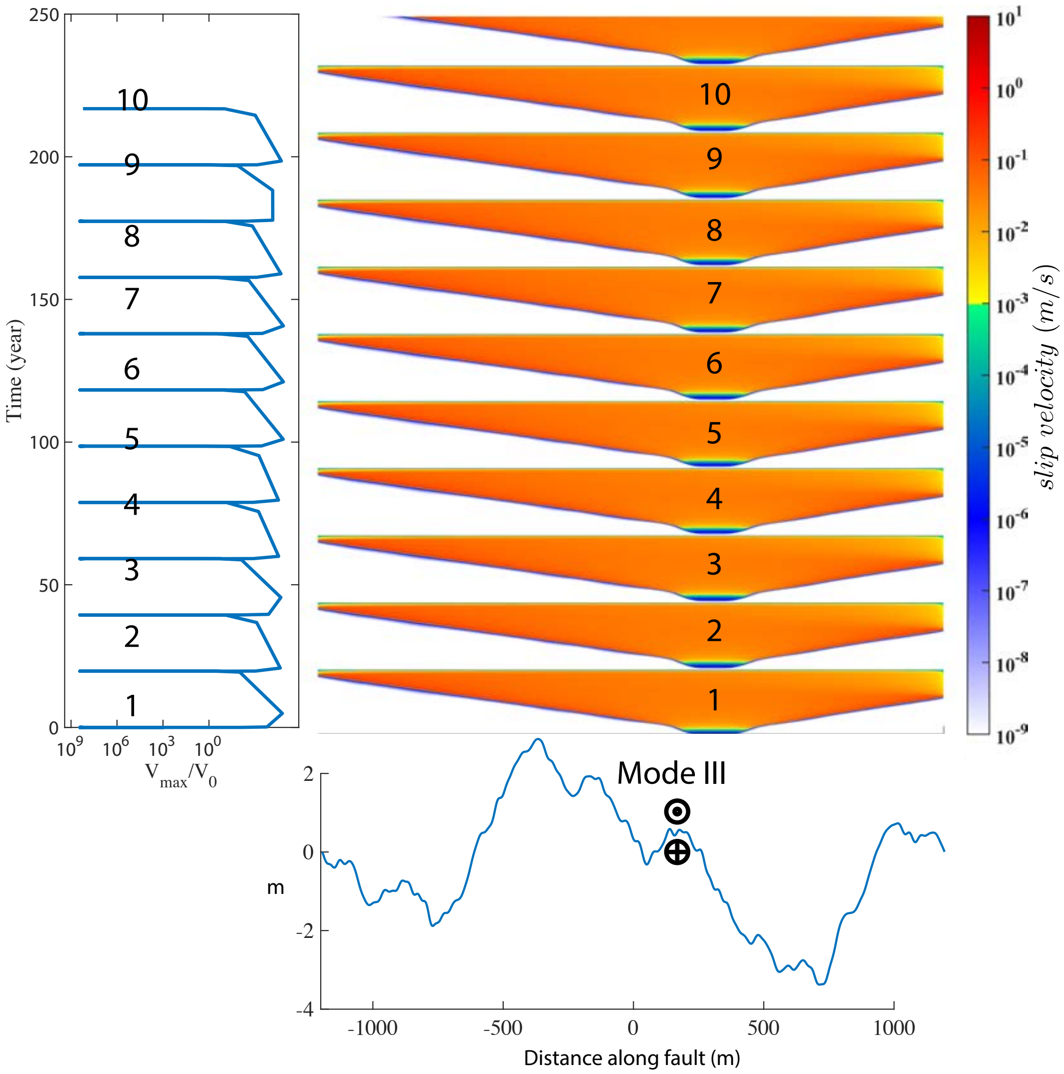

Figure 4.1 – Example of a rough fault geometry in out-of-plane configuration. Here the amplitude to wavelength ratio is $\alpha = 0.001$.

means that the slip direction is not forced to change its direction to follow the geometry of the fault (Fig. 4.1 and Fig. 4.2). Moreover, there is no normal stress change due to slip distribution on the fault. This is changing when considering in-plane elasticity. Here the slip direction is changing direction with the fault geometry, and the normal stress is changing when the fault is sliding. This raises different questions to understand in what extend this affects the behavior of the fault system. Because normal stress is changing, and the nucleation length scale is inversely proportional to the normal stress,

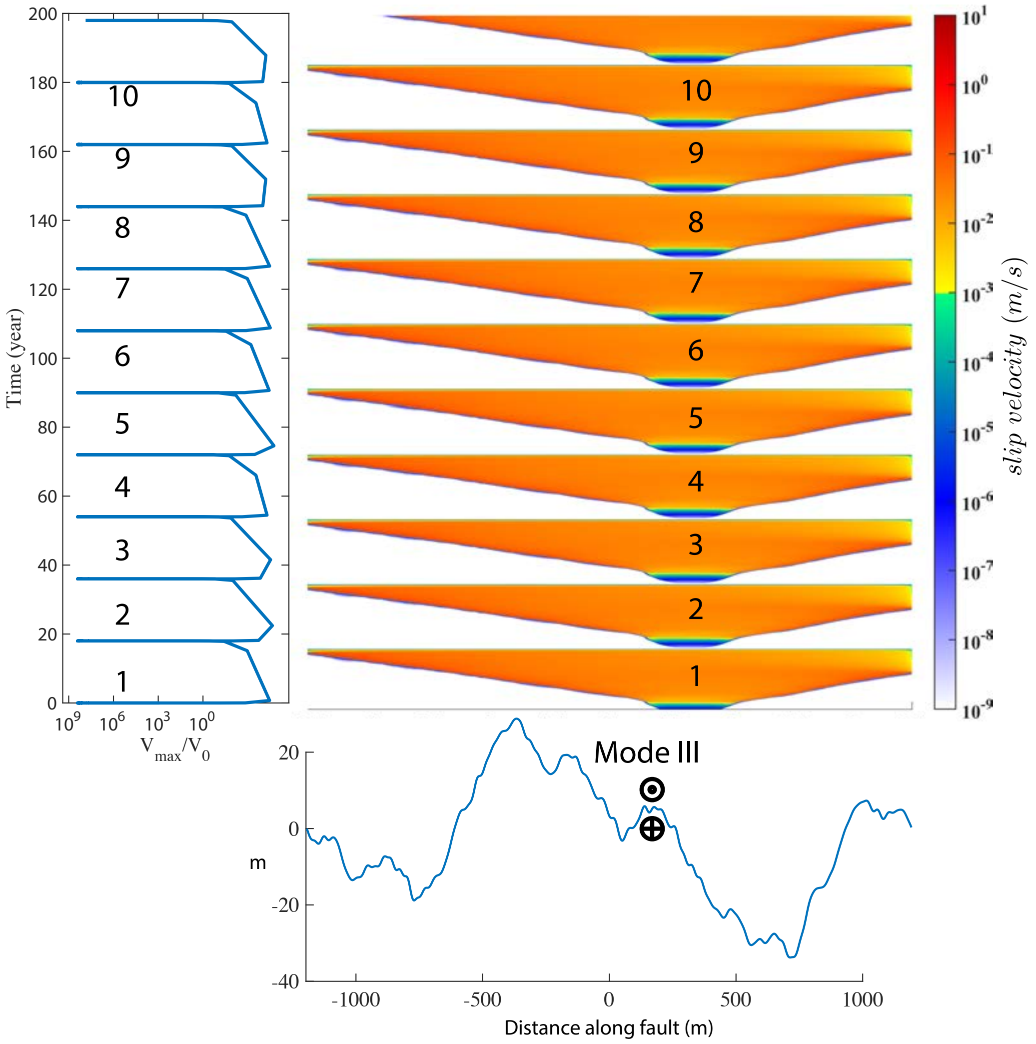

Figure 4.2 – Example of a rough fault geometry in out-of-plane configuration. Here the amplitude to wavelength ratio is $\alpha = 0.01$.

the nucleation length scale will change in time and space in the in-plane simulations. It can be expected that some part of the fault, with decreasing normal stress, will experience more slow-slip events than other part where the normal stress increases. It is really the case ? The long term loading will also affect differently the fault at each location. In the next sections, we will try to answer these questions.

Limitation of mode II

One limitation of the model described here is that while it is possible to release the shear stress on the fault by sliding, there is not way to release the normal stress that accumulate on the fault (Fig. 4.3). This normal stress keeps increasing (or decreasing) because the slip keeps accumulating. This affects the calculation when running simulation over long time, because of the lack of way to release this normal stress, it can sometimes reverse and become extensional. To avoid this behavior, a new criteria for normal stress is set. If the normal stress at a given point is less than 1MPa, the normal stress at that particular point does not evolve anymore. This is done by modifying the equation (4.5) at this particular point to :

$$\dot{\sigma}_n = 0 \tag{4.4}$$

This also has a strong influence on the accuracy of the calculation. Indeed, the accuracy in our simulation is set such that the length scale $L_b = \mu D_c / \sigma_n b$ is well discretized. Most of the time in our simulations, the grid size is set to be 10% of L_b. The problems is that in some part of the fault, the normal stress keeps increasing. Hence L_b, that is inversely proportional to the normal stress, keeps decreasing and the accuracy gets loss. This effect depends on the geometry of the fault and the loading rate.

Effect of roughness in in-plane configuration

Figure 4.4 shows the effect of roughness for a alpha ratio $\alpha = 0.001$. Here the seismic cycle is periodic, and all the events are dynamic. However, contrary to the simulation in out-of-plane configuration, here the nucleation phase gets more complex with every seismic cycle run ; it takes more time and it shows acceleration and deceleration of the rupture. This is maybe an explanation for the foreshocks happening sometime before earthquakes. This is an effect of the normal stress on the fault, that keeps increasing or decreasing on some part, and finally brings strong heterogeneity on normal stress for this fault. When the amplitude to wavelength ratio is increased by one order of magnitude $\alpha = 0.01$, the effect of normal stress appears only after one or two cycles (Fig. 4.5). This figure shows extremely complex events, slow and fast event, with partial ruptures and aperiodicity. Slow events are

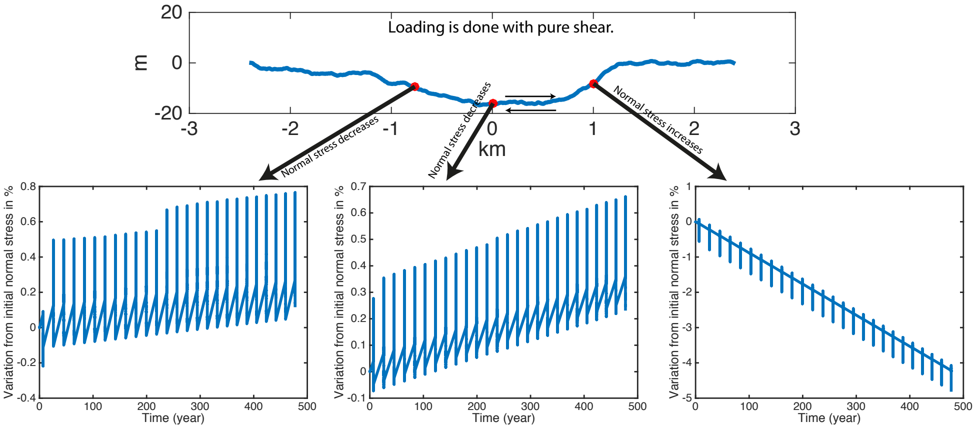

Figure 4.3 – Figure showing one drawback of this model, there is no way to release normal stress on the fault, so that the stress just builds up indefinitely, until the normal stress becomes extensional. The simulation are stopped if it happens. A rough geometry is used, and the normal stress variation from the initial at three different points is computed. A pure shear loading is applied so that some part of the fault will experience increase or decrease in normal stress. A In this simulation : $a = 0.008$, $b = 0.01$, initial normal stress $\sigma_n = 10^7$Pa.

present in figure 4.5, despite the fact that the fault is unique and much larger than the nucleation length scale ($L = 5L_{nuc}$).

The problem of accuracy loss because of increasing normal stress is visible by comparing figure 4.5 and 4.6. In figure 4.6 the grid size was divide by 2, hence making the simulation more accurate. Very quickly the two simulations are diverging, making the problems of rough fault difficult computationally. As previously mentioned, this is probably an effect of the increasing of normal stress on a specific part of the fault, that reduces locally the L_b length scale.

4.1.4 Discussion and conclusion

In this section, we showed that behaviors of seismic cycles differs drastically considering either in-plane or out-of plane elasticity. In out-of-plane simulation, the roughness play a small role, there is no accumulation of normal stress on the fault. Hence the behavior is classic to a single straight fault system except that the nucleation location is determined by the roughness and probably the loading. However in in-plane simulation, roughness of the

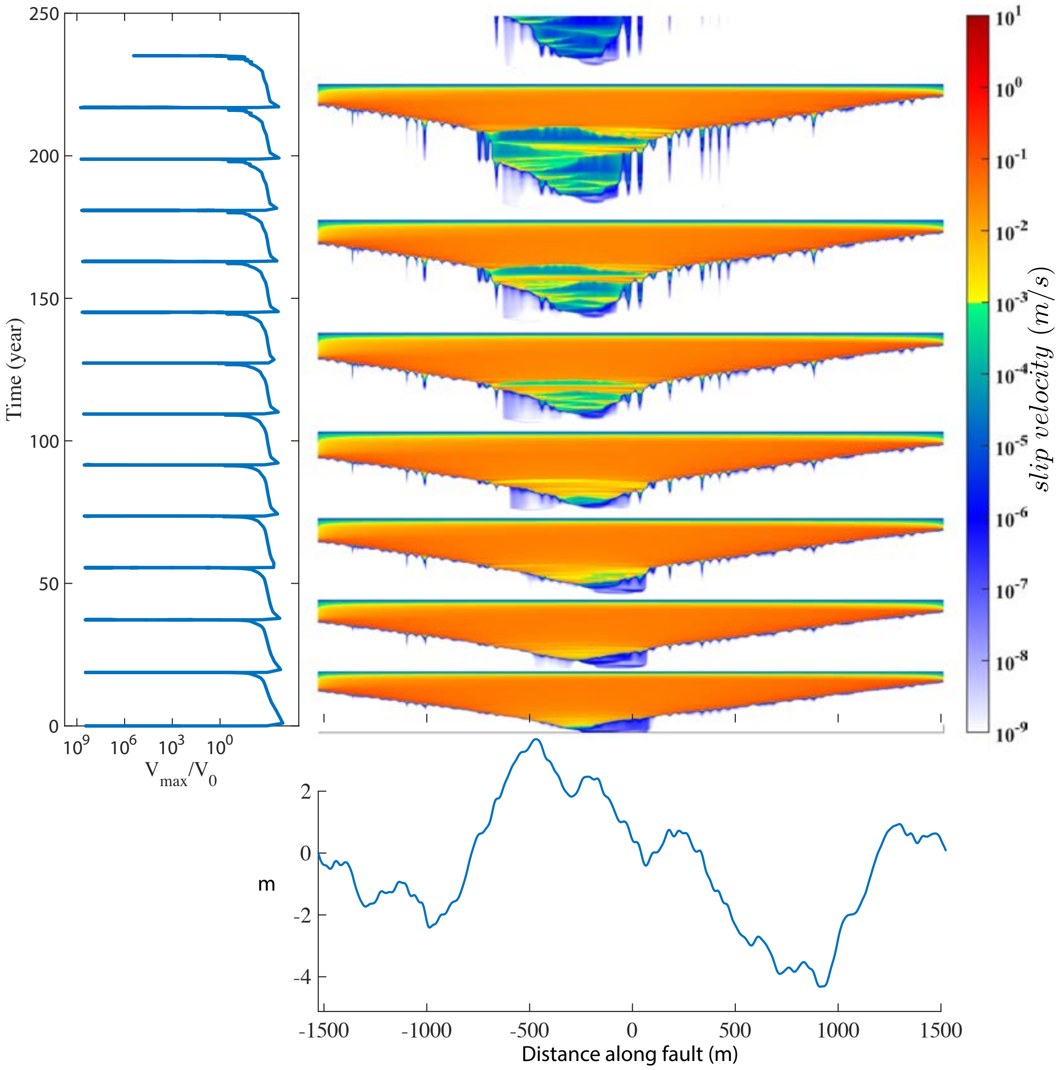

Figure 4.4 – Example of a rough fault in in-plane configuration. Here the amplitude to wavelength ratio is $\alpha = 0.001$. Notice that after a few cycles, the nucleation becomes very complex.

fault has a strong influence of the seismic cycle : normal stress keeps accumulating over cycles making parts of the faults blocked. A diversity of size and type of events emerge from these simulations, hence making the roughness a plausible candidate to : 1) provoke arrest of ruptures, especially at kinks, 2) Enhance the presence of slow phenomenas 3) prone complex nucleation phase of earthquake. An interesting feature that appears with rough fault is the size distribution that is created despite a length greater than the nucleation length scale ($L = 5L_{nuc}$). Hence it would not be unsafe to consider the nucleation length scale to be extremely small, allowing for small earth-

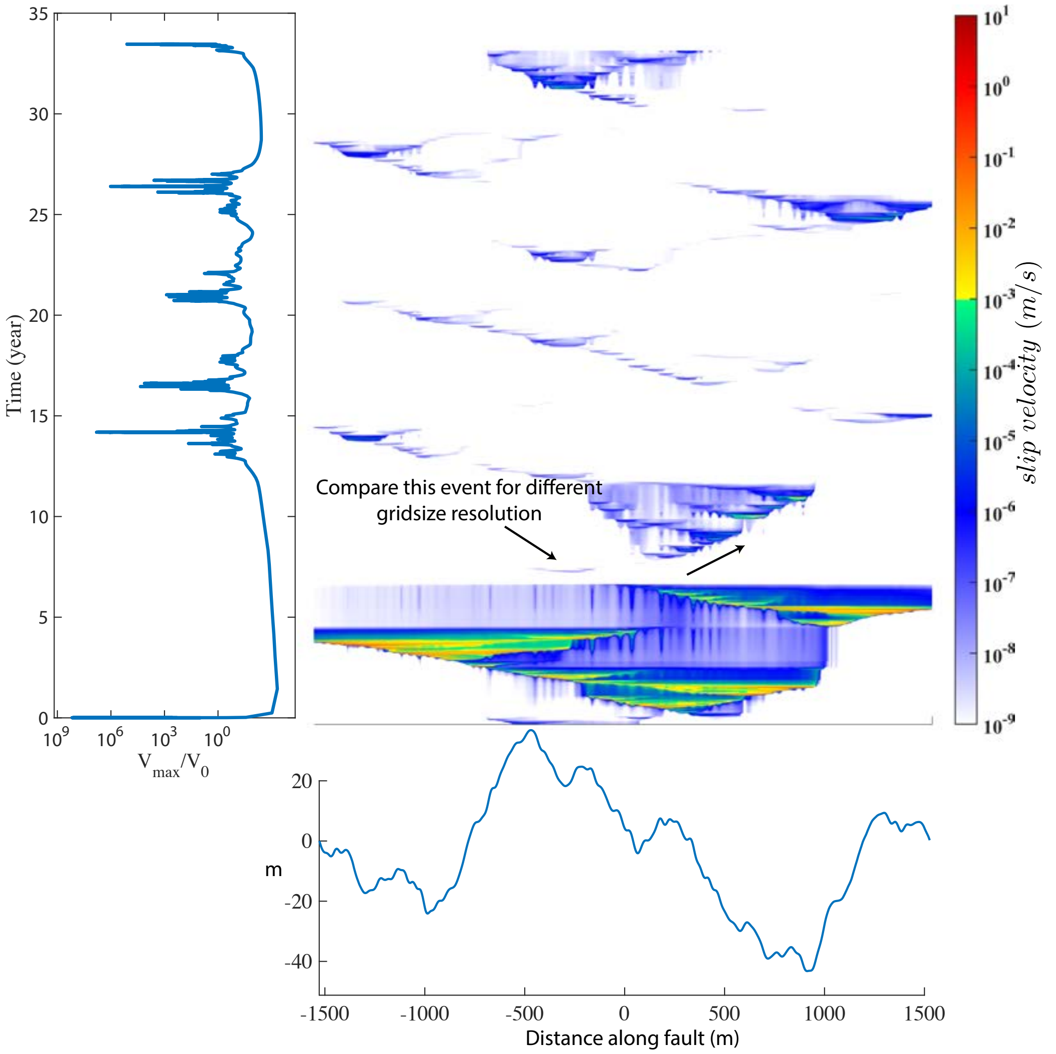

Figure 4.5 – Example of a rough fault in in-plane configuration. Here the amplitude to wavelength ratio is $\alpha = 0.01$.

quakes, that would be limited to grow only by the roughness of the fault. This may resolve one of the actual paradox, where the size distribution of events that one can get in simulations, is really restricted by the size of the fault and the nucleation length scale. An other complementary effect is that this small nucleation length scale will naturally vary. The limitation that in in-plane, there is no mechanism to release the normal stress accumulated over cycles is an hint that other mechanisms should be considered. 3D simulations could resolve some of these limitations by allowing for different direction of slip. An other explanation would be to appeal to micro damage to release the accumulated normal stress close or on the fault (Thomas et al.,

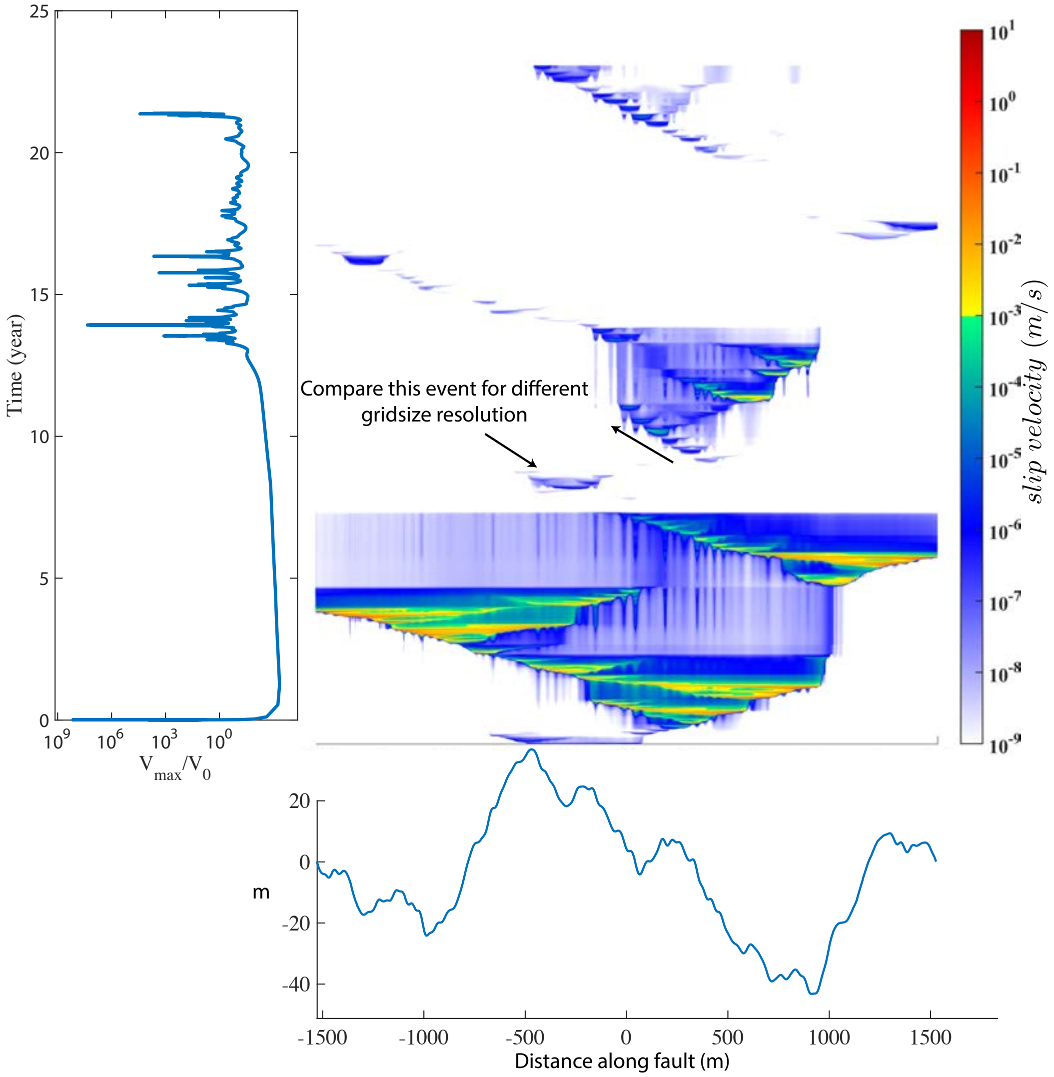

Figure 4.6 – Example of a rough fault in in-plane configuration. Here the amplitude to wavelength ratio is $\alpha = 0.01$. Compare to figure 4.5, the number of point used to discretized the fault was doubled.

2017).

4.2 Induced seismicity

4.2.1 Introduction

Induced seismicity due to waste water injection have drawn the attention since the huge rise in the number of earthquakes in mid USA (*Ellsworth*, 2013 ; *Ellsworth et al.*, 2015). The cumulative number of earthquakes in Oklahoma correlates with the increase in injection flow (*Ellsworth*, 2013). In 2014, the number of cumulated earthquake in Oklahoma outpass the cumulated number of earthquakes in California (*Hand*, 2014). This is of particular importance because Oklahoma, a state that was not known to be particularly seismically active, has experienced the two biggest earthquakes, most likely linked with fluid injection, ever recorded in the last decade, the 2011 $M_w 5.7$ Prague earthquake (*Keranen et al.*, 2013 ; *Sun and Hartzell*, 2014), and the 2016 $M_w 5.8$ Pawnee earthquake (*Barbour et al.*, 2017 ; *Yeck et al.*, 2017). However, extensive studies have shown that waste water injection does not always correlate with earthquake association (*Weingarten et al.*, 2015). Therefore understanding what are the condition under which the probability of an earthquake increase due to waste water injection is a key point in hazard management.

4.2.2 Model

Several causes have been suggested for the triggering of earthquake due to fluid injection. Fluid injection is suspected to provoke high pressure fluid migration, that reduces the effective stress on the fault. For long range interaction, poroelastically induced coulomb stress change can surpass high pore pressure diffusion transfer (*Goebel et al.*, 2017 ; *Barbour et al.*, 2017). In this model it is no possible to incorporate these effects, hence we will only model the pore pressure diffusion. In order to incorporate fluid diffusion in our model, equation 2.70 is modified :

$$\dot{\sigma}_n = \underbrace{\int_{faults} K^n(s,\xi)\frac{\partial}{\partial \xi}V \mathrm{d}\xi}_{\text{normal traction}} + \underbrace{\dot{\tau}_n^{load}}_{\text{normal loading}} + \underbrace{\dot{P}}_{\text{pressure rate}} \tag{4.5}$$

The conservation of fluid mass is

$$\frac{\partial m}{\partial t} + \nabla q_f = 0 \tag{4.6}$$

Where m is the mass of fluid, and q_f if the fluid flux. The fluid flux follows Darcy's law :

$$q_f = -\frac{\rho k}{\eta}\nabla P \tag{4.7}$$

Where k is the permeability of the medium, η is the viscosity of the fluid and ρ is the fluid density. Here the permeability is assumed to be constant and isotropic. The rate of change of mass is :

$$\begin{aligned}\frac{\partial m}{\partial t} &= \frac{\partial \rho\phi}{\partial t}\\ &= \phi\frac{\partial \rho}{\partial t} + \rho\frac{\partial \phi}{\partial t}\\ &= \rho\phi\left(\frac{1}{\rho}\frac{\partial \rho}{\partial P} + \frac{1}{\phi}\frac{\partial \phi}{\partial P}\right)\frac{\partial P}{\partial t}\\ &= \rho\phi\left(\beta_f + \beta_\phi\right)\frac{\partial P}{\partial t}\end{aligned} \tag{4.8}$$

Where ϕ is the porosity of the rock. β_f and β_ϕ are respectively the fluid compressibility and the pore space pressure expansivity. Using equation 4.6 together with equation 4.8 we get (*Bodvarsson*, 1970 ; *Segall and Rice*, 1995) :

$$\frac{\partial P}{\partial t} - \frac{k}{\eta\phi(\beta_f + \beta_\phi)}\nabla^2 P = 0 \tag{4.9}$$

This is a diffusion equation without any source term. If we considered a continuous point source solution, we can obtain an analytical solution (*Carslaw and Jaeger*, 1959, p 261) :

$$P = \frac{\dot{P}_{well}}{4\pi D r}\text{erfc}\left(\frac{r}{2\sqrt{Dt}}\right) \tag{4.10}$$

Where $\dot{P}_{well}$ is the pressure rate at the injection well and D is the diffusion coefficient.

$$D = \frac{k}{\eta\phi(\beta_f + \beta_\phi)} \tag{4.11}$$

erfc is the complementary error function given by :

$$\text{erfc}(x) = \frac{2}{\sqrt{\pi}}\int_x^\infty \text{e}^{-t^2}\text{d}t \tag{4.12}$$

The derivative gives the pressure rate in equation (4.5) :

$$\dot{P} = \frac{\dot{P}_{well}}{(4\pi D r)^{\frac{3}{2}}}\,\text{exp}\left(-\frac{r^2}{4Dt}\right) \tag{4.13}$$

Name	symbol	Value
Pore space pressure expansivity[1]	β_ϕ	10^{-9} Pa^{-1}
Fluid compressibility[1]	β_f	10^{-9} Pa^{-1}
Porosity[1]	ϕ	10^{-2}
Dynamic viscosity	η	10^{-3} Pa.s
Permeability	k	$2 \times 10^{-16} - 2 \times 10^{-17}$ m^2
Resulting diffusivity[2,3]	D	$0.01 - 0.001$ m^2/s
Injection rate[2,3]	Q	1000 m^3/month
Injection duration	Δt	1 year

Table 4.2 – Parameters of the fluid injection simulation. The values are order of magnitude that are extracted from 1 *Rice* (2006), 2 *Keranen et al.* (2013) and 3 *Goebel et al.* (2017). The diffusion coefficient is closer from the laboratory derived than from the seismicity migration (*Shapiro et al.*, 1997 ; *Goebel et al.*, 2017).

Using equation 4.8, it is possible to link the injection rate with the pressure rate at the well :

$$\dot{P}_{well} = \frac{Q}{\phi(\beta_f + \beta_\phi)} \tag{4.14}$$

Where Q is the injection rate in m^3/s at the well. Finally equation (4.10) can be written :

$$P = \frac{Q\eta}{4\pi kr}\text{erfc}\left(\frac{r}{2\sqrt{Dt}}\right) \tag{4.15}$$

To model the shut-in of a well, we can use the linearity of the solution of the diffusion equation and finally add a well at the same location but with a negative injection rate $-Q$:

$$\begin{aligned} P = \frac{Q\eta}{4\pi kr}\Bigg[&\text{erfc}\left(\frac{r}{2\sqrt{D(t-t_{beg})}}\right)\mathcal{H}(t-t_{beg}) - \\ &\text{erfc}\left(\frac{r}{2\sqrt{D(t-t_{end})}}\right)\mathcal{H}(t-t_{end})\Bigg] \end{aligned} \tag{4.16}$$

Where t_{beg} and t_{end} are respectively the beginning and the end of the injection. $\mathcal{H}$ is the Heaviside function.

4.2.3 Fluid injection during earthquake cycle

In this section, we ran 3 simulations with different position of the injection well. In each of the simulation, the parameters used can be found in table 4.2. The injection starts when the seismic cycle is stable over two cycles, and lasts only one year. Figures 4.7, 4.8 and 4.9 are done with a diffusivity of $D = 0.01$ m^2/s and figures 4.10, 4.11 and 4.12 with a diffusivity of $D = 0.001$ m^2/s. Somehow counterintuitive, in all these simulations, the next earthquake after injection is postponed. For all these simulations, after the shut in, the periodicity is recovered after some cycles. For lower diffusivity (Fig. 4.10, 4.11 and 4.12), it takes more time for the seismic cycle to recover the classic single fault seismic cycles.

4.2.4 Conclusion

From this small subset of simulation, it is not possible to draw general conclusions about fluid injection. However, this already allows us to answer partially some questions : in this restricted parameter space the next earthquake directly following injection was always postponed (except maybe in Fig. 4.10, but it was a slow event), making possible that in some specific areas injection of fluid would delay instead of advancing the next earthquake. The injection can in some case lead to emergence of slow events (Fig. 4.11 and Fig. 4.10). This effect was already observed in an experiment in south east France, where aseismic slip was triggered on a fault by injection of fluid (*Guglielmi et al.*, 2015). This is probably an effect of reduce effective normal stress that increase the nucleation lenghscale and hence prone slow events.

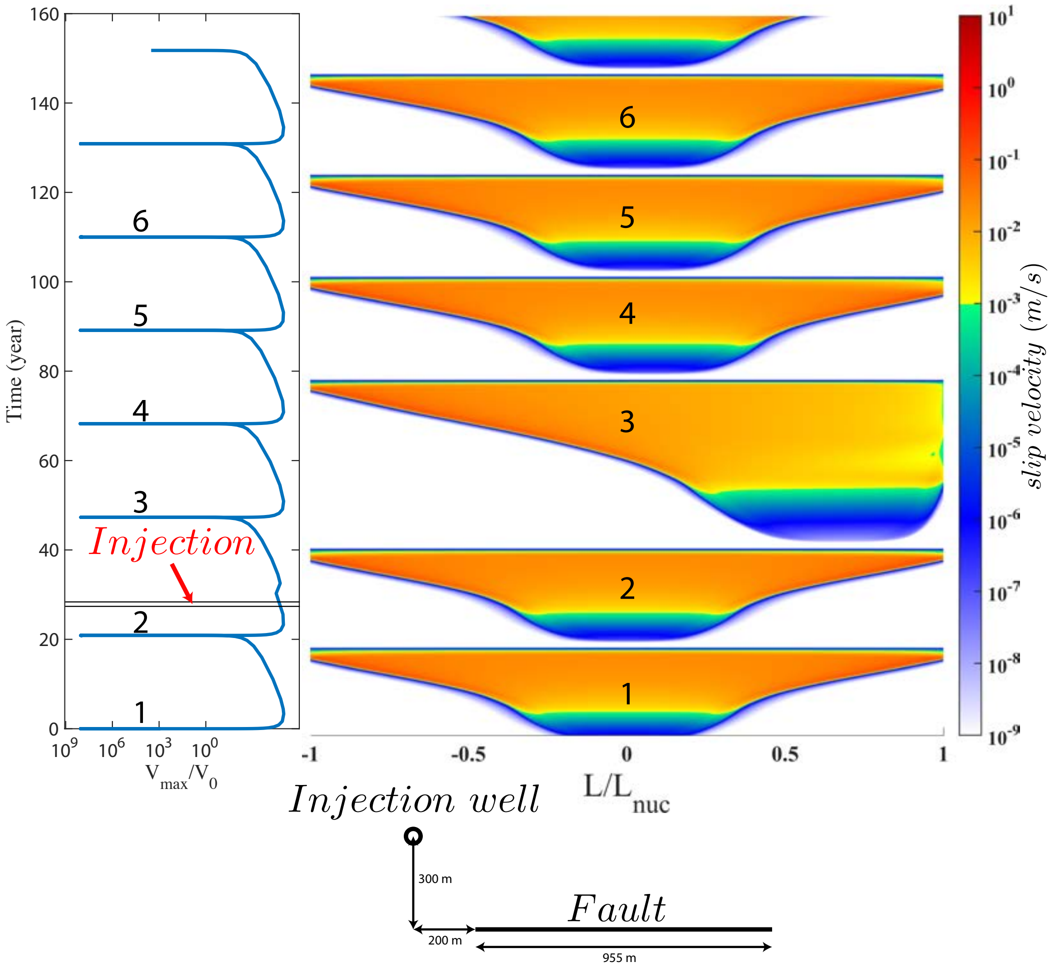

Figure 4.7 – Example of a fluid injection modeled by pore pressure diffusion, with a diffusivity $D = 0.01$ m^2/s.

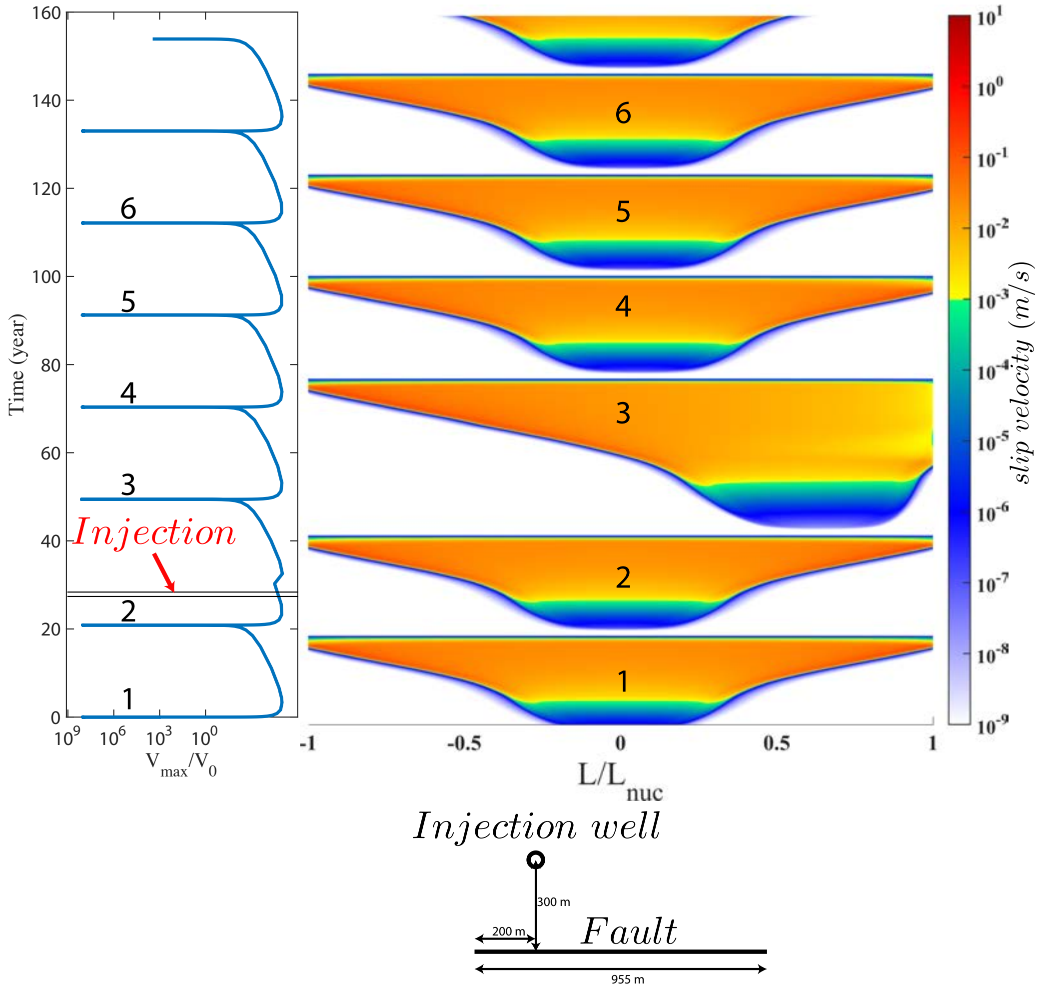

Figure 4.8 – Example of a fluid injection modeled by pore pressure diffusion, with a diffusivity $D = 0.01$ m$^2/$s.

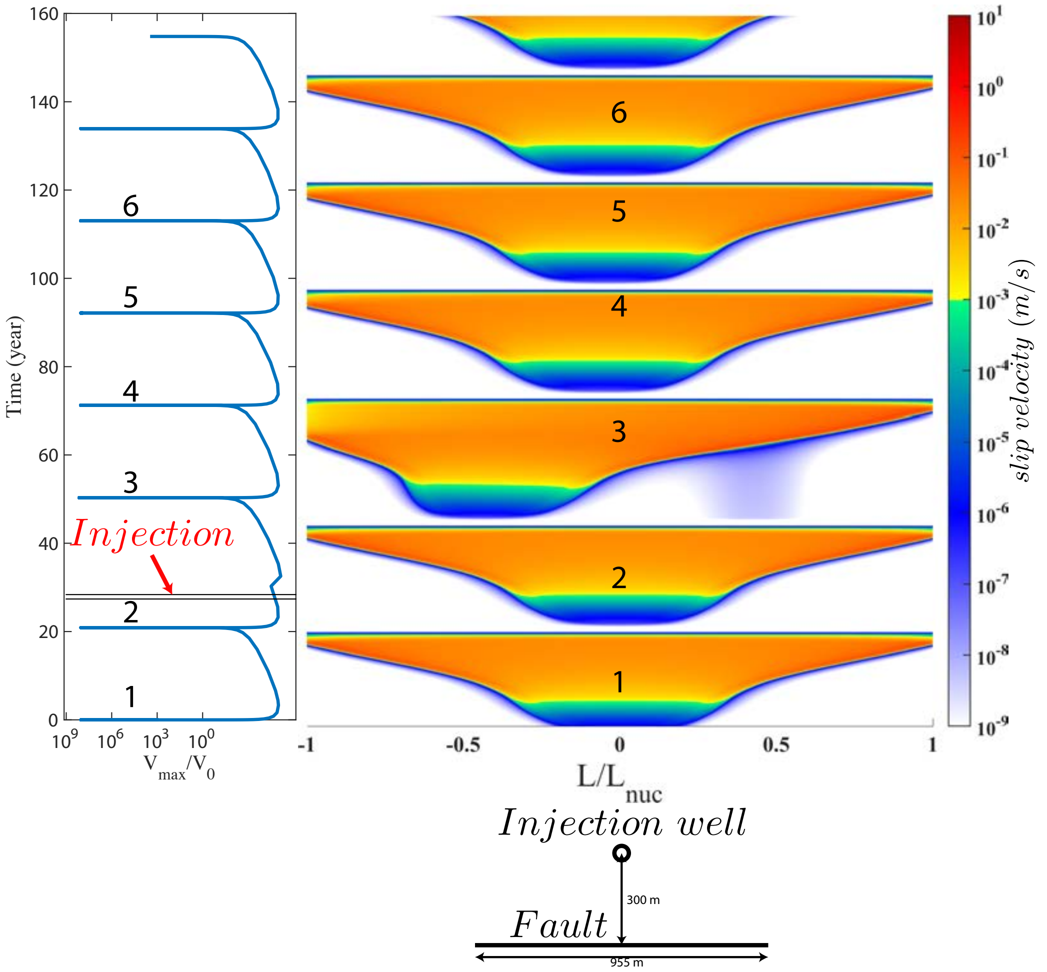

Figure 4.9 – Example of a fluid injection modeled by pore pressure diffusion, with a diffusivity $D = 0.01$ m^2/s.

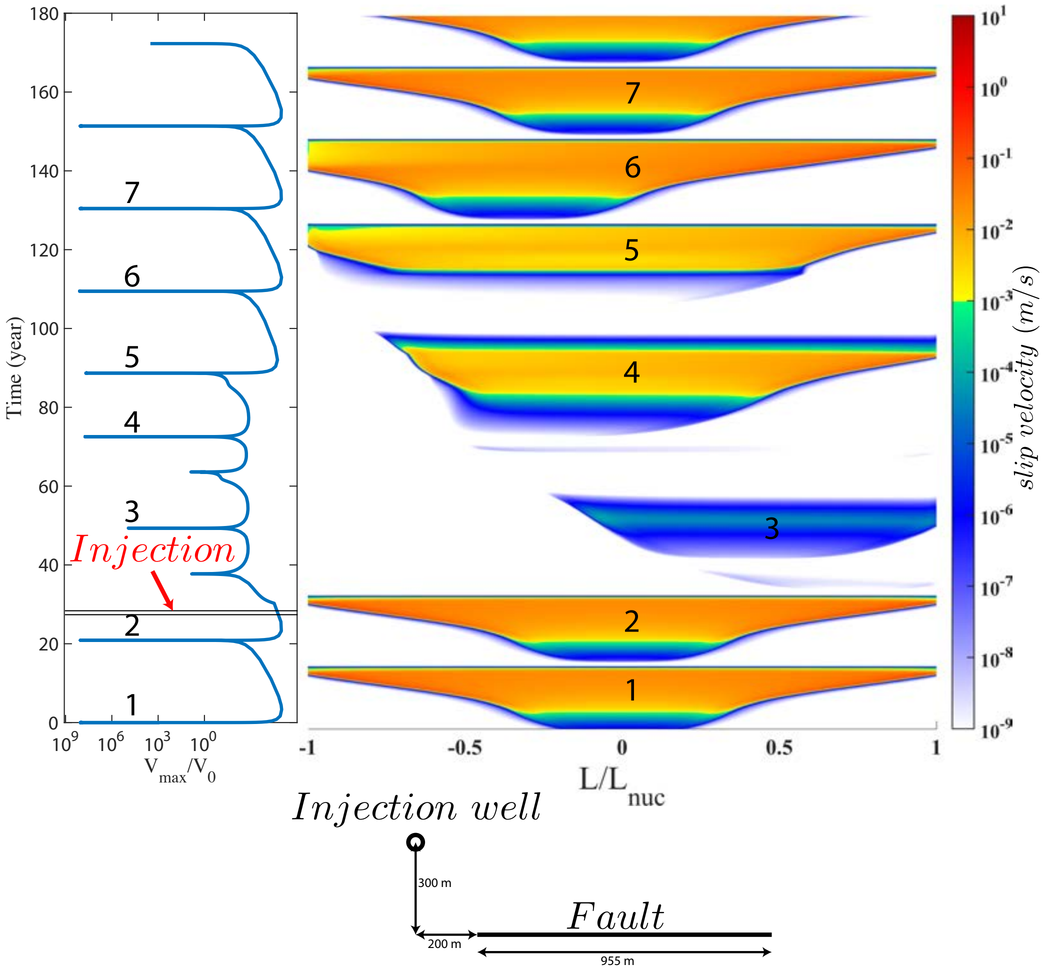

Figure 4.10 – Example of a fluid injection modeled by pore pressure diffusion, with a diffusivity $D = 0.001$ m^2/s.

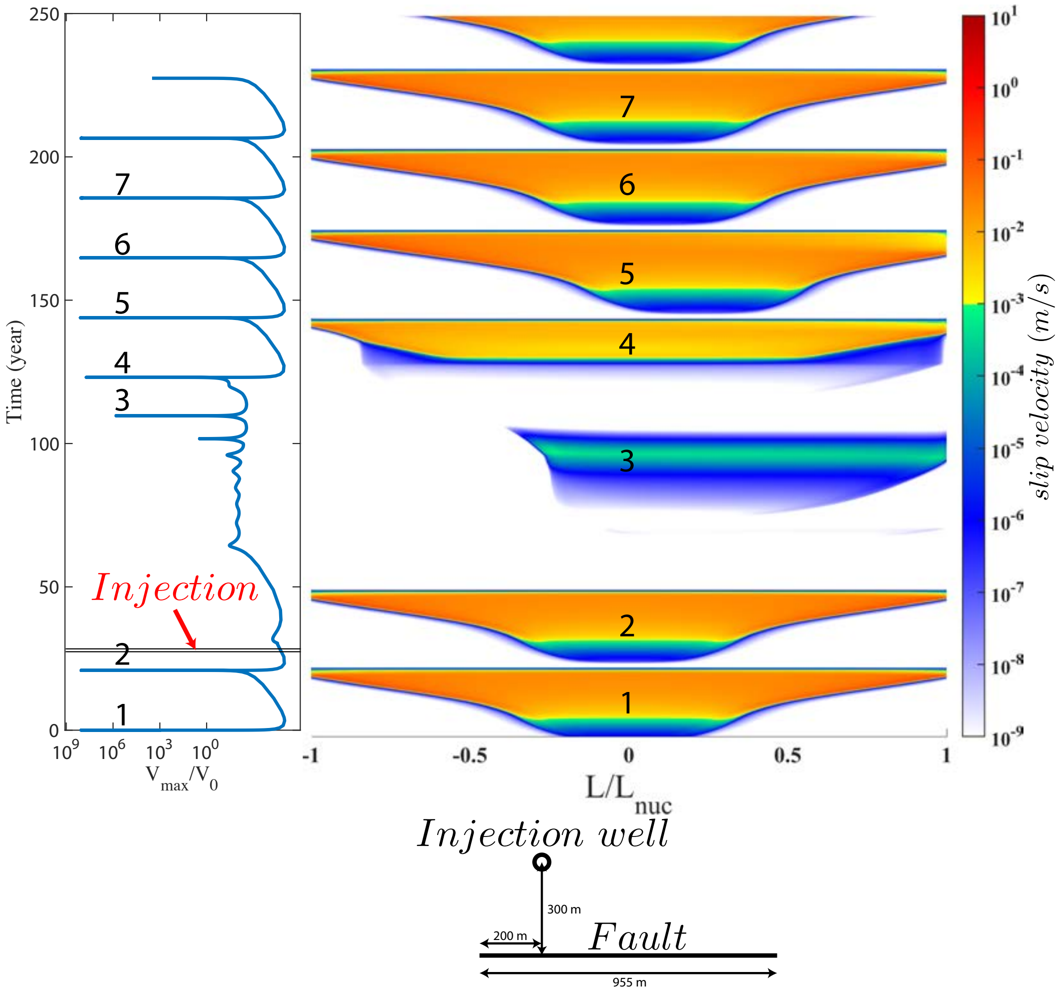

Figure 4.11 – Example of a fluid injection modeled by pore pressure diffusion, with a diffusivity $D = 0.001$ m^2/s.

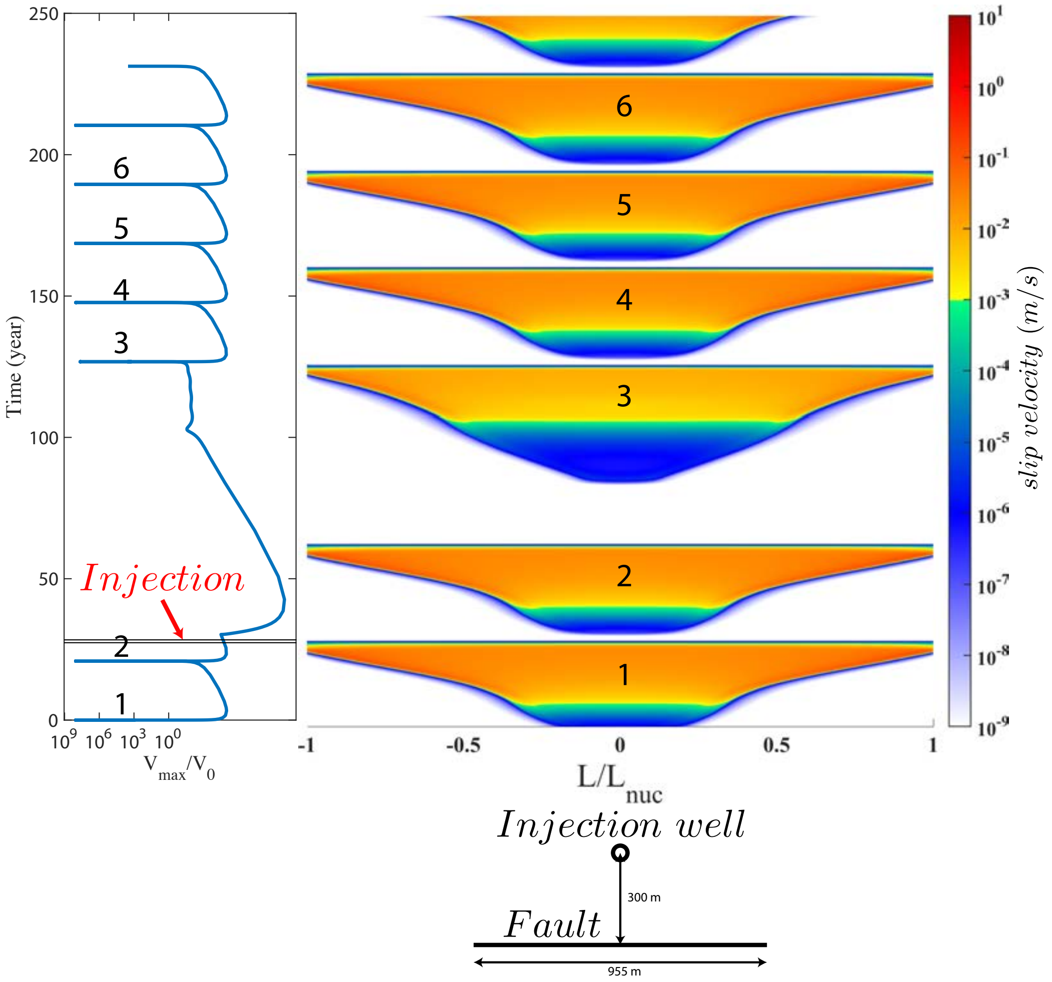

Figure 4.12 – Example of a fluid injection modeled by pore pressure diffusion, with a diffusivity $D = 0.001$ m^2/s.

4.3 Real geometry of fault network

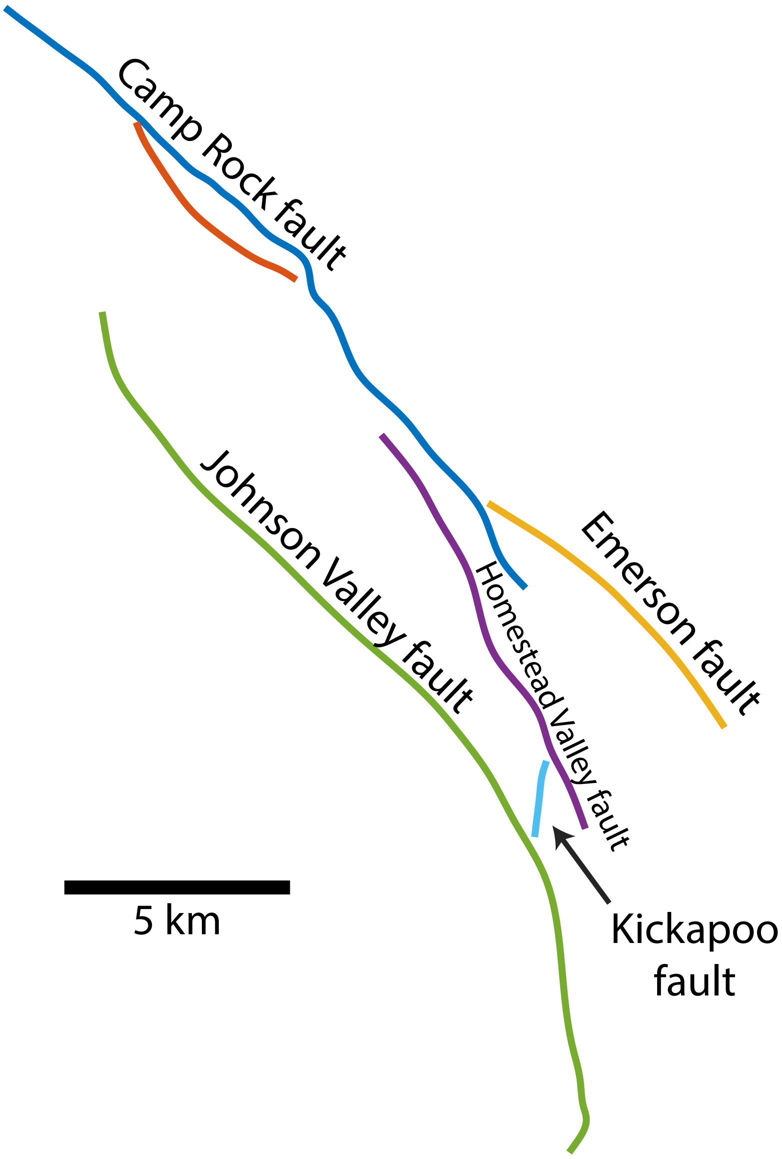

Figure 4.13 – Landers fault surface map of the geometry used for the simulation.

In this section, the Landers geometry fault surface map is used to run simulations of earthquake cycle. We will considered three different scenarios, where the initial nucleation will happen on the different faults. For these simulations, the constant parameters are given in table 4.3. This section aims at demonstrating that complexities of fault systems can simply emerge from geometrical consideration without tuning any rheological parameters. The

Name	symbol	Value
Reference friction coefficient	f_0	0.6
Reference velocity	V_0	10^{-9} m/s
Critical slip distance	D_c	5 mm
Rate and state parameter	a	0.008
Rate and state parameter	b	0.01
Shear rate loading	$\dot{\tau}_t$	0.01 Pa/s
Normal stress	σ_n	100 MPa
Shear modulus	μ	30GPa
Shear velocity	c_s	3000 m/s
Dilatational velocity	c_p	5000 m/s
Resulting nucleation length scale	L_{nuc}	3.183km

Table 4.3 – Table of constant parameters among all the simulation shown in this section.

nucleation length scale here is chosen such that most of the fault (except Kickapoo fault) must be able to rupture dynamically.

4.3.1 Scenario 1 : initial nucleation on Camp Rock fault

In this scenario the first earthquake is artificially nucleated on Camp Rock fault by increasing the velocity on a small portion of the fault. We then leave the simulation run for 800 years. The fact that the geometry is fixed, inevitably leads to a accumulation or a reduction on some parts of the fault of normal stress (Fig. 4.14). This makes some parts of the fault completely blocked after a few seismic cycles. Particularly at kinks (see the kink on Camp Rock fault in figure 4.14). Figure 4.16 and 4.17 show a sequence of event that begins in year 406 after the beginning of the simulation. This sequence initiated on Camp rock Fault with a slow event, and then rupture Johnson valley and Kickapoo fault two years later. Emerson fault ruptures in year 414, and finally one half of the Johnson Valley fault is ruptured in year 418. The other half of the Johnson valley fault ruptured 9 years after. Although the timing of events is difficult to interpret because we are doing an oversimplified model (2D quasidynamic model), the sequence of events is particularly interesting. The sequence involves all the faults, and shows partial rupture on the fault

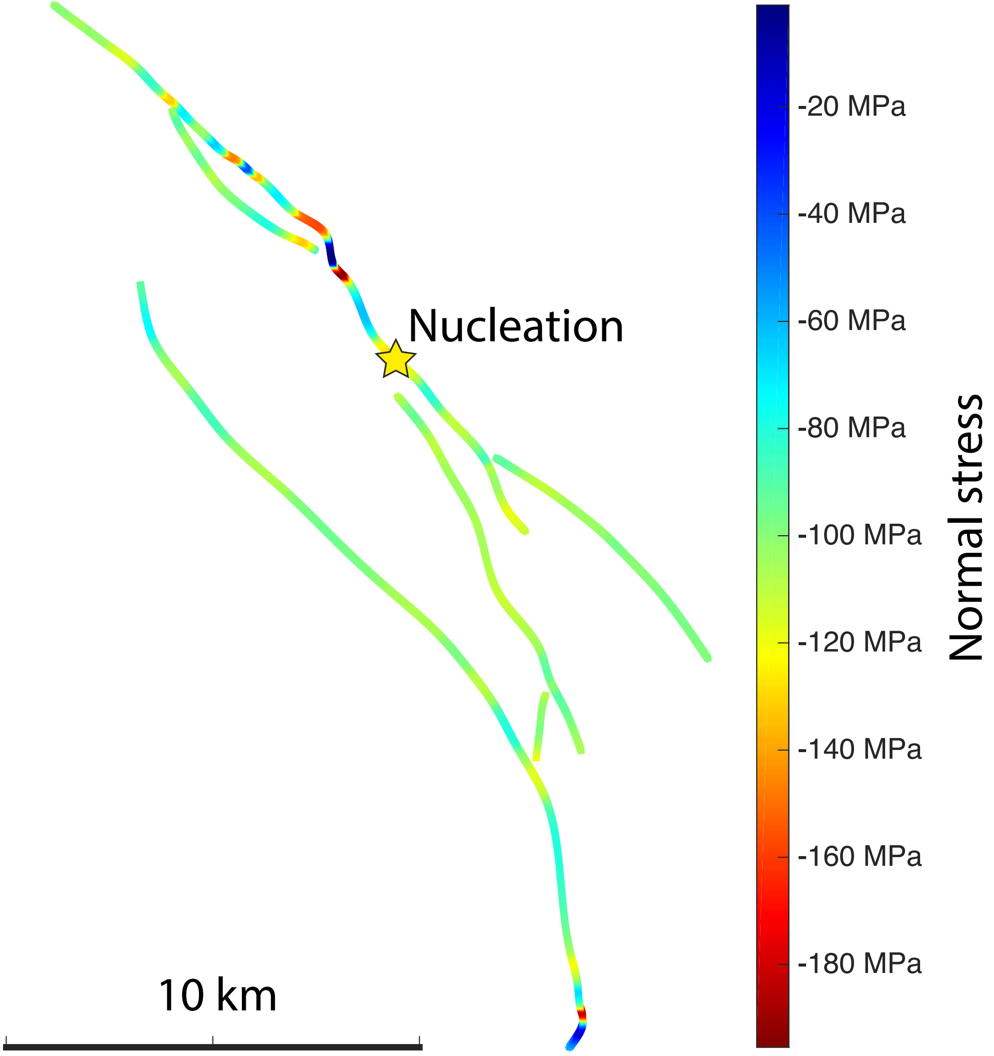

Figure 4.14 – Landers fault surface map with the evolution of normal stress at time $= 411$ years

at location of geometrical complexities (kink on Camp Rock fault, branch of Kickapoo fault and Johnson Valley fault). The fact that it is not rupturing in only one time may be due to the resolution of our branch. Indeed, the different branch are well separated from each other. Another explanation, or a complementary phenomenon is that these simulations are quasi dynamic simulation. It was shown that for quasi dynamic simulation, it is harder for a rupture to go through an asperity of rate strengthening than for a fully dynamic rupture (*Thomas et al.*, 2014). This is probably also the case here though the velocity strengthening is infinitely rate strengthening (because our faults are finite).

Something that is also obvious from this sequence is that most of the slow events initiate close to geometrical complexities. This is maybe an hint that the creep burst observed by *Jolivet et al.* (2013) on Haiyuan fault close to a fault overlap was not a coincidence. If we now look at the cumulative number of earthquake, it is surprising that all the events are clustered in time (Fig. 4.15).

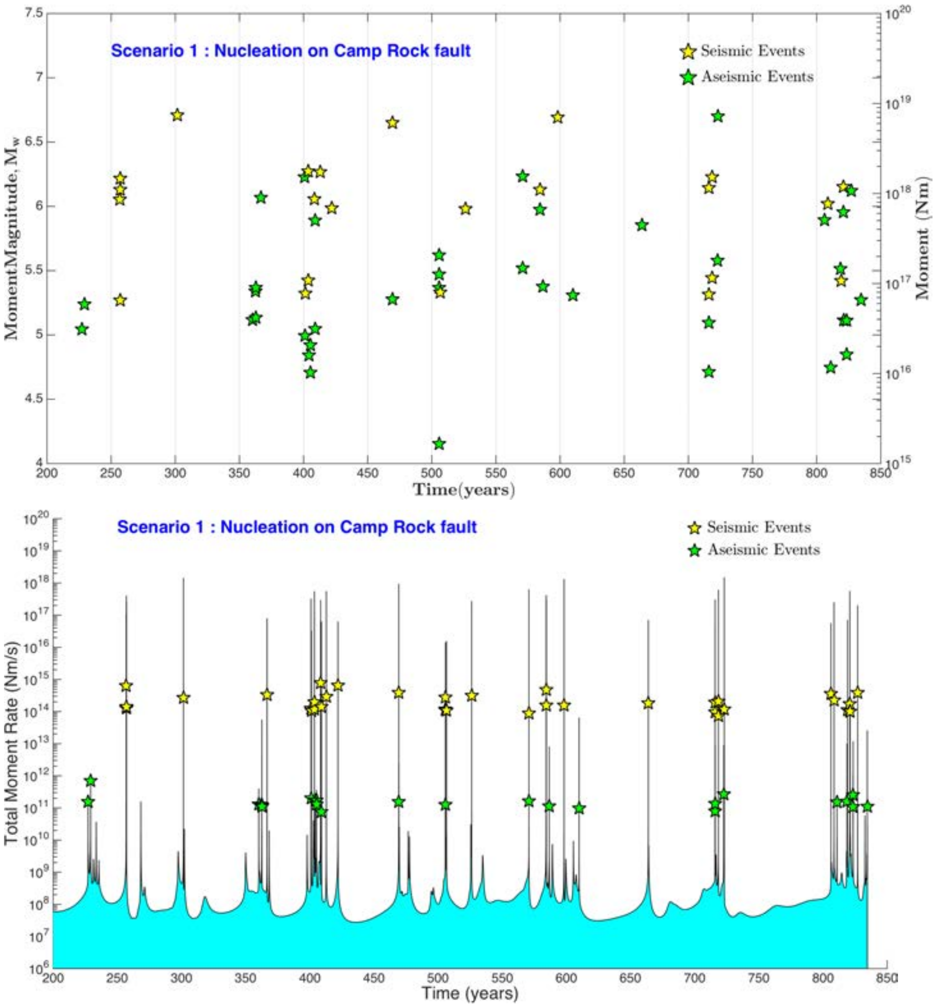

Figure 4.15 – Scenario 1 : moment and moment rate versus time. Events are clustering in time.

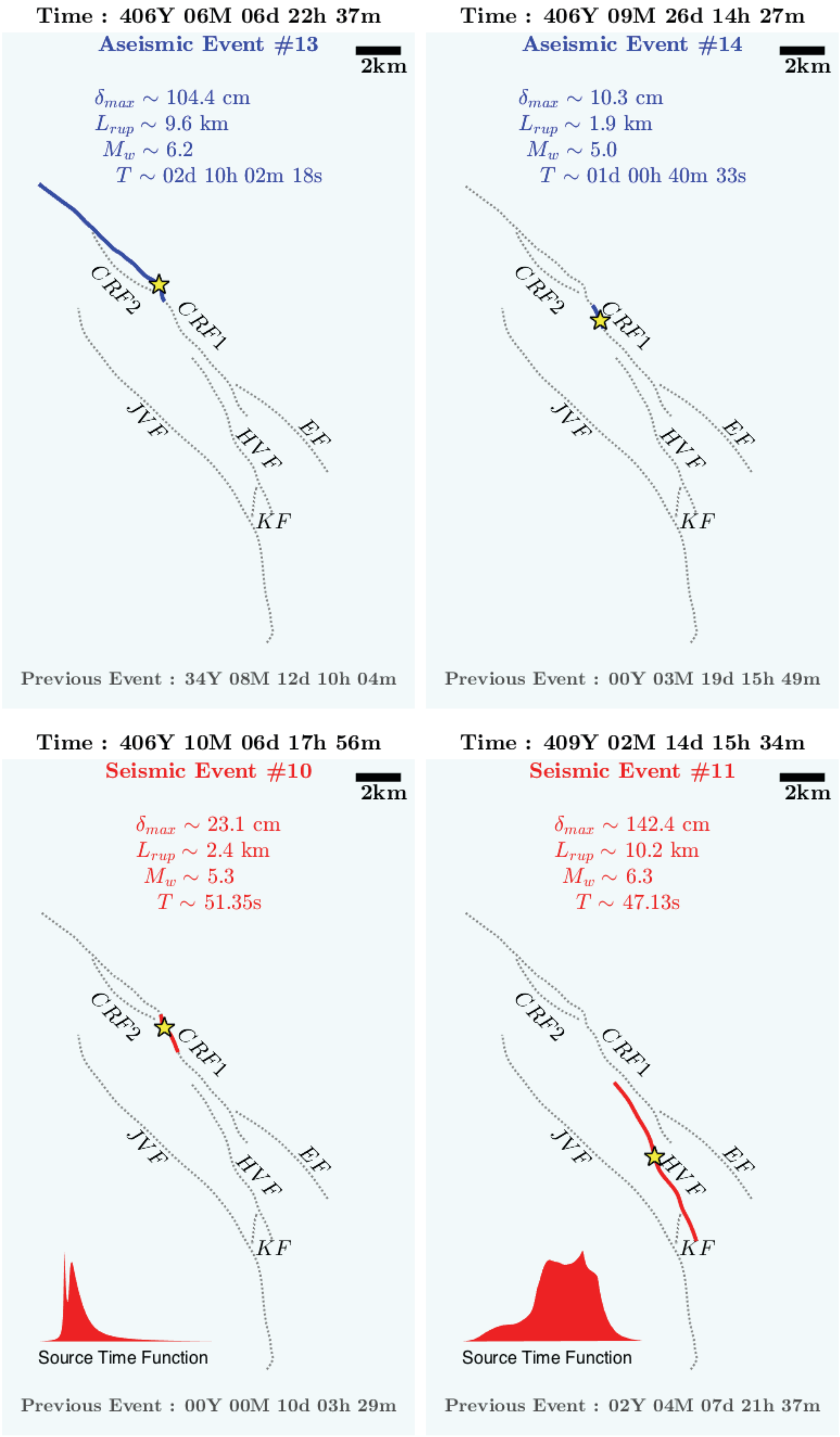

Figure 4.16 – Scenario 1 : sequence of clustered events.

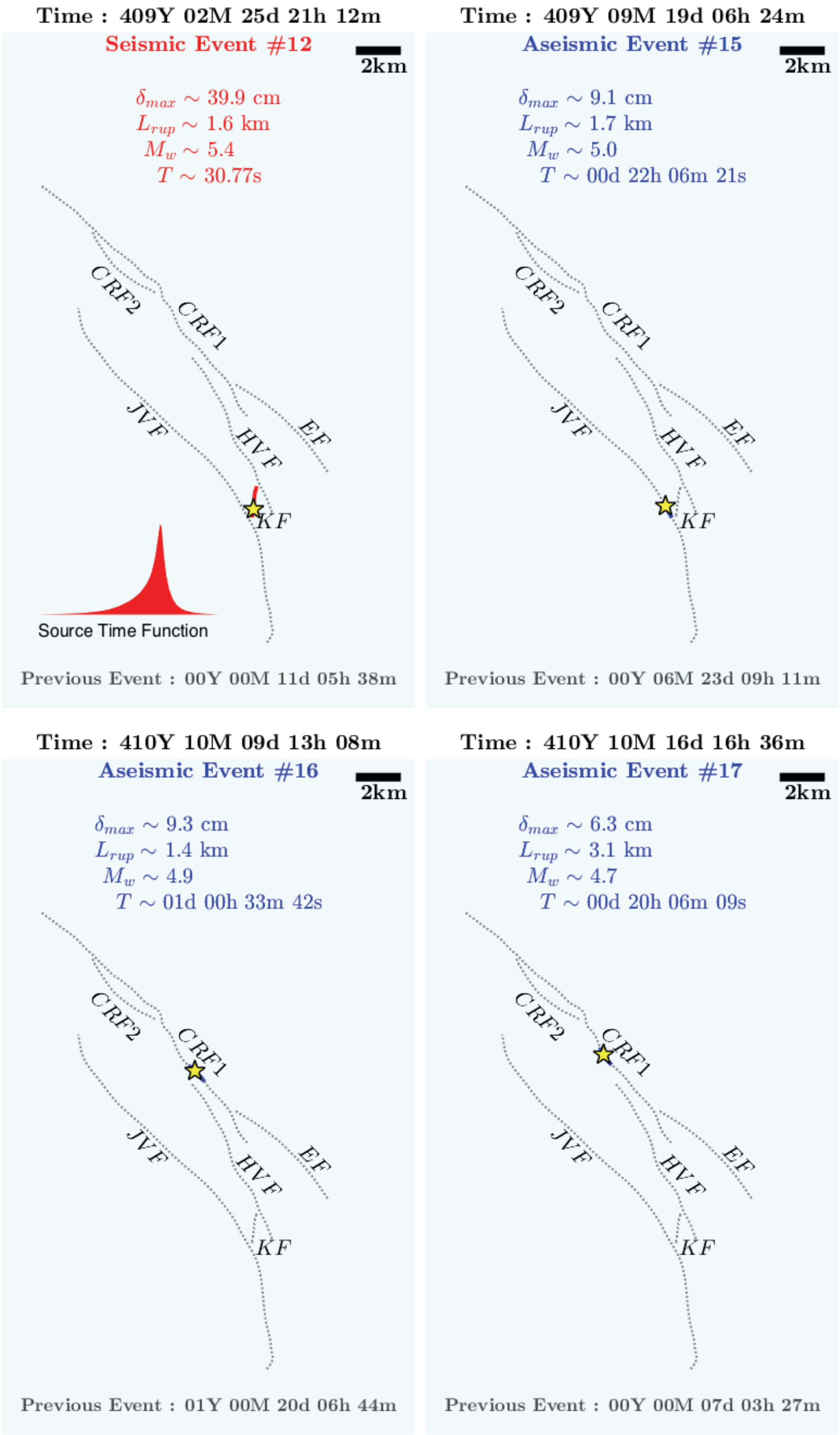

Figure 4.17 – Scenario 1 : sequel of figure 4.16, sequence of clustered events.

4.3.2 Scenario 2 : initial nucleation on Homestead Valley Fault

In this scenario the first initial event was artificially triggered on Homestead valley fault by introducing a perturbation in sliding velocity on the fault. The sequence shown here begins 675 years after the beginning of the simulation by a dynamic rupture on Emerson fault (Fig. 4.19 and 4.20). One month later a subsequent partial rupture happen on Camp Rock Fault. The same remarks as for the scenario 1 holds here : it seems that slow events are emerging close to geometrical asperities, and that earthquakes are clustering, although it happens that some fault ruptures alone (Johnson Valley Fault at year 500, Fig. 4.18).

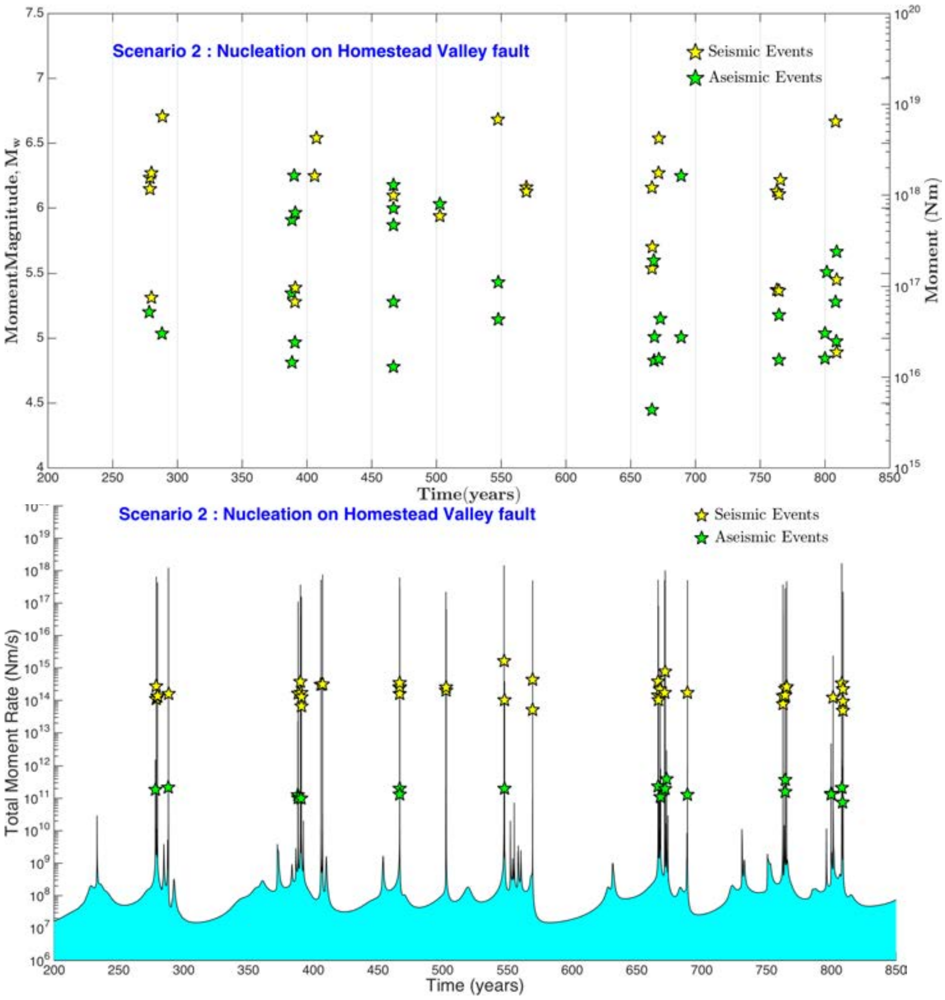

Figure 4.18 – Scenario 2 : moment and moment rate versus time. Events are clustering in time.

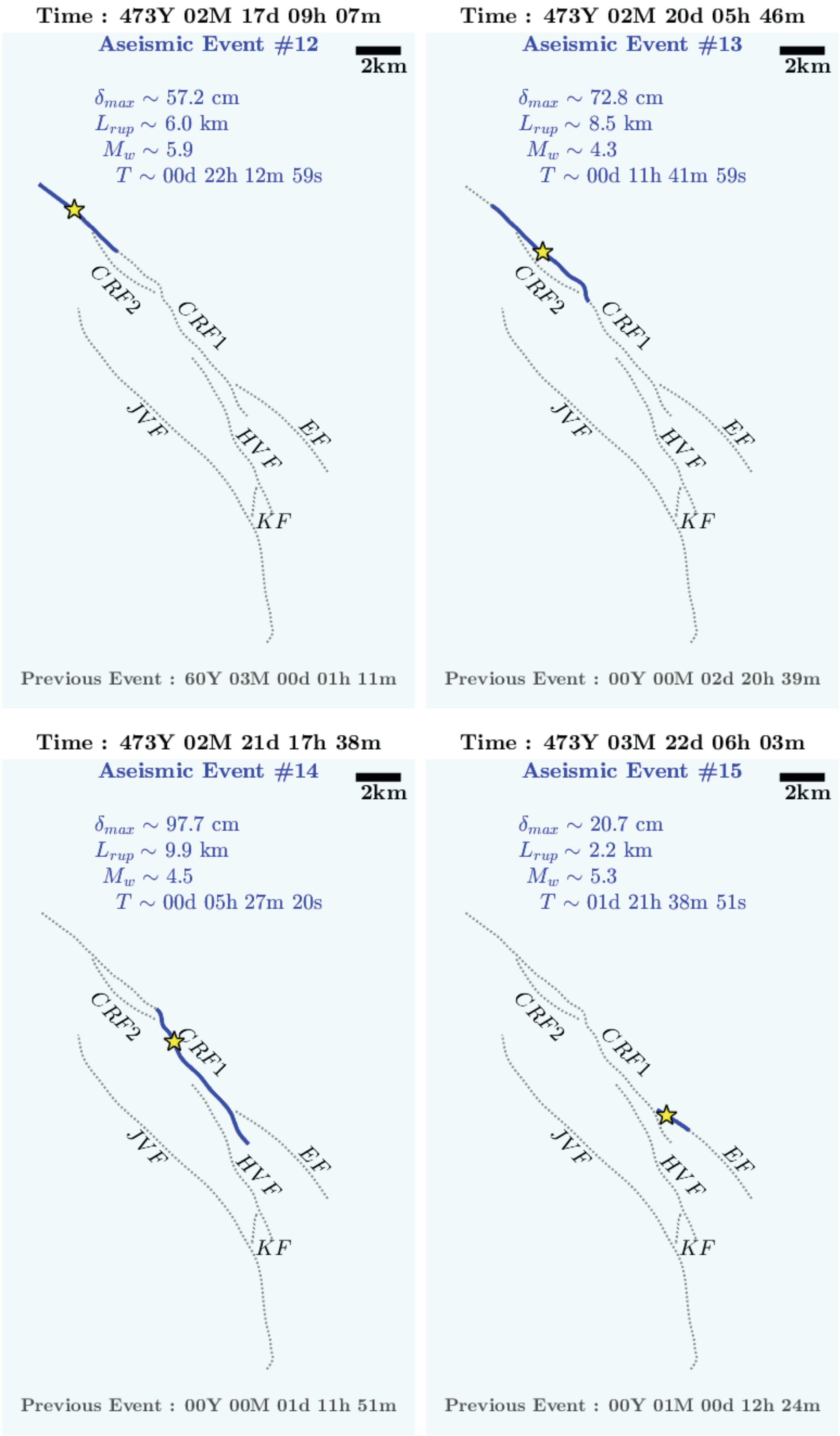

Figure 4.19 – Scenario 2 : sequence of clustered events.

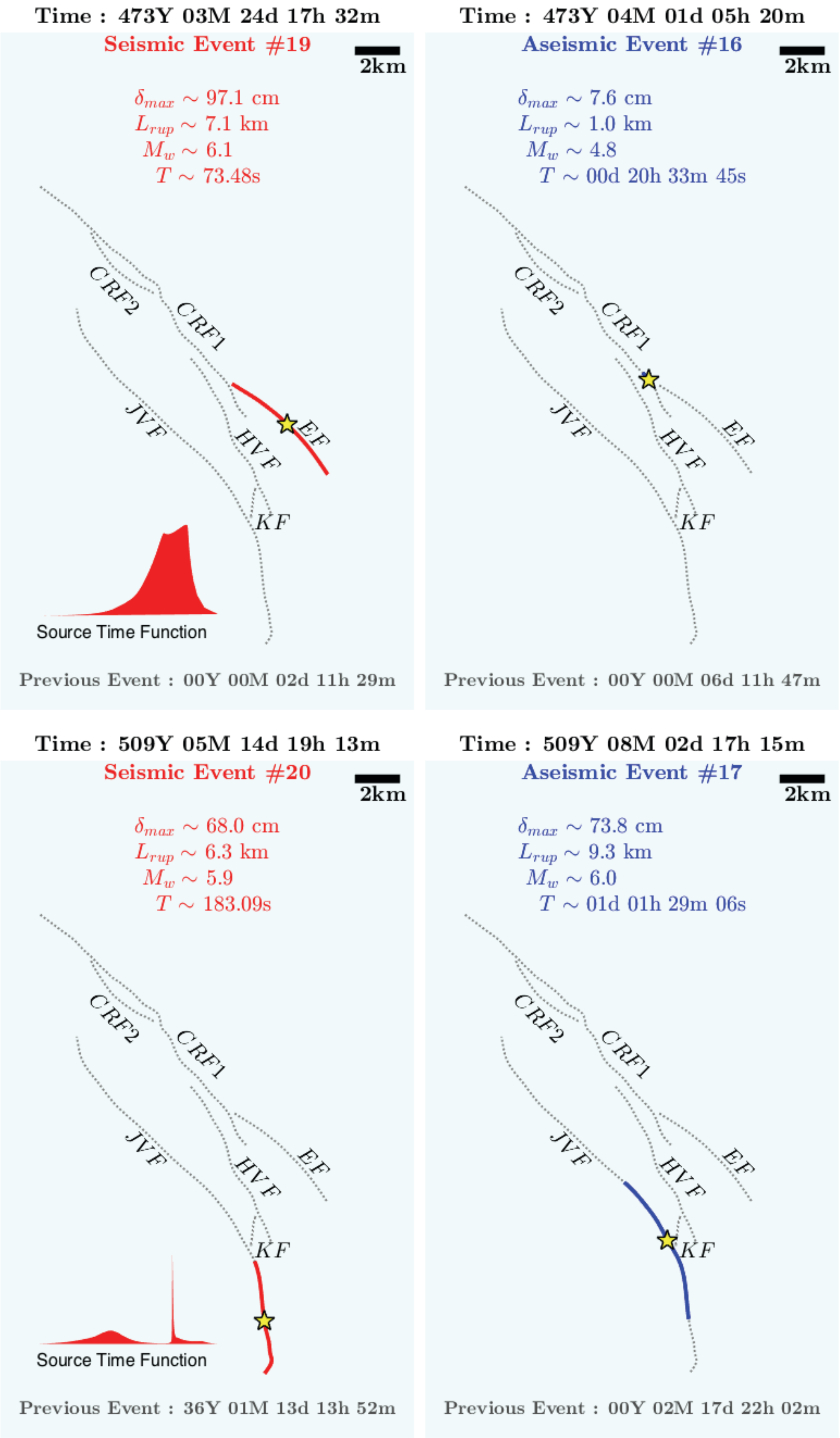

Figure 4.20 – Scenario 2 : sequel of figure 4.19, sequence of clustered events.

4.3.3 Scenario 3 : initial nucleation on Johnson Valley Fault

In the last scenario the first initial event is again artificially triggered on Johnson valley fault by introducing a perturbation in sliding velocity on the fault. Like the two other scenarios, events are clustering in time (Fig. 4.21). In this last scenario, we show a sequence that begins with a slow rupture on Camp Rock fault 420 years after the beginning of the simulation (Fig. 4.22 and 4.23).

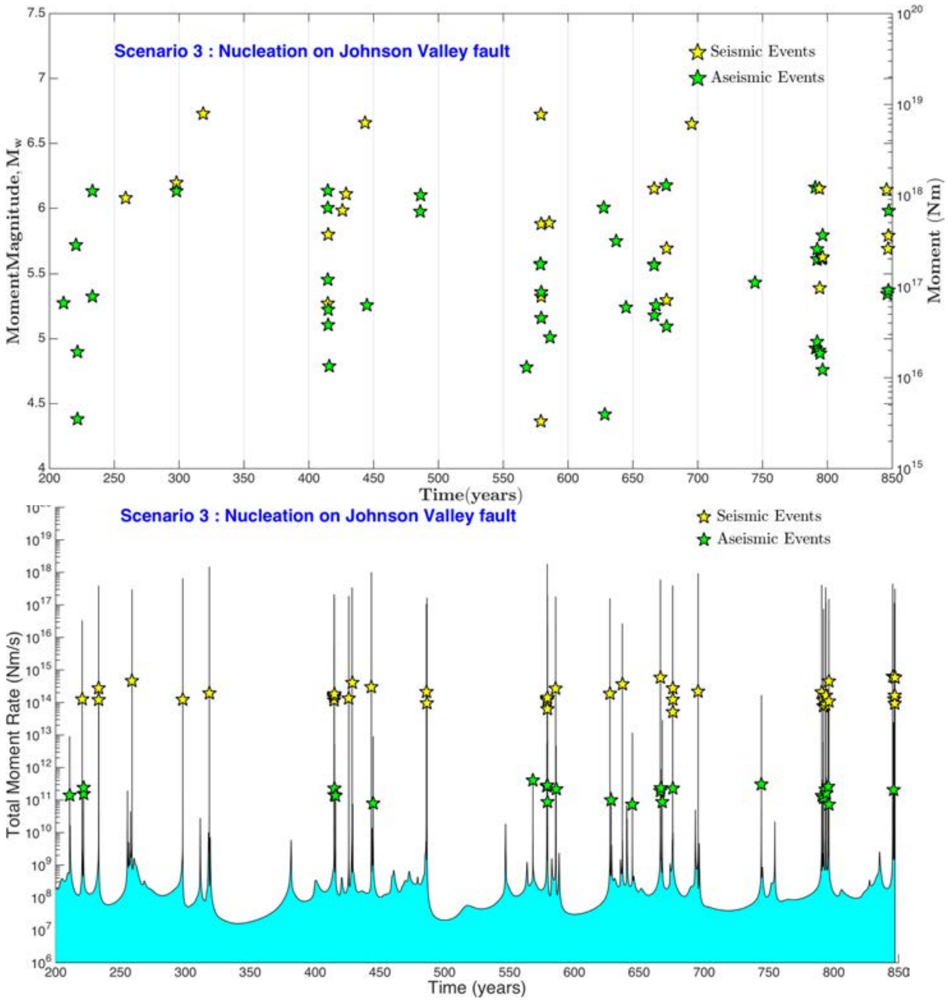

Figure 4.21 – Scenario 3 : moment and moment rate versus time. Events are clustering in time.

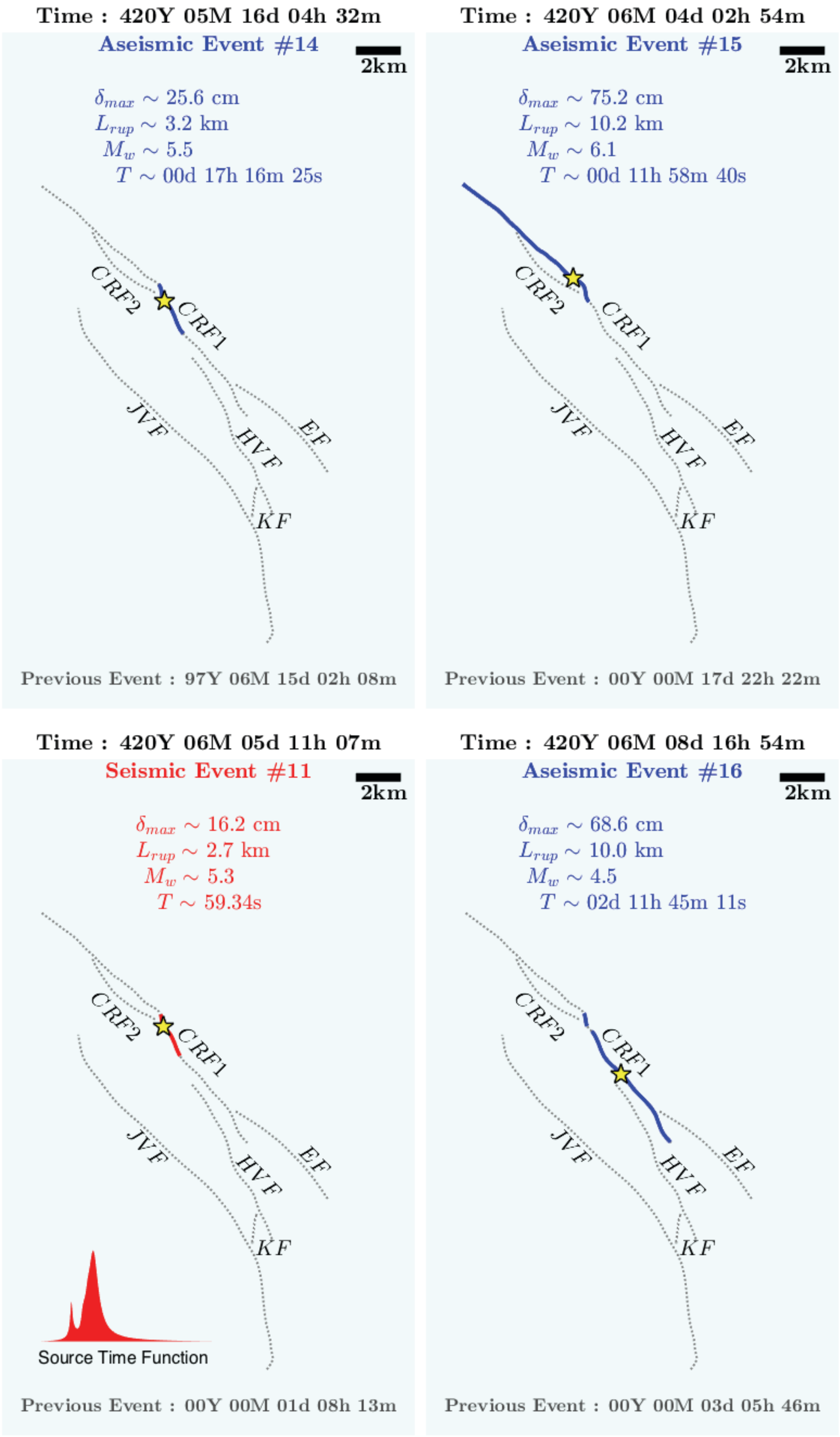

Figure 4.22 – Scenario 3 : sequence of clustered events.

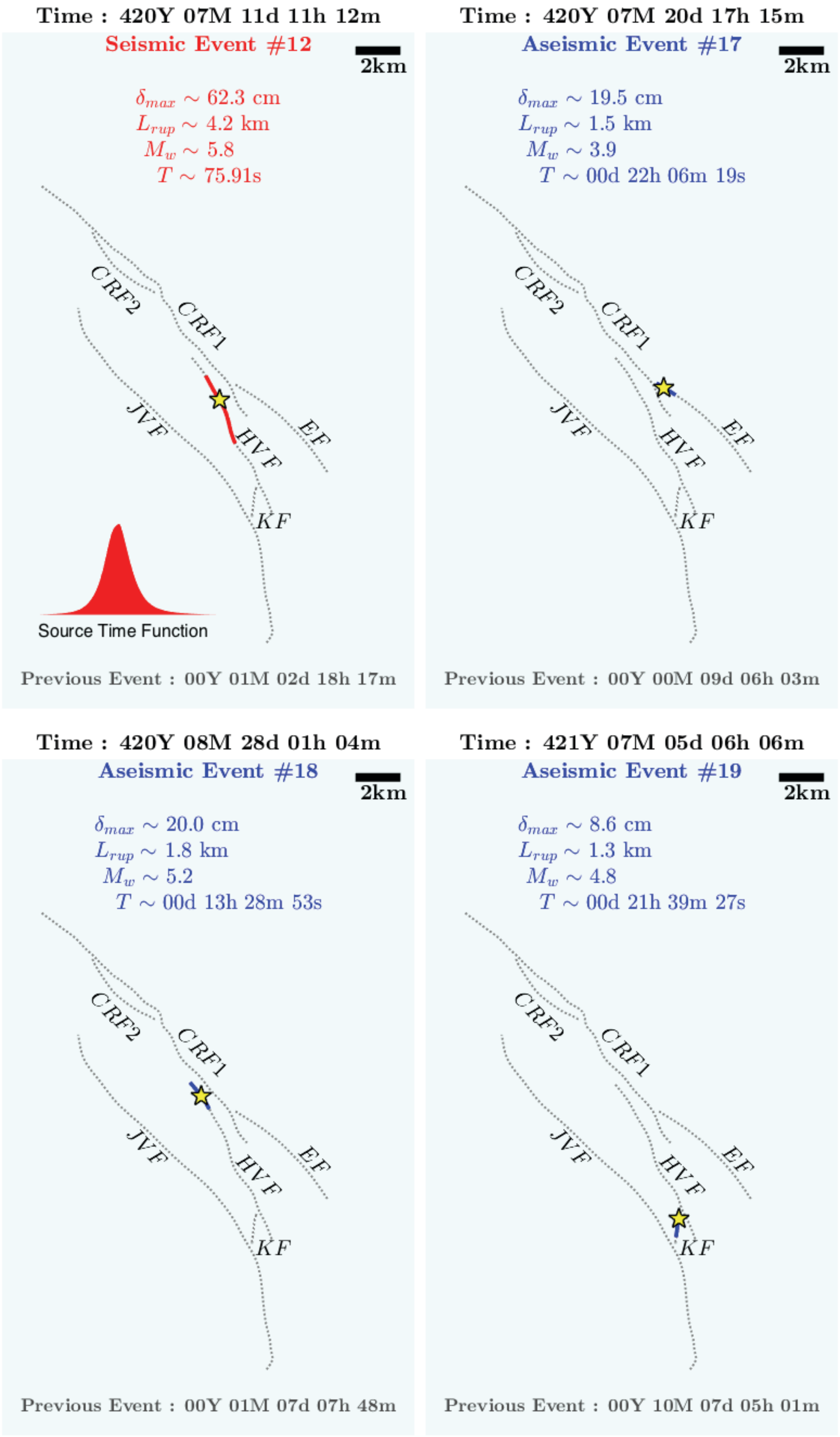

Figure 4.23 – Scenario 3 : sequel of figure 4.22, sequence of clustered events.

4.3.4 Discussion and conclusion

In this section, we showed three different simulations of the seismic cycle of Eastern California Shear Zone. The geometry of faults used here is smooth and not rough. However we tried to take into account the true geometry of these faults, based on fault mapping. In this system, despite the fact that most of the faults are longer than the nucleation length scale, complex dynamics including slow and fast events emerge. We saw that these slow events seem to emerge close to geometrical complexities for all the three different simulations. An other general comment is the apparent clustering of all the events in the three simulations. This clustering of event, the trend of fault to synchronise themselves was already observed in mode III for the two overlapping fault system in Chapter 3, even when the distance between them was twice as large than the length of the faults. The clustering of big earthquakes is supported by paleoseismological studies in this area (*Rockwell et al.*, 2000 ; *Ganev et al.*, 2010). The rupture pattern of these different clusters is not identical and varies in time. This state was already identified by *Scholz* (2010) and named by him, *fuzzy synchrony*. This is only preliminary work (mainly to demonstrate the power of the new algorithms developed in this thesis), but in the future this kind of model can be used to build statistics of potential rupture of faults. It would be interesting to know for example, in a given system of faults, which faults are more likely to rupture together ? What is the fault that is rupturing the most ? Is the clustering of events a reality ? For large number of cycles, is there one pattern of rupture that is repeating ? These are the kind of questions that can now be addressed with full physics based models and will be in explored in the future.

Chapitre 5

Conclusion

5.1 Conclusion

Dans cette thèse nous avons exploré ce que pouvait donner l'introduction de complexités géométriques (réseau de faille, géométrie non-plane, rugosité) dans un modèle quasi-dynamic du cycle sismique, avec une loi de friction de type ”rate-and-state”. Cela n'avait que peu été exploré jusqu'à maintenant, principalement à cause du temps de calcul de la réponse statique d'une faille dû au glissement sur celle-ci. Pour surmonter ce problème du temps de calcul, nous avons fait appel à deux méthodes développées récemment : la méthode multipolaire rapide et les matrices hiérarchiques. Ces deux méthodes accélèrent le temps de calcul du produit matrice-vecteur qui apparait lorsque l'on discrétise l'équation intégrale de frontière (cette équation donne la solution analytique des contraintes sur une faille dues au glissement, voir chapitre II). La méthode multipolaire rapide présente l'avantage d'avoir un contrôle facile et totale de l'erreur. Cependant elle nécessite le développement du noyau de l'équation intégrale de frontière, ce qui la rend dépendante de ce même noyau et difficile à mettre en oeuvre lorsque ce noyau ne présente pas une forme simple à développer en série de Taylor. C'est pourquoi dans cette thèse, l'utilisation de la méthode multipolaire rapide est restée limitée au cas ”out-of-plane”, où le noyau avait déjà développé dans le contexte du champ électrostatique créé par des charges ponctuelles (*Greengard and Rokhlin*, 1987 ; *Carrier et al.*, 1988). Les matrices hiérarchiques ne nécessitent pas de développer le noyau et sont donc utilisables dans un plus large contexte. Une collaboration avec Stéphanie Chaillat (ENSTA) en avril 2017, nous a permis de mettre rapidement en place les matrices hiérarchiques dans notre modèle (*Desiderio*, 2017). Nous avons pu aussi généraliser notre code *FastCycles* au mode II (”in-plane”). La généralisation au mode I et aux modes mixtes est aussi possible avec les matrices hiérarchiques. Nous avons donc développé un code d’éléments aux frontières quasi-dynamique, nommé FastCycles, qui permet de modéliser n’importe quelle géométrie et réseau de failles, avec une loi de friction de type rate and state, et ce, de manière particulièrement rapide par rapport aux codes existants non parallèles.

Prenant avantage de la rapidité du code, nous avons pu étudier un large ensemble de variables pour deux failles en superposition qui interagissent en mode III (”out-of-plane”) . Ce qui ressort de cette étude est que même une des plus simples complexités géométriques (deux failles en superposition) peut donner lieu à un large éventail de comportements du cycle sismique, incluant des ruptures partielles, des évènements de glissement lent et des tremblements de terre, et un comportement apériodique sans pour autant devoir faire appel à des variations de la rhéologie des failles (en faisant varier les paramètres de friction). Dans cette configuration géométrique, nous avons montré que les principaux paramètres contrôlant la dynamique du système étaient le ratio de la longueur de la faille sur la longueur caractéristique de nucléation, la distance entre les failles, et le ratio a/b des paramètres de friction. Nous avons aussi pu montrer que dans le cas particulier du domaine où évènements de glissement lent et tremblements de terre coexistent, leur moment suit une loi d’échelle qui semble différente pour les deux types d’évènements à savoir : $M_0 \propto T$ pour les glissements lents et $M_0 \propto T^2$ pour les tremblements de terre. Cela est a rapproché des deux lois d’échelle observées par *Ide et al.* (2007) : $M_0 \propto T$ pour les glissements lents et $M_0 \propto T^3$ pour les tremblements de terre. La différence de puissance pour les tremblements de terre pourrait être due au fait que notre modèle est en 2 dimensions seulement.

Dans la dernière partie de cette thèse nous avons pu montrer des résultats préliminaires pour diverses configurations utilisant cette fois le mode II (”in-plane”). Nous avons montré que l’existence d’une variation de pression de pore pouvait perturber le cycle sismique des failles et en particulier faire apparaître du glissement lent, chose qui a déjà été observée lors d’une expérience grandeur nature d'injection d'eau le long d'une faille dans le sud-est de la France (*Guglielmi et al.*, 2015).

Nous nous sommes aussi intéressés à la rugosité et aux réseaux de faille. Nous avons montré que la rugosité, avait une forte influence sur le cycle sismique lorsque le mode II (in-plane) était considéré. En particulier, nous avons obtenu une distribution en taille des évènements, des ruptures lentes et rapides et de l'apériodicité. Un résultat très intéressant de cette étude est qu'il semble que l'on puisse s'affranchir du contrôle de la longueur de nucléation en prenant en compte des failles rugueuses. En effet les failles testées étant plus grandes que la longueur de nucléation d'un facteur 5, il semble que la distribution en taille des évènements obtenus ne soit due qu'à la rugosité. Si c'est vraiment le cas, la longueur de nucléation ne contraindrait plus que la taille du plus petit évènement possible dans le modèle, et non plus la dynamique du modèle lui même.

5.2 Perspectives futures

5.2.1 Rugosité et réseau de failles

Dans la dernière section de cette thèse, nous avons obtenu des résultats intéressants mais préliminaires provenant de modélisation du cycle sismique sur des réseaux de failles, et des failles rugueuses. Il conviendrait de faire une étude plus précise des paramètres qui contrôlent le comportement de ces failles. En particulier, a quelle condition sur le réseau ou la rugosité des lois d'échelle apparaissent t'elles ? Pourrait-on reproduire la loi de Gutenberg Richter juste en utilisant la rugosité sur une faille ? Pourrait-on vraiment démontrer que la rugosité des failles permet de s'affranchir du contrôle de la longueur de nucléation dans les modèles ? Dans les configurations que nous avons testé sur une faille unique rugueuse, il semble que non, cependant nous n'avons testé qu'un nombre extrêmement restreint de paramètres. La rapidité de cette méthode permet justement d'explorer un grand nombre de paramètres. Une autre question intéressante qui semble émerger de ces simulations est la possible synchronisation des réseaux de faille par transfert de contraintes. Plusieurs études semblent pointer dans ce sens, à savoir des études paleosismologiques (*Rockwell et al.*, 2000 ;

Ganev et al., 2010), à une échelle locale (*Scholz*, 2010) ou régionale *Dolan et al.* (2007), et même à l'échelle mondiale (*Bendick and Bilham*, 2017). Bien que les mécanismes diffèrent ici, nous pourrions tester si le transfert de contraintes de Coulomb peut, à l'échelle locale, synchroniser les failles.

5.2.2 Simulation complètement dynamique en 3D

Un objectif à moyen terme pourrait être de généraliser ce code, en incluant complètement la partie dynamique de la rupture en 3 dimensions (FastCycles est un modèle quasi-dynamique, 2D). *Ando* (2016) a trouvé une manière originale de décomposer le calcul en élément frontière globale en séparant : (1) la partie statique, (2) le domaine entre les ondes P et les ondes S, (3) la partie relative aux ondes P et (4) la partie relative aux ondes S du noyau. Dans l'annexe C de son article, il y discute la possibilité d'utiliser les matrices hiérarchiques pour encore plus accélérer le calcul. Passer de 2 dimensions à 3 dimensions pourrait aider à résoudre certain problème, notamment le problème d'accumulation de contrainte normale sur la faille en mode 2 et en deux dimensions. Si nous souhaitons passer à la 3D , il faudra sans aucun doute paralléliser le code. Les matrices hiérarchiques à cause de leur structure, se prètent plutôt bien à la parallélisation.

5.2.3 Atténuation des risques liés aux tremblements de terre

Finalement une autre perspective intéressante, pourrait être la création de banque de scénarios pour un système de failles donné. En effet, notre code *FastCycles* inclut la partie statique de l'interaction des failles, se faisant il pourrait se poser en complément pour aider à mieux contraindre les modèles probabilistes actuels de rupture des failles, en prennant en compte de possibles scénarios de ruptures sur plusieurs failles. C'est quelque chose que nous comptons explorer dans un future proche.

5.3 Conclusions générales

Cette thèse a aussi été l'occasion d'en apprendre plus sur les possibilités offertes par les matrices hiérarchiques et la méthode multipolaire rapide. La méthode multipolaire rapide est adaptée à des cas particuliers, et est assez longue à mettre en place à cause du dévelopement nécessaire des noyaux. En revanche, les matrices hiérarchiques sont particulièrement simples à mettre en place et pourraient permettre d'accélérer de nombreux codes éxistants. De nombreux problèmes en géophysique comportent des noyaux adaptés aux matrices hiérarchiques. D'une manière générale, il ressort de cette thèse que toute perturbation de contrainte, que ce soit à cause de la rugosité, de l'interaction d'autres failles, ou de l'injection d'eau usée, peut créer les conditions favorables à l'apparition d'évènements de glissement lent. La détection de plus en plus importante d'évènements lents le long des failles, nous pousse à penser que cela n'est pas qu'une propriété de ce modèle, mais bien un comportement général. Nous avons montré dans cette thèse que la prise en compte de la géométrie dans les simulations du cycle sismique était une manière élégante de reproduire des comportements sismiques observés. Bien sûr, la rhéologie a aussi probablement un rôle important, et seulement la prise en compte de ces deux effets pourra nous permettre de réellement comprendre le cycle sismique.

Bibliographie

Agnew, D. C. (2002), History of seismology, *International handbook of earthquake and engineering seismology*, *81*, 3–11.

Aki, K., and P. G. Richards (2002), *Quantitative Seismology*, University Science Books.

Ampuero, J.-P., and A. M. Rubin (2008), Earthquake nucleation on rate and state faults–aging and slip laws, *J. Geophys. Res.*, *113*(B1), doi :10.1029/2007JB005082.

Ando, R. (2016), Fast domain partitioning method for dynamic boundary integral equations applicable to non-planar faults dipping in 3-d elastic half-space, *Geophys. J. Int.*, p. ggw299.

Andrews, D. J. (1976), Rupture velocity of plane strain shear cracks, *J. Geophys. Res.*, *81*(B32), 5679–5689.

Araki, E., D. M. Saffer, A. J. Kopf, L. M. Wallace, T. Kimura, Y. Machida, S. Ide, E. Davis, I. Expedition, et al. (2017), Recurring and triggered slow-slip events near the trench at the nankai trough subduction megathrust, *Science*, *356*(6343), 1157–1160, doi :10.1126/science.aan3120.

Barbot, S., N. Lapusta, and J.-P. Avouac (2012), Under the hood of the earthquake machine : Toward predictive modeling of the seismic cycle, *Science*, *336*(6082), 707–710, doi :10.1126/science.1218796.

Barbour, A. J., J. H. Norbeck, and J. L. Rubinstein (2017), The effects of varying injection rates in osage county, oklahoma, on the 2016 m w 5.8 pawnee earthquake, *Seismol. Res. Lett.*, doi :10.1785/0220170003.

Beatson, R., and L. Greengard (1997), A short course on fast multipole methods.

Bebendorf, M., and S. Rjasanow (2003), Adaptive low-rank approximation of collocation matrices, *Computing*, *70*(1), 1–24, doi :10.1007/s00607-002-1469-6.

Bendick, R., and R. Bilham (2017), Do weak global stresses synchronize earthquakes ?, *Geophys. Res. Lett.*, doi :10.1002/2017GL074934.

Beroza, G. C., and S. Ide (2011), Slow earthquakes and nonvolcanic tremor, *Annual review of Earth and planetary sciences*, *39*, 271–296, doi :10.1146/annurev-earth-040809-152531.

Bhat, H. S., M. Olives, R. Dmowska, and J. R. Rice (2007), Role of fault branches in earthquake rupture dynamics, *J. Geophys. Res.*, *B11309*, doi :10.1029/2007JB005027.

Bhattacharya, P., A. M. Rubin, E. Bayart, H. M. Savage, and C. Marone (2015), Critical evaluation of state evolution laws in rate and state friction : Fitting large velocity steps in simulated fault gouge with time-, slip-, and stress-dependent constitutive laws, *J. Geophys. Res.*, *120*(9), 6365–6385, doi :10.1002/2015JB012437.

Bilham, R., H. Ozener, D. Mencin, A. Dogru, S. Ergintav, Z. Cakir, A. Aytun, B. Aktug, O. Yilmaz, W. Johnson, and G. Mattioli (2016), Surface creep on the north anatolian fault at ismetpasa, turkey, 1944–2016, *J. Geophys. Res.*, *121*(10), 7409–7431, doi :10.1002/2016JB013394.

Blanpied, M., C. Marone, D. Lockner, J. Byerlee, and D. King (1998), Quantitative measure of the variation in fault rheology due to fluid-rock interactions, *J. Geophys. Res.*, *103*(B5), 9691–9712.

Bodvarsson, G. (1970), Confined fluids as strain meters, *J. Geophys. Res.*, *75*(14), 2711–2718.

Börm, S., L. Grasedyck, and W. Hackbusch (2003), Introduction to hierarchical matrices with applications, *Engineering analysis with boundary elements*, *27*(5), 405–422, doi :10.1016/S0955-7997(02)00152-2.

Brace, W. F., and J. D. Byerlee (1966), Stick-slip as a mechanism for earthquakes, *Science*, *153*(3739), 990–992.

Brace, W. F., B. W. Paulding Jr, and C. Scholz (1966), Dilatancy in the fracture of crystalline rocks, *J. Geophys. Res.*, *71*, 3939–3953.

Brodsky, E. E., and T. Lay (2014), Recognizing Foreshocks from the 1 April 2014 Chile Earthquake, *Science*, *344*(6185), 700–702, doi :10.1126/science.1255202.

Bulirsch, R., and J. Stoer (1966), Numerical treatment of ordinary differential equations by extrapolation methods, *Numerische Mathematik*, *8*(1), 1–13.

Burridge, R. (1969), The numerical solution of certain integral equations with non-integrable kernels arising in the theory of crack propagation and elastic wave diffraction, *Phil. Trans. R. Soc. Lond. A*, *265*(1163), 353–381.

Burridge, R., and L. Knopoff (1967), Model and theoretical seismicity, *B. Seismol. Soc. Am.*, *57*(3), 341–371.

Candela, T., F. Renard, M. Bouchon, A. Brouste, D. Marsan, J. Schmittbuhl, and C. Voisin (2009), Characterization of fault roughness at various scales : Implications of three-dimensional high resolution topography measurements, in *Mechanics, Structure and Evolution of Fault Zones*, pp. 1817–1851, Springer.

Candela, T., F. Renard, J. Schmittbuhl, M. Bouchon, and E. E. Brodsky (2011), Fault slip distribution and fault roughness, *Geophys. J. Int.*, *187*(2), 959–968, doi :10.1111/j.1365-246X.2011.05189.x.

Candela, T., F. Renard, Y. Klinger, K. Mair, J. Schmittbuhl, and E. E. Brodsky (2012), Roughness of fault surfaces over nine decades of length scales, *J. Geophys. Res.*, *117*, B08,409, doi :10.1029/2011JB009041.

Carlson, J., and J. Langer (1989), Mechanical model of an earthquake fault, *Physical Review A*, *40*(11), 6470.

Carrier, J., L. Greengard, and V. Rokhlin (1988), A fast adaptive multipole algorithm for particle simulations, *SIAM J. Sci. Stat. Comput.*, *9*(4), 669–686.

Carslaw, H. S., and J. C. Jaeger (1959), *Conduction of heat in solids*, Oxford Clarendon Press.

Chen, T., and N. Lapusta (2009), Scaling of small repeating earthquakes explained by interaction of seismic and aseismic slip in a rate and state fault model, *J. Geophys. Res.*, *114*(B1), doi :10.1029/2008JB005749.

Cochard, A., and R. Madariaga (1994), Dynamic faulting under rate-dependent friction, *Pure Appl. Geophys.*, *142*, 419–445.

Desiderio, L. (2017), H-matrix based solvers for 3d elastodynamic boundary integral equations, Ph.D. thesis, Université Paris-Saclay, ENSTA Paris-Tech.

Dieterich, J. (1979), Modeling of rock friction 1. experimental results and constitutive equations, *J. Geophys. Res.*, *84*(B5), 2161—2168.

Dieterich, J., and B. Kilgore (1994), Direct observation of frictional contacts : New insights for state-dependent properties, *Pure Appl. Geophys.*, *143*(1), 283–302.

Dieterich, J. H. (1978), Time-dependent friction and the mechanics of stick-slip, *Pure Appl. Geophys.*, *116*(4-5), 790–806.

Dieterich, J. H. (1992), Earthquake nucleation on faults with rate-and state-dependent strength, *Tectonophysics*, *211*(1-4), 115–134.

Dolan, J. F., D. D. Bowman, and C. G. Sammis (2007), Long-range and long-term fault interactions in southern california, *Geology*, *35*(9), 855–858, doi :10.1130/G23789A.1.

Douglas, A., J. Beavan, L. Wallace, and J. Townend (2005), Slow slip on the northern hikurangi subduction interface, new zealand, *Geophys. Res. Lett.*, *32*(16), doi :10.1029/2005GL023607.

Dragert, H., K. Wang, and T. S. James (2001), A silent slip event on the deeper cascadia subduction interface, *Science*, *292*(5521), 1525–1528.

Dragert, H., K. Wang, and G. Rogers (2004), Geodetic and seismic signatures of episodic tremor and slip in the northern cascadia subduction zone, *Earth Planets Space*, *56*(12), 1143–1150.

Dublanchet, P., P. Bernard, and P. Favreau (2013), Interactions and triggering in a 3-d rate-and-state asperity model, *J. Geophys. Res.*, *118*(5), 2225–2245, doi :10.1002/jgrb.50187.

Dunham, E. M., D. Belanger, L. Cong, and J. E. Kozdon (2011), Earthquake ruptures with strongly rate-weakening friction and off-fault plasticity, part 2 : Nonplanar faults, *Bull. Seism. Soc. Am.*, *101*(5), 2308–2322, doi :10.1785/0120100076.

Duputel, Z., and L. Rivera (2017), Long-period analysis of the 2016 kaikoura earthquake, *Phys. Earth Planet. In.*, *265*, 62–66, doi :0.1016/j.pepi.2017.02.004.

Ellsworth, W. L. (2013), Injection-induced earthquakes, *Science*, *341*, doi : 10.1126/science.1225942.

Ellsworth, W. L., A. L. Llenos, A. F. McGarr, A. J. Michael, J. L. Rubinstein, C. S. Mueller, M. D. Petersen, and E. Calais (2015), Increasing seismicity in the us midcontinent : Implications for earthquake hazard, *The Leading Edge*, *34*(6), 618–626.

Franco, S., V. Kostoglodov, K. Larson, V. Manea, M. Manea, and J. Santiago (2005), Propagation of the 2001-2002 silent earthquake and interplate coupling in the oaxaca subduction zone, mexico, *Earth Planets Space*, *57*(10), 973–985.

Ganev, P. N., J. F. Dolan, K. Blisniuk, M. Oskin, and L. A. Owen (2010), Paleoseismologic evidence for multiple holocene earthquakes on the calico fault : Implications for earthquake clustering in the eastern california shear zone, *Lithosphere*, *2*(4), 287–298, doi :10.1130/L82.1.

Gao, H., D. A. Schmidt, and R. J. Weldon (2012), Scaling relationships of source parameters for slow slip events, *Bull. Seism. Soc. Am.*, *102*(1), 352–360, doi :10.1785/0120110096.

Gilbert, G. K. (1884), A theory of the earthquakes of the great basin, with a practical application, *American Journal of Science*, *27*(157), 49–53.

Goebel, T., M. Weingarten, X. Chen, J. Haffener, and E. Brodsky (2017), The 2016 mw5. 1 fairview, oklahoma earthquakes : Evidence for long-range poroelastic triggering at> 40 km from fluid disposal wells, *Earth Planet. Sc. Lett.*, *472*, 50–61, doi :10.1016/j.epsl.2017.05.011.

Greengard, L., and V. Rokhlin (1987), A fast algorithm for particle simulations, *J. Comput. Phys.*, *73*(2), 325–348.

Gu, J.-C., J. R. Rice, A. L. Ruina, and T. T. Simon (1984), Slip motion and stability of a single degree of freedom elastic system with rate and state dependent friction, *J. Mech. Phys. Solids*, *32*(3), 167–196.

Gualandi, A., C. Nichele, E. Serpelloni, L. Chiaraluce, L. Anderlini, D. Latorre, M. Belardinelli, and J.-P. Avouac (2017), Aseismic deformation associated with an earthquake swarm in the northern apennines (italy), *Geophys. Res. Lett.*, doi :10.1002/2017GL073687.

Guglielmi, Y., F. Cappa, J.-P. Avouac, P. Henry, and D. Elsworth (2015), Seismicity triggered by fluid injection–induced aseismic slip, *Science*, *348*(6240), 1224–1226, doi :10.1126/science.aab0476.

Hackbusch, W. (1999), A sparse matrix arithmetic based on-matrices. part i : Introduction to-matrices, *Computing*, *62*(2), 89–108.

Hamling, I. J., S. Hreinsdóttir, K. Clark, J. Elliott, C. Liang, E. Fielding, N. Litchfield, P. Villamor, L. Wallace, T. J. Wright, E. D'Anastasio, S. Bannister, D. Burbidge, P. Denys, P. Gentle, J. Howarth, C. Mueller, N. Palmer, C. Pearson, W. Power, P. Barnes, D. J. A. Barrell, R. Van Dissen, R. Langridge, T. Little, A. Nicol, J. Pettinga, J. Rowland, and M. Stirling (2017), Complex multifault rupture during the 2016 Mw 7.8 Kaikoura earthquake, New Zealand, *Science*, doi :10.1126/science.aam7194.

Hand, E. (2014), Injection wells blamed in oklahoma earthquakes, *Science*, *345*(6192), 13–14, doi :10.1126/science.345.6192.13.

Hirahara, K., N. Mitsui, and T. Hori (2009), Development of a fast code for earthquake cycle simulation-(1) application of fast multipole method, *Eos Trans. AGU*, *90(52), Fall Meet. Suppl.*, Abstract T23C–1929.

Hirose, H., K. Hirahara, F. Kimata, N. Fujii, and S. Miyazaki (1999), A slow thrust slip event following the two 1996 hyuganada earthquakes beneath the bungo channel, southwest japan, *Geophys. Res. Lett.*, *26*(21), 3237–3240.

Hollingsworth, J., L. Ye, and J.-P. Avouac (2017), Dynamically triggered slip on a splay fault in the mw 7.8, 2016 kaikoura (new zealand) earthquake, *Geophys. Res. Lett.*, *44*(8), 3517–3525, doi :10.1002/2016GL072228.

Huang, J., and D. L. Turcotte (1990), Are earthquakes an example of deterministic chaos ?, *Geophys. Res. Lett.*, *17*(3), 223–226.

Ide, S., G. C. Beroza, D. R. Shelly, and T. Uchide (2007), A scaling law for slow earthquakes, *Nature*, *447*(7140), 76–79, doi :10.1038/nature05780.

Ide, S., K. Imanishi, Y. Yoshida, G. C. Beroza, and D. R. Shelly (2008), Bridging the gap between seismically and geodetically detected slow earthquakes, *Geophys. Res. Lett.*, *35*(10), L10,305, doi :10.1029/2008GL034014.

Igarashi, T., T. Matsuzawa, and A. Hasegawa (2003), Repeating earthquakes and interplate aseismic slip in the northeastern japan subduction zone, *J. Geophys. Res.*, *108*(B5), 2249, doi :10.1029/2002JB001920.

Itaba, S., and R. Ando (2011), A slow slip event triggered by teleseismic surface waves, *Geophys. Res. Lett.*, *38*(21), L21,306, doi :10.1029/2011GL049593,2011.

Ito, Y., R. Hino, M. Kido, H. Fujimoto, Y. Osada, D. Inazu, Y. Ohta, T. Iinuma, M. Ohzono, S. Miura, M. Mishina, K. Suzuki, T. Tsuji, and J. Ashi (2013), Episodic slow slip events in the japan subduction zone before the 2011 tohoku-oki earthquake, *Tectonophysics*, *600*, 14–26, doi :10.1016/j.tecto.2012.08.022.

Jaswon, M., and A. Ponter (1963), An integral equation solution of the torsion problem, in *Proceedings of the Royal Society of London A : Mathematical, Physical and Engineering Sciences*, vol. 273, pp. 237–246, The Royal Society.

Jolivet, R., C. Lasserre, M.-P. Doin, G. Peltzer, J.-P. Avouac, J. Sun, and R. Dailu (2013), Spatio-temporal evolution of aseismic slip along the haiyuan fault, china : Implications for fault frictional properties, *Earth Planet. Sc. Lett.*, *377*, 23–33, doi :10.1016/j.epsl.2013.07.020.

Jolivet, R., T. Candela, C. Lasserre, F. Renard, Y. Klinger, and M.-P. Doin (2015), The burst-like behavior of aseismic slip on a rough fault : The creeping section of the haiyuan fault, china, *Bull. Seism. Soc. Am.*, *105*(1), 480–488, doi :10.1785/0120140237.

Kame, N., and T. Yamashita (2003), Dynamic branching, arresting of rupture and the seismic wave radiation in self-chosen crack path modelling, *Geophys. J. Int.*, *155*, 1042–1050.

Kato, A., and S. Nakagawa (2014), Multiple slow-slip events during a foreshock sequence of the 2014 iquique, chile mw 8.1 earthquake, *Geophys. Res. Lett.*, *41*(15), 5420–5427, doi :10.1002/2014GL061138.

Kato, A., K. Obara, T. Igarashi, H. Tsuruoka, S. Nakagawa, and N. Hirata (2012), Propagation of Slow Slip Leading Up to the 2011 Mw 9.0 Tohoku-Oki Earthquake, *Science*, *335*(6069), 705–708, doi :10.1126/science.1215141.

Kato, A., T. Igarashi, and K. Obara (2014), Detection of a hidden boso slow slip event immediately after the 2011 mw 9.0 tohoku-oki earthquake, japan, *Geophysical Research Letters*, *41*(16), 5868–5874, doi : 10.1002/2014GL061053.

Kato, N., and T. E. Tullis (2001), A composite rate-and state-dependent law for rock friction, *Geophys. Res. Lett.*, *28*(6), 1103–1106.

Keranen, K. M., H. M. Savage, G. A. Abers, and E. S. Cochran (2013), Potentially induced earthquakes in oklahoma, usa : Links between wastewater injection and the 2011 mw 5.7 earthquake sequence, *Geology*, *41*(6), 699–702, doi :10.1130/G34045.1.

King, G. C. P., and J. Nabelek (1985), The role of bends in faults in the initiation and termination of earthquake rupture, *Science*, *228*, 984–987.

Klinger, Y. (2010), Relation between continental strike-slip earthquake segmentation and thickness of the crust, *J. Geophys. Res.*, *115*, B07,306, doi :10.1029/2009JB006550.

Koller, M. G., M. Bonnet, and R. Madariaga (1992), Modelling of dynamical crack propagation using time-domain boundary integral equations, *Wave Motion*, *16*(4), 339–366.

Komatitsch, D., and J. P. Vilotte (1998), The spectral element method : An efficient tool to simulate the seismic response of 2D and 3D geological structures, *Bull. Seism. Soc. Am.*, *88*(2), 368.

Kostoglodov, V., S. K. Singh, J. A. Santiago, S. I. Franco, K. M. Larson, A. R. Lowry, and R. Bilham (2003), A large silent earthquake in the guerrero seismic gap, mexico, *Geophys. Res. Lett.*, *30*(15), doi : 10.1029/2003GL017219.

Kostrov, B. (1966), Unsteady propagation of longitudinal shear cracks, *J. Appl. Math. Mech.-USS.*, *30*, 1241–1248.

Koto, B. (1893), On the cause of the great earthquake in central japan, 1891, *J. Coll. Sci. Imp. Univ. Tokyo*, *5*(295–353).

Lay, T., and H. Kanamori (1981), An asperity model of large earthquake sequences, in *Earthquake Prediction, an International Review, Maurice Ewing Series*, vol. IV, edited by D. W. Simpson and P. Richards, pp. 579–592, AGU, Washington, D. C., doi :10.1029/ME004p0579.

Lee, J.-J., and R. L. Bruhn (1996), Structural anisotropy of normal fault surfaces, *J. Struct. Geol.*, *18*(8), 1043–1059.

Lee, W. H. K., H. Kanamori, P. C. Jennings, and C. Kisslinger (2002), *International Handbook of Earthquake and Engineering Seismology-Part A*, Elsevier Science & Technology Books.

Li, D., and Y. Liu (2016), Spatiotemporal evolution of slow slip events in a nonplanar fault model for northern cascadia subduction zone, *J. Geophys. Res.*, *121*(9), 6828–6845, doi :10.1002/2016JB012857.

Lienkaemper, J. J., J. S. Galehouse, and R. W. Simpson (1997), Creep response of the hayward fault to stress changes caused by the loma prieta earthquake, *Science*, *276*(5321), 2014–2016.

Linker, M., and J. Dieterich (1992), Effects of variable normal stress on rock friction : Observations and constitutive equations, *J. Geophys. Res.*, *97*(B4), 4923–4940.

Liu, Y., and J. R. Rice (2005), Aseismic slip transients emerge spontaneously in 3d rate and state modeling of subduction earthquake sequences, *J. Geophys. Res.*, *110*, B08,307, doi :10.1029/2004JB003424.

Liu, Y., and J. R. Rice (2007), Spontaneous and triggered aseismic deformation transients in a subduction fault model, *J. Geophys. Res.*, *112*, B09,404, doi :10.1029/2007JB004930.

Lowry, A. R., K. M. Larson, V. Kostoglodov, and R. Bilham (2001), Transient fault slip in guerrero, southern mexico, *Geophys. Res. Lett.*, *28*(19), 3753–3756, doi :0094-8276/01/2001GL000000$05.00.

Madariaga, R. (1976), Dynamics of an expanding circular fault, *Bull. Seism. Soc. Am.*, *66*(3), 639–666.

Madariaga, R., A. Cochard, et al. (1992), Heterogenous faulting and friction, in *Simposio Internacional sobre Prevención de Desastres Sísmicos= International Symposium on Earthquake Disaster Prevention*, pp. 103–18, México. Centro Nacional de Prevención de Desastes (CENAPRED) ; Japón. Agencia de Cooperación Internacional (JICA) ; NU. Centro para el Desarrollo Regional (UNCRD).

Marone, C. (1998), Laboratory-derived friction laws and their application to seismic faulting, *Ann. Rev. Earth Planet. Sci.*, *26*(1), 643–696.

Matsuzawa, T., B. Shibazaki, K. Obara, and H. Hirose (2013), Comprehensive model of short-and long-term slow slip events in the shikoku region of japan, incorporating a realistic plate configuration, *Geophys. Res. Lett.*, *40*(19), 5125–5130, doi :10.1002/grl.51006.

Maury, J., H. Aochi, and M. Radiguet (2014), Fault constitutive relations inferred from the 2009-2010 slow slip event in guerrero, mexico, *Geophys. Res. Lett.*, *41*, 4929–4936, doi :10.1002/2014GL060691.

Mavrommatis, A. P., P. Segall, N. Uchida, and K. M. Johnson (2015), Long-term acceleration of aseismic slip preceding the Mw 9 Tohoku-oki earthquake : Constraints from repeating earthquakes, *Geophys. Res. Lett.*, *42*, 9717–9725, doi :10.1002/2015GL066069.

Melosh, H. J., and A. Raefsky (1981), A simple and efficient method for introducing faults into finite element computations, *Bull. Seism. Soc. Am.*, *71*(5), 1391–1400.

Michel, S., J.-P. Avouac, N. Lapusta, and J. Jiang (2017), Pulse-like partial ruptures and high-frequency radiation at creeping-locked transition during megathrust earthquakes, *Geophys. Res. Lett.*, doi :10.1002/2017GL074725.

Mitsui, N., and K. Hirahara (2006), Slow slip events controlled by the slab dip and its lateral change along a trench, *Earth Planet. Sc. Lett.*, *245*(1), 344–358, doi :10.1016/j.epsl.2006.03.001.

Murray, J. R., and P. Segall (2005), Spatiotemporal evolution of a transient slip event on the san andreas fault near parkfield, california, *J. Geophys. Res.*, *110*(B9), doi :10.1029/2005JB003651.

Nishimura, N., K.-i. Yoshida, and S. Kobayashi (1999), A fast multipole boundary integral equation method for crack problems in 3d, *Eng. Anal. Bound. Elem.*, *23*(1), 97–105.

Noda, H., N. Lapusta, and H. Kanamori (2013), Comparison of average stress drop measures for ruptures with heterogeneous stress change and implications for earthquake physics, *Geophys. J. Int.*, *193*, 1691—1712, doi :10.1093/gji/ggt074.

Nussbaum, J., and A. Ruina (1987), A two degree-of-freedom earthquake model with static/dynamic friction, *Pure and Applied Geophysics*, *125*(4), 629–656.

Obara, K. (2002), Nonvolcanic deep tremor associated with subduction in southwest Japan, *Science*, *296*(5573), 1679–1681.

Obara, K., and A. Kato (2016), Connecting slow earthquakes to huge earthquakes, *Science*, *353*(6296), 253–257, doi :10.1126/science.aaf1512.

Obara, K., H. Hirose, F. Yamamizu, and K. Kasahara (2004), Episodic slow slip events accompanied by non-volcanic tremors in southwest japan subduction zone, *Geophys. Res. Lett.*, *31*(23), doi :10.1029/2004GL020848.

Ohtani, M., K. Hirahara, Y. Takahashi, T. Hori, M. Hyodo, H. Nakashima, and T. Iwashita (2011), Fast computation of quasi-dynamic earthquake cycle simulation with hierarchical matrices, *Procedia Comput. Sci.*, *4*, 1456–1465, doi :10.1016/j.procs.2011.04.158.

Peng, Z., and J. Gomberg (2010), An integrated perspective of the continuum between earthquakes and slow-slip phenomena, *Nature Geoscience*, *3*(9), 599–607, doi :10.1038/ngeo940.

Perfettini, H., J.-P. Avouac, H. Tavera, A. Kositsky, J.-M. Nocquet, F. Bondoux, M. Chlieh, A. Sladen, L. Audin, D. L. Farber, and P. Soler (2010), Seismic and aseismic slip on the central peru megathrust, *Nature*, *465*, 78–81, doi :10.1038/nature09062.

Perrin, G., J. R. Rice, and G. Zheng (1995), Self-healing slip pulse on a frictional surface, *J. Mech. Phys. Solids*, *43*(9), 1461–1495.

Power, W., T. Tullis, S. Brown, G. Boitnott, and C. Scholz (1987), Roughness of natural fault surfaces, *Geophys. Res. Lett.*, *14*(1), 29–32.

Power, W. L., and T. E. Tullis (1991), Euclidean and fractal models for the description of rock surface roughness, *J. Geophys. Res.*, *96*(B1), 415–424.

Press, W. H., S. A. Teukolsky, W. T. Vetterling, and B. P. Flannery (1993), *Numerical Recipes in Fortran 77 : The Art of Scientific Computing 1*, Cambridge University Press.

Rabinowicz, E. (1958), The intrinsic variables affecting the stick-slip process, *Proc. Phys. Soc.*, *71*(4), 668.

Radiguet, M., H. Perfettini, N. Cotte, A. Gualandi, B. Valette, V. Kostoglodov, T. Lhomme, A. Walpersdorf, E. Cabral Cano, and M. Campillo (2016), Triggering of the 2014 mw7.3 papanoa earthquake by a slow slip event in guerrero, mexico, *Nature Geoscience*, *9*, 829–833, doi :10.1038/NGEO2817.

Ranjith, K., and J. R. Rice (1999), Stability of quasi-static slip in a single degree of freedom elastic system with rate and state dependent friction, *J. Mech. Phys. Solids*, *47*(6), 1207–1218.

Renard, F., C. Voisin, D. Marsan, and J. Schmittbuhl (2006), High resolution 3d laser scanner measurements of a strike-slip fault quantify its morphological anisotropy at all scales, *Geophys. Res. Lett.*, *33*(4), doi : 10.1029/2005GL025038.

Rice, J. R. (1983), Constitutive relations for fault slip and earthquake instabilities, *Pure Appl. Geophys.*, *121*(3), 443–475.

Rice, J. R. (1992), Fault stress states, pore pressure distributions, and the weakness of the san andreas fault, in *Fault Mechanics and Transport Properties in Rocks*, edited by B. Evans and T. F. Wong, pp. 475–503, Academic Press.

Rice, J. R. (1993), Spatio-temporal complexity of slip on a fault, *J. Geophys. Res.*, *98*(B6), 9885–9907.

Rice, J. R. (2006), Heating and weakening of faults during earthquake slip, *J. Geophys. Res.*, *111*(B05311), doi :10.1029/2005JB004006.

Rockwell, T. K., S. Lindvall, M. Herzberg, D. Murbach, T. Dawson, and G. Berger (2000), Paleoseismology of the johnson valley, kickapoo and homestead valley faults : Clustering of earthquakes in the eastern california shear zone, *Bull. Seism. Soc. Am.*, *90*(5), 1200–1236.

Rogers, G., and H. Dragert (2003), Episodic tremor and slip on the Cascadia subduction zone : The chatter of silent slip, *Science*, *300*(5627), 1942–1943.

Rousset, B., R. Jolivet, M. Simons, C. Lasserre, B. Riel, P. Milillo, Z. Çakir, and F. Renard (2016), An aseismic slip transient on the north anatolian fault, *Geophys. Res. Lett.*, *43*(7), 3254–3262, doi :10.1002/2016GL068250.

Rubin, A., and J.-P. Ampuero (2005), Earthquake nucleation on (aging) rate and state faults, *J. Geophys. Res.*, *110*, B11,312, doi :10.1029/2005JB003686.

Rubin, A. M. (2008), Episodic slow slip events and rate-and-state friction, *J. Geophys. Res.*, *113*, B11,414, doi :10.1029/2008JB005642.

Ruina, A. (1983), Slip instability and state variable friction laws, *J. Geophys. Res.*, *88*(10), 359–370.

Ruiz, S., M. Metois, A. Fuenzalida, J. Ruiz, F. Leyton, R. Grandin, C. Vigny, R. Madariaga, and J. Campos (2014), Intense foreshocks and a slow slip event preceded the 2014 iquique mw 8.1 earthquake, *Science*, *345*(6201), 1165–1169, doi :10.1126/science.1256074.

Saffer, D. M., and L. M. Wallace (2015), The frictional, hydrologic, metamorphic and thermal habitat of shallow slow earthquakes, *Nature Geoscience*, doi :10.1038/NGEO2490.

Schmitt, S., P. Segall, and T. Matsuzawa (2011), Shear heating-induced thermal pressurization during earthquake nucleation, *J. Geophys. Res.*, *116*(B6), doi :10.1029/2010JB008035.

Schmittbuhl, J., S. Gentier, and S. Roux (1993), Field measurements of the roughness of fault surfaces, *Geophys. Res. Lett.*, *20*(8), 639–641.

Scholz, C. H. (2002), *The mechanics of earthquakes and faulting*, Cambridge Univ Press.

Scholz, C. H. (2010), Large earthquake triggering, clustering, and the synchronization of faults, *Bulletin of the Seismological Society of America*, *100*(3), 901–909, doi :10.1785/0120090309.

Schwartz, S. Y., and J. M. Rokosky (2007), Slow slip events and seismic tremor at circum-pacific subduction zones, *Rev. Geophys.*, *45*(3), 1–32, doi :10.1029/2006RG000208.

Segall, P. (2010), *Earthquake and volcano deformation*, Princeton University Press.

Segall, P., and A. M. Bradley (2012a), The role of thermal pressurization and dilatancy in controlling the rate of fault slip, *J. Appl. Mech.*, *79*(3), 031,013.

Segall, P., and A. M. Bradley (2012b), Slow-slip evolves into megathrust earthquakes in 2d numerical simulations, *Geophys. Res. Lett.*, *39*(18), L18,308, doi :10.1029/2012GL052811.

Segall, P., and J. R. Rice (1995), Dilatancy, compaction, and slip instability of a fluid-infiltrated fault, *J. Geophys. Res.*, *100*(B11), 22,155–22,171.

Segall, P., A. M. Rubin, A. M. Bradley, and J. R. Rice (2010), Dilatant strengthening as a mechanism for slow slip events, *J. Geophys. Res.*, *115*, B12,305, doi :10.1029/2010JB007449,.

Shapiro, S. A., E. Huenges, and G. Borm (1997), Estimating the crust permeability from fluid-injection-induced seismic emission at the ktb site, *Geophys. J. Int.*, *131*(2).

Sibson, R. H. (1985), Stopping of earthquake ruptures at dilational fault jogs, *Nature*, *316*(6025), 248–251.

Sieh, K., L. Jones, E. Hauksson, K. Hudnut, D. Eberhart-Phillips, T. Heaton, S. Hough, K. Hutton, H. Kanamori, A. Lilje, S. Lindvall, S. F. McGill, J. Mori, C. Rubin, J. A. Spotila, J. Stock, H. K. Thio, J. Treiman, B. Wernicke, and J. Zachariasen (1993), Near-field investigations of the landers earthquake sequence, april to july 1992, *Science*, *260*(5105), 171–176.

Sladek, V., and J. Sladek (1984), Transient elastodynamic three-dimensional problems in cracked bodies, *Appl. Math. Modelling*, *8*(1), 2–10.

Sowers, J. M., J. R. Unruh, W. R. Lettis, and T. D. Rubin (1994), Relationship of the kickapoo fault to the johnson valley and homestead valley faults, san bernardino county, california, *Bull. Seism. Soc. Am.*, *84*(3), 528–536.

Steinbrugge, K. V., E. G. Zacher, D. Tocher, C. Whitten, and C. Claire (1960), Creep on the san andreas fault, *B. Seismol. Soc. Am.*, *50*(3), 389–415.

Stuart, W. D., and T. E. Tullis (1995), Fault model for preseismic deformation at parkfield, california, *J. Geophys. Res.*, *100*(B12), 24,079–24,099.

Sun, X., and S. Hartzell (2014), Finite-fault slip model of the 2011 mw 5.6 prague, oklahoma earthquake from regional waveforms, *Geophys. Res. Lett.*, *41*(12), 4207–4213, doi :10.1002/2014GL060410.

Symm, G. T. (1963), Integral equation methods in potential theory–ii, *Proc. R. Soc. Lond. A*, *275*(1360), 33–46.

Tada, T. (1995), Boundary integral equations for the time-domain and time-independent analyses of 2d nonplanar cracks, Ph.D. thesis, Earth and Planetary Physics department at the University of Tokyo.

Tada, T., and R. Madariaga (2001), Dynamic modelling of the flat 2-D crack by a semi-analytic BIEM scheme, *Int. J. Numer. Meth. Eng.*, *50*(1), 227–251.

Tada, T., and T. Yamashita (1997), Non-hypersingular boundary integral equations for two dimensional non-planar crack analysis, *Geophys. J. Int.*, *130*(2), 269–282.

Thomas, A. M., R. M. Nadeau, and R. Bürgmann (2009), Tremor-tide correlations and near-lithostatic pore pressure on the deep San Andreas fault, *Nature*, *462*(7276), 1048–1051, doi :10.1038/nature08654.

Thomas, M. Y., N. Lapusta, H. Noda, and J.-P. Avouac (2014), Quasi-dynamic versus fully dynamic simulations of earthquakes and aseismic slip with and without enhanced coseismic weakening, *J. Geophys. Res.*, *119*(3), 1986–2004, doi :10.1002/2013JB010615.

Thomas, M. Y., H. S. Bhat, and Y. Klinger (2017), Effect of brittle off-fault damage on earthquake rupture dynamics, in *Fault Zone Dynamic Processes : Evolution of Fault Properties During Seismic Rupture, Geophysical Monograph 227*, edited by M. Y. Thomas, H. S. Bhat, and T. M. Mitchell, pp. 255–280, John Wiley & Sons, Inc., doi :10.1002/9781119156895.ch14.

Udías, A., R. Madariaga, E. Buforn, et al. (2014), *Source Mechanisms of Earthquakes : Theory and Practice*, Cambridge University Press.

Vallee, M., J.-M. Nocquet, J. Battaglia, Y. Font, M. Segovia, M. Regnier, P. Mothes, P. Jarrin, D. Cisneros, S. Vaca, et al. (2013), Intense interface seismicity triggered by a shallow slow slip event in the central ecuador subduction zone, *J. Geophys. Res.*, *118*(6), 2965–2981, doi : 10.1002/jgrb.50216.

Veedu, D. M., and S. Barbot (2016), The parkfield tremors reveal slow and fast ruptures on the same asperity, *Nature*, *532*(7599), 361–365, doi :10.1038/nature17190.

Viesca, R. C. (2016), Stable and unstable development of an interfacial sliding instability, *Phys. Rev. E*, *93*(6), 060,202, doi :10.1103/PhysRevE.93.060202.

Virieux, J., and R. Madariaga (1982), Dynamic faulting studied by a finite difference method, *Bull. Seism. Soc. Am.*, *72*(2), 345–369.

Wallace, L. M., S. C. Webb, Y. Ito, K. Mochizuki, R. Hino, S. Henrys, S. Y. Schwartz, and A. F. Sheehan (2016), Slow slip near the trench at the hikurangi subduction zone, new zealand, *Science*, *352*(6286), 701–704.

Weingarten, M., S. Ge, J. W. Godt, B. A. Bekins, and J. L. Rubinstein (2015), High-rate injection is associated with the increase in us mid-continent seismicity, *Science*, *348*(6241), 1336–1340, doi :10.1126/science.aab1345.

Wesnousky, S. G. (1988), Seismological and structural evolution of strike-slip faults, *Nature*, *335*(6188), 340–343.

Yeck, W., G. Hayes, D. E. McNamara, J. L. Rubinstein, W. Barnhart, P. Earle, and H. M. Benz (2017), Oklahoma experiences largest earthquake during ongoing regional wastewater injection hazard mitigation efforts, *Geophys. Res. Lett.*, *44*(2), 711–717, doi :10.1002/2016GL071685.

Yoshida, K.-i., N. Nishimura, and S. Kobayashi (2001), Application of fast multipole galerkin boundary integral equation method to elastostatic crack problems in 3d, *Int. J. Numer. Meth. Eng.*, *50*(3), 525–547.

Zigone, D., D. Rivet, M. Radiguet, M. Campillo, C. Voisin, N. Cotte, A. Walpersdorf, N. M. Shapiro, G. Cougoulat, P. Roux, et al. (2012), Triggering of tremors and slow slip event in guerrero, mexico, by the 2010 mw 8.8 maule, chile, earthquake, *J. Geophys. Res.*, *117*, B09,304, doi : 10.1029/2012JB009160.

UNIVERSITÉ SORBONNE PARIS CITÉ

Fast algorithms to model quasi-dynamic earthquake cycles in complex fault networks

par

Pierre Romanet

Résumé

Les failles sont rarement uniques et planes, le plus souvent elles agissent en réseau et présentent des complexités géométriques (rugosité, branches...) à toutes les échelles. Cependant, la majorité des modèles de cycles sismique jusqu'à ce jour, ne prennent pas en compte ces complexités géométriques. Cela est principalement dû aux limites des ressources informatiques, et au temps de calcul qui ne peut être accéléré simplement qu'en géométrie plane.

Dans cette thèse, nous avons développé un nouveau modèle quasi-dynamic du cycle sismique, avec une loi de friction de type "rate and state" et une loi d'évolution de la variable d'état "aging". Pour surmonter le problème du temps de calcul, sans pour autant se restreindre à une géométrie plane, nous avons fait appel à deux méthodes : la méthode multipolaire rapide et les matrices hiérarchiques. Ces deux méthodes permettent des gains de temps significatifs en réduisant la complexité du temps de calcul de l'ordre de $\mathcal{O}(N^2)$ à $\mathcal{O}(N \log N)$, N étant le nombre d'éléments utilisés pour discrétiser la faille.

En utilisant ce modèle, nous avons pu explorer le comportement de deux failles dont une partie se superpose en mode III. Alors qu'une faille unique donne lieu à un comportement périodique, avec toujours le même tremblement de terre se répétant, l'introduction d'une seconde faille interagissant avec la première fait apparaître une grande complexité dans le cycle sismique : comportement apériodique, ruptures partielles, "afterslip", coexistance des évènements lents et rapides. Dans le domaine particulier ou évènements de glissement lent et rapide coexistent, nous avons montré que le moment des ces deux types d'événement suivaient des lois d'échelle qui s'apparentent aux lois observées dans la nature par *Ide et al.* (2007). Nous avons aussi montré que la rugosité et les réseaux de failles en mode II ("in-plane"), provoquaient le même genre de complexités dans le cycle sismique.

Cycle sismique, rate and state, complexité géometrique, rugosité, matrices hiérarchiques, méthode multipolaire rapide

Abstract

In nature, faults are rarely planar and isolated, but rather act in networks of geometrically complex faults with roughness, kinks, jogs etc. at all scales. However, the majority of models of seismic cycles so far, do not take into account these geometrical complexities. This is mainly because of the limitation of computational resources. In this thesis, we developed a new model of quasi-dynamic seismic cycle, using a rate-and-state friction law with aging state evolution. To overcome the problem of calculation time, we appeal to two recent methods : fast multipole method and hierarchical matrices that accelerate matrix-vector products. These two methods do not add any restriction on the geometry and number of the faults and decrease the complexity of calculation time from $\mathcal{O}(N^2)$ to $\mathcal{O}(N \log N)$, N being the number of elements used to discretized the fault. Taking advantage of this model, we explore the problem of two overlapping faults that are interacting with each other in mode III. Knowing that a single straight fault system with constant rheological parameters gives rise to a characteristic periodic event that ruptures the entire fault, the add of another fault makes the seismic cycle much more complex with : aperiodic behavior, partial ruptures, afterslip, coexistence of slow and fast events. In the particular domain where both slow and fast events coexist, we show that the moment of these events follow two observed scaling laws (*Ide et al.*, 2007). We also showed that roughness and fault networks in in-plane stress and strain, quickly bring complexities when accounted for in the seismic cycle.

Seismic cycle, rate and state, geometrical complexity, roughness, hierarchical matrices, fast multipole method